PROCESS AND RELIABILITY ASSESSMENT OF

PLASMA-BASED COPPER ETCH PROCESS

A Dissertation

by

GUOJUN LIU

Submitted to the Office of Graduate Studies of
Texas A&M University
in partial fulfillment of the requirements for the degree of

DOCTOR OF PHILOSOPHY

August 2008

Major Subject: Chemical Engineering

PROCESS AND RELIABILITY ASSESSMENT OF

PLASMA-BASED COPPER ETCH PROCESS

A Dissertation

by

GUOJUN LIU

Submitted to the Office of Graduate Studies of
Texas A&M University
in partial fulfillment of the requirements for the degree of

DOCTOR OF PHILOSOPHY

Approved by:

Chair of Committee,	Yue Kuo
Committee Members,	Rayford G. Anthony
	Chin B. Su
	Victor M. Ugaz
Head of Department,	Michael Pishko

August 2008

Major Subject: Chemical Engineering

ABSTRACT

Process and Reliability Assessment of Plasma-based Copper Etch Process.

(August 2008)

Guojun Liu, B.S., Tsinghua University, Beijing, China

Chair of Advisory Committee: Dr. Yue Kuo

The plasma-based etching processes of copper (Cu) and titanium tungsten (TiW) thin films, and the electromigration of the copper lines patterned by above etching processes were studied. Instead of vaporizing the plasma/copper reaction product, a dilute hydrogen chloride solution was used to dissolve the nonvolatile reaction product. The plasma/copper reaction process was affected by many factors including the microstructure of the copper film and the plasma conditions. Under the same chlorine plasma exposure condition, the copper conversation rate and the copper chloride ($CuCl_x$) formation rate increased monotonically with the Cu grain size. The characteristics of the Cu etching process were explained by diffusion mechanisms of Cl and Cu in the plasma-copper reaction process as well as microstructures of Cu and $CuCl_x$. The Cu chlorination process was also affected by the additive gas in the Cl_2 plasma. The additive gas, such as Ar, N_2, and CF_4, dramatically changed the plasma phase chemistry, i.e., the Cl concentration, and the ion bombardment energy, which resulted in changes of the Cu chlorination rate and the sidewall roughness.

TiW thin films, used as the diffusion barrier layer for the Cu film, were reactive ion etched with CF_4/O_2, CF_4/Cl_2, and CF_4/HCl plasma. Process parameter such as feed gas composition, RF power, and plasma pressure showed tremendous effects on the etch rate and the etch selectivity. The TiW etch rate was a function of the sum of Cl and F concentrations and the ion bombardment energy. Cu/diffusion barrier metal stack was successfully patterned by above plasma etch processes. The electromigration (EM) performance of the Cu lines was evaluated by the accelerated isothermal test. The activation energy of 0.5~0.6 eV and the current density exponent of 2.7 were obtained. Failure analysis showed that both copper-silicon nitride cap layer interface and the copper grain boundary were active diffusion paths. The EM induced stress caused the cap layer crack and affected the reliability of Cu lines.

The processes studied in this dissertation can be applied in advanced microelectronic fabrication including large area flexible microelectronics.

To my wife, Qin Jiang,

and

my daughter, Yutong Liu

ACKNOWLEDGEMENTS

I would like to thank all the people who helped me to complete this dissertation. First of all, I would like to express my special gratitude to Dr. Yue Kuo, for his consistent guidance and encouragement through this research. Not only his knowledgeable and inspiring advices but also his dedicate attitude to the scientific research enlightened me through the research. I am more than proud of being his student, and cherish the great experience working with him.

Special appreciation is extended to Dr. Rayford G. Anthony, Dr. Victor M. Ugaz and Dr. Chin B. Su for serving as my Ph.D. advisory committee members and offering their valuable suggestions. Also, I would like to thank Dr. Mosong Cheng for his valuable discussions.

Appreciation is also given to my friends and group members at the Thin Film Nano & Microelectronic Research Laboratory, including Dr. Jun-yen Tweg, Dr. Jiang Lu, Dr. Hyun Ho Lee, Yu Lei, Dr. Helinda Nominanda, Jiong Yan and Chen-Han Lin, for their valuable assistance. Dr. Lu, Dr. Nominanda, Mr. Yan and Mr. Lin offered me many help in the thin film deposition and surface analysis. Mr. Lei's help with research equipment and valuable discussion is also appreciated. Their support and friendship made my research more fruitful and enjoyable.

Thanks also go to the department faculty and staff for making my time at Texas A&M University a great experience. I want to thank Mr. Randy Marek for his help to maintain the equipment.

I also want to thank Dr. D. Buckley, Mr. S. Ahmed and Mr. T. Ahmed at University of Limerick, Ireland, for their technical discussion and the surface analysis as part of the research in Chapter III.

Finally, I would like to thank my parents and brothers for their understanding and encouragement, my wife and daughter for their patience, love, and support.

This research is partially supported by National Science Foundation (contract # ECS-0103022), and Texas Instrument Corp.

TABLE OF CONTENTS

	Page
ABSTRACT	iii
DEDICATION	v
ACKNOWLEDGEMENTS	vi
TABLE OF CONTENTS	viii
LIST OF FIGURES	x
LIST OF TABLES	xv

CHAPTER

I	INTRODUCTION	1
	1.1 General concepts of interconnect technology	1
	1.2 Plasma etching process	5
	1.3 Plasma-based Cu etching process	10
	1.4 Diffusion barrier material and its etching process	18
	1.5 Electromigration of Cu interconnect lines	22
	1.6 Structure of this dissertation	26
II	EXPERIMENTAL AND ANALYTICAL METHODS	27
	2.1 Thin film preparation	27
	2.2 Plasma reactor and plasma diagnosis	30
	2.3 Electromigration test setup	37
	2.4 Physical and chemical characterization	38
III	GRAIN SIZE EFFECT ON PLASMA-BASED COPPER ETCH PROCESS	48
	3.1 Experimental	48
	3.2 Microstructure of Cu films	50
	3.3 Grain size effect on Cu chlorination process	55
	3.4 Summary	71

CHAPTER Page

IV ADDITIVE-GAS EFFECT ON CL_2 PLASMA-BASED COPPER ETCH PROCESS AND SIDEWALL ATTACK 72

4.1 Experimental 72
4.2 Additive gas effect 74
4.3 Summary 96

V REACTIVE ION ETCH OF TITANIUM TUNGSTEN THIN FILMS 97

5.1 Experimental 97
5.2 TiW film microstructure.. 98
5.3 TiW film etching characteristics 101
5.4 Selectiviy of TiW to PECVD SiN_x 116
5.5 Summary 120

VI ELECTROMIGRATION OF COPPER LINES PATTERNED BY CL_2 PLASMA-BASED ETCHING PROCESS.............................. 121

6.1 Experimental 121
6.2 Isothermal EM algorithm 124
6.3 Statistical performance of EM.. 130
6.4 Failure analysis 138
6.5 External bending stress effect on Cu EM 145
6.6 Summary 149

VII SUMMARY AND CONCLUSIONS 150

REFERENCES.. 154

APPENDIX A 162

APPENDIX B 163

VITA 165

LIST OF FIGURES

FIGURE Page

1.1 Comparison of intrinsic gate delay and interconnect delay as a function of feather size 3

1.2 Steady-state voltage distribution in RF plasma 7

1.3 Flues of species in plasma etching and their resulting profile: (a) reactive neutral chemical species; (b) ionic species 9

1.4 Vapor pressure of copper halides at various temperatures 11

1.5 Flow chart of plasma-based copper etch process 13

1.6 X-ray diffraction of (a) original Cu film, (b) after HCl plasma for 1 min, (c) after HCl plasma for 2 min. 16

1.7 Intrinsic diffusivity of (a) Al and (b) Cu in silicon 19

1.8 The required current density at operation conditions continues to rise with time as depicted by the International Technology Roadmap of Semiconductor. 24

2.1 Schematic configuration of RIE system 31

2.2 Electrode configuration in PE and RIE mode 33

2.3 Correlation between F-atom emission normalized to Ar emission and number density $I_F/(I_{Ar}/n_{Ar})$, and fluorine atom number density n_F 36

2.4 Schematic configuration of EM test setup 37

2.5 Schematic of AFM system 39

2.6 Schematic of SEM system 41

2.7 X-ray generation during EDX analysis 43

2.8 Photoelectron emission in XPS analysis 45

FIGURE Page

2.9 Bragg's law reflection: (a) rectangular grid, AB=BC, (AB+BC) = $2d_{hkl}\sin\theta$; (b) general case AB $\neq$ BC, (AB+BC) = $2d_{hkl}\sin\theta$...................... 47

3.1 (a) XRD patterns of as-deposited and annealed Cu films. Annealing conditions: 250°C~400°C, forming gas H_2(10%)/N_2(90%), for 30 min; (b) Cu film grain size and resisitivity under (a) condition.. 51

3.2 AFM images of the top surfaces of (a) as-deposited (b) 300 °C (c) 400 °C annealed Cu film 53

3.3 $CuCl_x$ formation rate and Cu conversion rate for the Cu films annealed at various temperatures 56

3.4 (a) EDS of 250°C, 300°C, 350°C and 400°C annealed Cu films after being exposed to Cl_2 plasma at 600 W, 60 mTorr, for 1 min; (b) the Cl/Cu ratio under (a) condition…………………………………………... 58

3.5 SEM cross-sectional and top views of (a) 250°C and (b) 300°C annealed Cu films after being exposed to Cl_2 plasma at 600 W, 60 mTorr, for 1 min. The inlets are the top views... 60

3.6 Surface roughness of the Cu film vs. annealing temperature, before and after plasma exposure and removal of $CuCl_x$. Plasma condition: 600 W, 60 mTorr, 12 sccm Cl_2, for 1 min 63

3.7 AFM of (a) as deposited, (b) 300°C annealed, (d) 400°C annealed Cu film after Cl_2 plasma exposure and removal of $CuCl_x$ layers. (c) and (e) are scan lines indicated in (b) and (d), respectively. Plasma condition: 600 W, 60 mTorr, 12 sccm Cl_2, for 20 seconds 65

3.8 Schematic diagram of etching process with (a) small grain (b) large grain Cu film. 68

3.9 Cu conversion rate as a function of total grain boundary area to total grain volume (1.5/G) and fitted straight line…………………………….. 70

4.1 Cross-section diagram of the metal stack prior to plasma exposure 73

4.2 Cu sidewall profile after Cl_2 plasma exposure and removal of $CuCl_x$, plasma conditions: 600 W, 30 mTorr, 20 sccm Cl_2. The sample was tilt 55° for SEM imaging 76

FIGURE Page

4.3 Effect of Ar concentration on cathode bias voltage in the Cl_2/Ar plasma at 600 W, 30 mTorr and 20 sccm total feed gas rate................................ 78

4.4 Cu sidewall after Cl_2/Ar (20%) plasma exposure and removal of $CuCl_x$. Sample was tilt 55° for SEM imaging 80

4.5 Effect of N_2 concentration on Cl concentration and cathode bias $-V_{dc}$ in Cl_2/N_2 plasma at 600 W, 30 mTorr, and 20 sccm total feed gas rate......... 82

4.6 Top view of Cu film after being exposed to (a) Cl_2 and (b) Cl_2/N_2(20%) plasma at 600 W, 30 mTorr, and 20 sccm total feed stream 84

4.7 ESCA spectra of Cu surface (a) Cu $2P_{3/2}$ before and after N_2 plasma exposure, and (b) N 1s after N_2 plasma exposure 86

4.8 Cu sidewall after Cl_2/N_2 (20%) plasma exposure and removal of $CuCl_x$. Sample was tilt 55° for SEM imaging 88

4.9 Effect of CF_4 concentration on Cl concentration and cathode bias $-V_{dc}$ in Cl_2/CF_4 plasma at 600 W, 30 mTorr, and 20 sccm total flow rate……… 90

4.10 ESCA spectra of Cu surface after Cl_2/CF_4(20%) plasma at 600 W, 30 mTorr, and 20 sccm total feed stream. (a) F 1s, (b) C 1s, (c) Cu 2p, and (d) Cl 2p……………………………………………………………….. 92

4.11 Cu sidewall after Cl_2/CF_4 (20%) plasma exposure and removal of $CuCl_x$. Sample was tilt 55° for SEM imaging.. 95

5.1 X-ray diffraction pattern of the sputter deposited TiW film 100

5.2 Effect of feed gas compositions on etch rate of TiW film at 100 mTorr and 300 W (total flow rate 20 sccm) 102

5.3 Effect of CF_4 concentration on Cl and F concentrations in the CF_4/Cl_2 plasma under the same conditions as in Fig. 5.2 104

5.4 (a) Effect of RF power on cathode self-bias voltage in the CF_4/Cl_2 plasma at 100 mTorr pressure (total flow rate 20 sccm); (b) effect of cathode self-bias voltage on TiW film etch rate in the CF_4/Cl_2 plasma with the CF_4 concentration of 25 %, 50 %, 75 %, and 100% respectively... 107

FIGURE Page

5.5 (a) Pressure effect on TiW etch rate in the CF_4(50%)/Cl_2 plasma at 300 W (total flow rate 20 sccm); (b) pressure effect on Cl and F concentrations and cathode self-bias voltage at the same plasma conditions as (a). 109

5.6 ESCA spectra of TiW films after being exposed to various plasmas at 100 mTorr, 300 W (total flow rate 20 sccm). (a) W $4f_{7/2,\ 5/2}$ peaks before and after CF_4 plasma exposure; (b) Ti $2p_{3/2,\ 1/2}$ peaks after CF_4, CF_4(50%)/Cl_2, and Cl_2 plasma exposure; (c) Cl $2p_{3/2,1/2}$ peaks after CF_4(50%)/Cl_2 and Cl_2 plasma exposure; (d) F 1s peaks after CF_4 and CF_4(50%)/Cl_2 plasma exposure........ 111

5.7 TiW surface after (a) Cl_2, (b) CF_4/Cl_2 plasma etch. Plasma condition: 300 W, 100 mTorr, 20 sccm, 20 seconds. 115

5.8 Effect CF_4 concentration on SiN_x etch rate under CF_4/Cl_2 and CF_4/HCl plasmas at 100 mTorr (total flow rate 20 sccm)........ 117

5.9 Effect of CF_4 concentration on etch selectivity of TiW to SiN_x under the same plasma conditions as in Fig. 5.8........ 119

6.1 (a) Illustration of the three-point bending setup for EM test; (b) optical image of the bended sample plate; (c) optical image of Cu line for EM test. 123

6.2 Flow chart of isothermal EM algorithm. (a) initialization phase; (b) temperature ramp and convergence phase; (c) constant power stress phase 126

6.3 Typical (a) resistance and (b) line temperature changes during isothermal EM test. 129

6.4 Correlation between initial current of stress phase at 320, 350 and 380 ºC and initial resistance.. 131

6.5 Cumulative failure distribution of thick Cu line at 350ºC with different chuck temperatures. The inset is the linear regression of ln (MTTF) vs. ln (J)........ 133

6.6 Cumulative failure distribution of 800 nm thick Cu lines at various test temperatures. The inset is the linear regression of [ln(MTTF) + n*ln(J)] vs. 1/kT, using n =2.7. 135

FIGURE Page

6.7 Cumulative failure distribution of 240 nm thick Cu lines at various test temperatures. The inset is the linear regression of [ln(MTTF) + n*ln(J)] vs. 1/kT, using n =2.7. 137

6.8 Illustration (a) and SEM images of void formation after EM at 350ºC for (b) 150 seconds; (c) 350 seconds. 139

6.9 Illustration (a) and SEM image (b) of voids by grain thinning and grain boundary depletion after EM at 350ºC. 141

6.10 Slit-like failure site of thin Cu line after EM at 170ºC. 142

6.11 (a) cap layer crack after EM at 320ºC and (b) EDX of the spot at (a). 144

6.12 Cumulative failure distribution of thick Cu lines at various temperatures with applied bending stress. The inserted is the linear regression of [ln(MTTF) + n*ln(J)] vs. 1/kT, using n = 2.7.. 146

6.13 Typical void distribution in (a) non-bended line, (b) bended line after EM at 350ºC. 148

LIST OF TABLES

TABLE Page

1.1 Properties of low-resistivity metals 4

1.2 Melting and boiling temperature of selective Ti and W chloride and fluoride 21

CHAPTER I

INTRODUCTION

1.1 General concepts of interconnect technology

The semiconductor industry is continuing its quest to improve the performance of microelectronic devices. These efforts are principally focused on two areas. On one hand, the speed of each individual device is increased by continuously shrinking the feather dimension of the device, and by applying the new materials such as high dielectric constant (high-k) materials.[1] On the other hand, in order to take advantage of the increased device speed, individual devices are connected into circuits using increasingly complex interconnect schemes, which involve multiplayer structure of several levels of metal wiring. The interconnect technology includes metal layer deposition, interconnect lines patterning, and establishment of electrically functional interconnection. The desired properties of the interconnect material are low resistivity, good adhesion to adjacent layers, and robustness to electromigration. The continuously shrinking of very large scale integrated (VLSI) circuits leads to the increase of current density flowing along the interconnection lines.[2] The signal propagation delay and the reliability of the interconnects are becoming critical issues when the feather dimension decreases.

This dissertation follows the style of *Journal of the Electrochemical Society*.

The signal propagation delay from the interconnection is usually called RC delay. The R and C are the effective total resistance of the interconnection and the capacitance associated with the dielectric. The RC can be expressed by the following equation.[3]

$$RC = \frac{\rho}{t_M} \frac{L^2 \varepsilon_{ILD}}{t_{ILD}} \tag{1.1}$$

where ρ, t_M, L, ε_{ILD}, and t_{ILD} are the resistivity, thickness, and length of the interconnect, and the interlayer dielectric (ILD) permittivity and thickness, respectively. A reduced t_M or t_{ILD} will increase the RC delay. For a given t_M and t_{ILD}, RC delay depends on ρ, ε_{ILD} and L, and is independent of width of the interconnection. Another signal delay called intrinsic gate delay is the carrier transient time in the device, typically depends on the gate dielectric material and its dimension. Figure 1.1 shows the interconnection delay and the intrinsic gate delay as a function of feather size.[4] When the feather size goes into the deep sub-micron region, the interconnection delay may be the limiting factor to the performance of VLSI. RC delay can be reduced by reducing ρ, ε_{ILD} and L, which means going to metals with lower resistivity, applying ILDs with lower dielectric constant (low-k), and optimizing the interconnect structure to reduce the metal line length. Many researches are being carried out to develop such materials and processes.

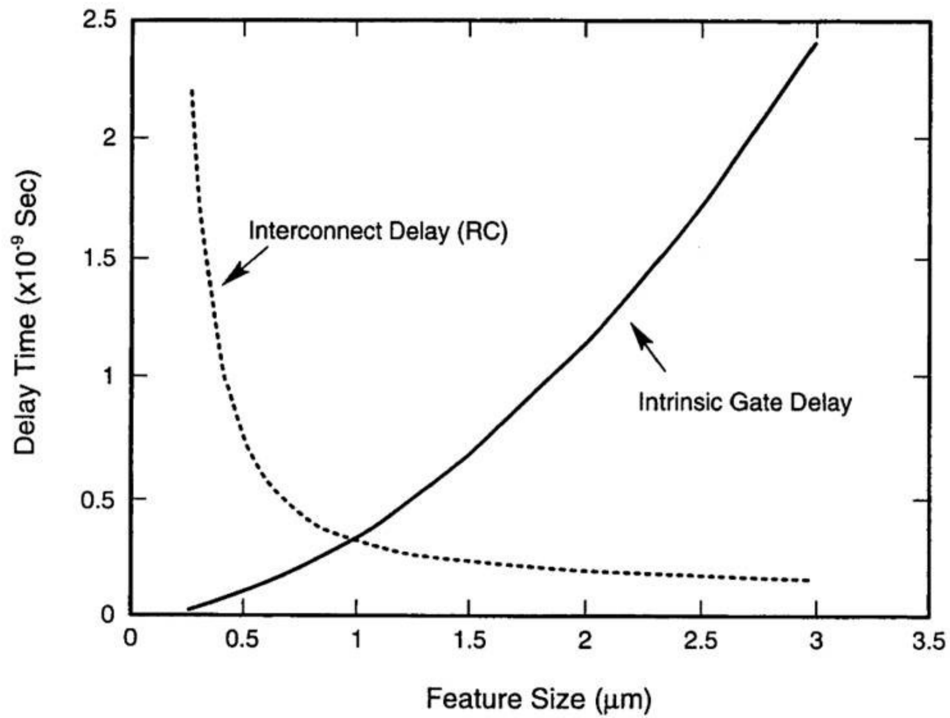

Figure 1.1 Comparison of intrinsic gate delay and interconnect delay (RC) as a function of feature size. (after Jeng.[4])

As far as lower resistivity is concerned, Table 1.1 lists the properties of the most commonly considered low-resistivity metals: Ag, Al, Au, and Cu. Aluminum was conventionally used as the material for interconnection. However, Al can not meet the high requirements for 180 nm VLSI and beyond due to its relative low resistivity.[5] Gold offers comparable resisitivty as aluminum. Sliver offers about 5% lower resistivity comparing with copper. However, Ag has much less electromgration resistance than Cu, i.e., the Ag diffusion constant is a few order magnitude higher than that of Cu. In addition, it is reported Ag can diffuse into SiO_2 at a much faster rate than Cu can.[6] Therefore, Cu has been chosen as the interconnect material. Besides the low resistivity, i.e., 35% lower than that of Al, Cu offers higher resistance to electromigration.

Table 1.1 Properties of low-resistivity metals.[3]

	Cu	Ag	Au	Al
Resistivity (μΩ-cm)	1.67	1.59	2.35	2.66
Melting Point (°C)	1085	962	1064	660
D(cm^2/s) at 100°C	2.1×10^{-30}	1.1×10^{-26}	2.2×10^{-27}	2.1×10^{-20}
Adhesion to SiO_2	Poor	Poor	Poor	Good
Delay (ps/mm)	2.3	2.2	3.2	3.7

Note: Delay = RC =34.5 Rs (ps/mm) for 1-mm-length conductor on 1-um thick SiO_2.

1.2 Plasma etching process

It would be helpful to give a review of plasma etching process before the discussion of Cu lines patterning. After thin films are deposited on the wafer or substrate surface, they can be selectively removed by etching to leave the desired pattern of the film. The etching process can be done in either “wet” or “dry” environment. Wet etching involves the use of liquid etchants. The target film is usually immersed into the etchant solution where the etchant chemically reacts with the material at the exposed area. Since the wet etchants attack the target film in all directions, most wet etching processes are isotropic. For modern VLSI circuits processing, the wet etching process is largely replaced by the plasma or dry etching process, because the latter provides a directional or anisotropic profile, which minimizes the undercut and allows the smaller and more tightly packed structure.

What is a plasma ?

Plasma is a partially ionized gas. Plasma can be generated and sustained in a DC or RF electric field which is impressed on the electrodes. The transport of electrons between the two electrodes results in some collisions with the gas molecules. Depending on the energy of the incoming electron, this collision can result in various species such as excited molecules, neutral atoms, secondary electrons, and ions. These ions and electrons are further accelerated by the electric field, so that they can collide with other molecules or atoms, thus resulting in an avalanche multiplication effect. Due to the light weight, electrons travel much faster than ions, and collide much more frequently with

the electrodes and reactor wall. Consequently, more electrons are removed from the plasma, leaving the plasma positively charged. In order to maintain the plasma neutral, a DC electric field is formed in such a way that the electrons are repelled from the electrodes and reactor wall. The plasma is sustained when the generation and removal of electrons and ions reach the balance. Figure 1.2 shows the potential distribution across the two electrodes. According to the continuity of the current flow, the DC potentials, i.e., V_1 and V_2, next to the two electrodes are related to the respective electrode areas, A_1 and A_2.

$$\frac{V_1}{V_2} = (\frac{A_2}{A_1})^m \tag{1.2}$$

where m is a constant between 2 and 4, depending on the system configuration. The DC potential drives the ions to bombard the target film, which enhances the etching process. In order to increase the DC potential during the etching process, the upper electrode and the sidewall are usually grounded. The lower electrode, also called target electrode, has a much smaller area than the other electrode. Therefore, a high DC potential V_2 is obtained at the target film.

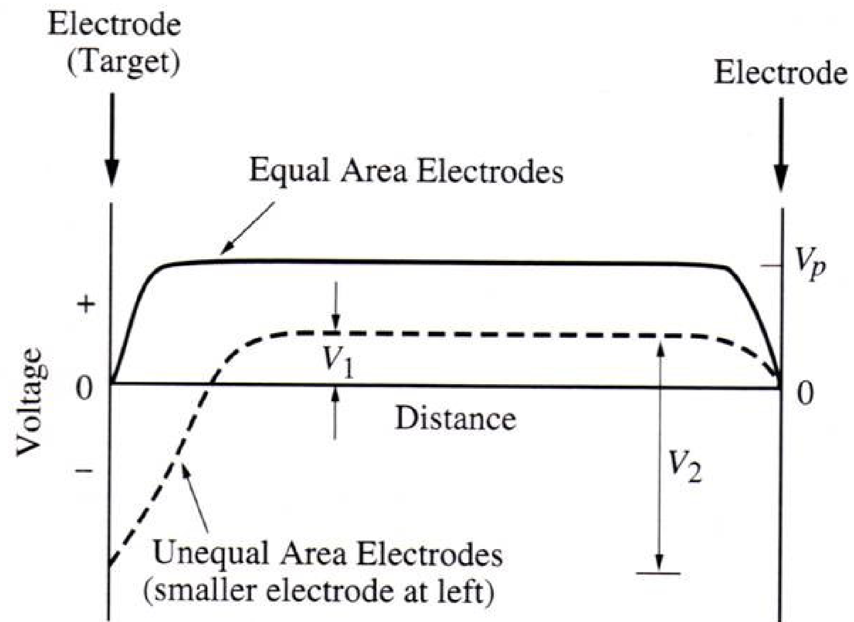

Figure 1.2 Steady-state voltage distribution in RF plasma. (after Pummer etc.[7])

General plasma etch mechanism

The two main types of species involved in the plasma etching are radical species and ions. The former is responsible for the chemical component in the plasma etching process; the latter is responsible for the physical component, i.e., ion bombardment. They can work independently or work together in a synergistic manner. Radicals are electrically neutral species that have incomplete bonding, which makes the radicals very reactive. The radicals can react with the target film to form volatile reaction products which are pumped away by the high vacuum pumping system. Most plasma processes are halogen based because the halide products usually have high volatilities. An additive gas can be introduced into the main feed stream to adjust the production of the reactive species. For example, oxygen can be added into a CF_4 plasma to increase the F concentration thereby increase the reaction rate.[8] Inert gases such as N_2 or Ar, can be added to dilute the reactant concentration. The chemical component of plasma etching, when acting by itself, proceeds isotropically but very selectively due to the nature of chemical reaction.

The physical component in the plasma etching is ion bombardment. Because of the voltage drop between the plasma and the electrode, the resulting electric field across the cathode sheath drives the positively charged ions to accelerate toward the electrode and sputter the target material. The flux of ion toward the wafer is almost normal to the film surface. Therefore, the physical etching is very directional and results in an anisotropic profile. However, the etching process by the ion bombardment is less selective because the sputter yields of most materials are fairly similar. Figure 1.3 illustrates the flues of

plasma species and their resulting profiles. Neutral chemical species result in an isotropic profile, while ionic bombardment tends to have an anisotropic profile.

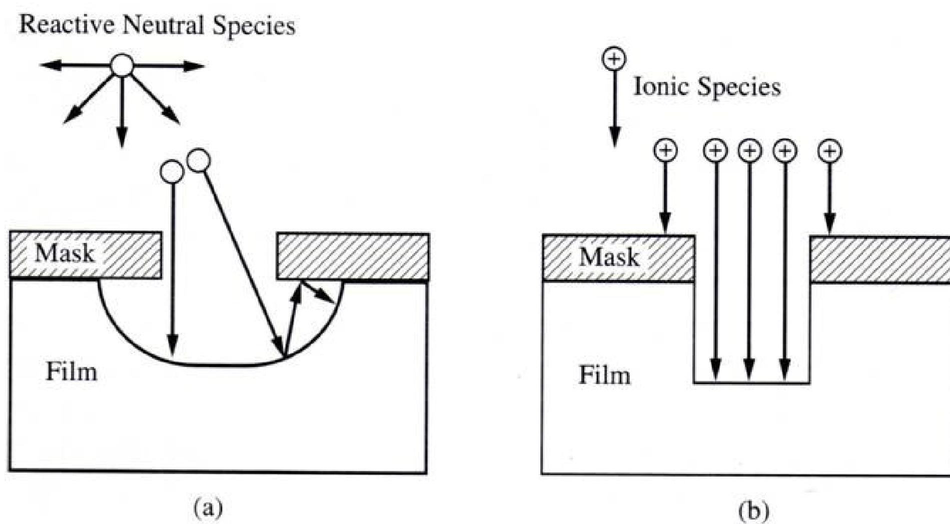

Figure 1.3 Flues of species in plasma etching and their resulting profile: (a) reactive neutral chemical species; (b) ionic species. (after Plummer etc.[7], p.624)

It is well recognized that the ions and reactive free radicals do not act independently for a reactive ion etch (RIE) process. The etch rate measured is not the sum of the two components acting independently; in many cases, it is much higher. There are many explanations and mechanisms proposed for the RIE process. The exact mechanism is process dependent. In most cases, the ion bombardment enhances one of the etching steps, such as surface adsorption, etching reaction, and removal of reaction products. For example, the ion bombardment causes the surface bond damage which makes the surface more apt to chemical reaction with the radicals. Or the ion bombardment accelerates the formation of the volatile reaction products. Or ion bombardment may dislodge or sputter away the etch by-products which would otherwise tend to stay on the surface and hinder the etch process.

With proper plasma conditions, an RIE process can give an anisotropic profile and high etch rate. In addition, a high selectivity to the underneath film can also be obtained because of the nature of chemical reaction involved in the etch process. High etch rate, anisotropic profile, high selectivity are usually the most desired properties for modern plasma etching processes.

1.3 Plasma-based Cu etching process

Although Cu is the ideal material for the interconnect, there are many challenges in Cu processing. For example, the Cu film is difficult to prepare into fine patterns with a conventional plasma etching process due to the low volatility of the plasma/Cu reaction product. Figure 1.4 shows the vapor pressures of copper halides at various temperatures.

The conventional plasma etch process is built on the principle of forming volatile plasma reaction product which is pumped away. In order to form volatile copper halide, the Cu substrate must be heated to above 200ºC, which makes the process less attractive for industry application. Currently, Cu fine lines are exclusively defined with the chemical mechanical polishing (CMP) process, such as damascene. However, the CMP process is costly and requires special chemical and wastewater treatment.[3,9,10]

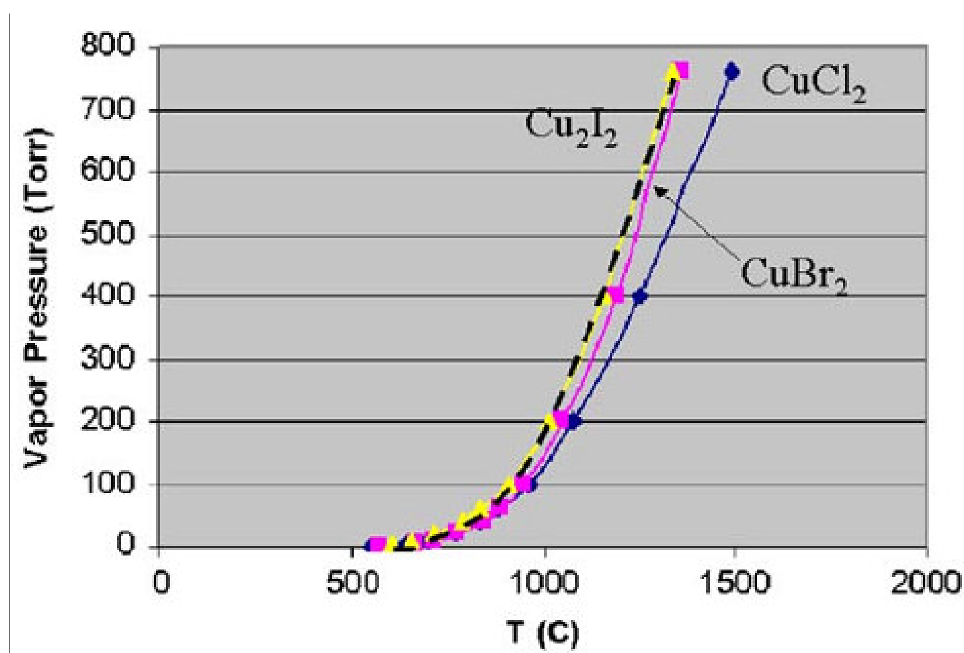

Figure 1.4 Vapor pressure of copper halides at various temperatures. (after Kuo and Lee.[11])

There are many studies on plasma etching of Cu.[12-15] These studies were focused on how to vaporize the nonvolatile reaction product generated in the plasma process, e.g., by applying an extra energy in the form of ultraviolet, infrared, or heat.[12,15] Kuo and Lee reported a new plasma-based Cu etching method using a conventional parallel-plate reactor with Cl_2 or Br_2 containing feed gas.[16,17] In stead of vaporizing the plasma/Cu reaction product, a dilute hydrogen chloride (HCl) solution was used to dissolve the nonvolatile product. Sub-micrometer Cu lines were successfully demonstrated.[11] This method has also been used to prepare the source, drain, and gate electrodes of thin film transistors.[18]

Figure 1.5 shows the process flow chart of the plasma-based Cu etching process. First, the Cu film is patterned with a conventional photolithography process. Secondly, the patterned Cu film is exposed to the Cl- or Br-based plasma. The Cu at unprotected area will be converted into $CuCl_x$ or $CuBr_x$, which is considered as a nonvolatile product but is very soluble in an acid solution. Then, the plasma exposed Cu film is dipped into a dilute hydrogen chloride (HCl) solution (6% V/V) to remove the $CuCl_x$ or $CuBr_x$. Finally, the photoresist pattern is stripped off by acetone or O_2 plasma ashing.

The key step of this unique Cu etch process is the plasma-Cu reaction, which is affected by plasma chemistry, reactants diffusion, ion bombardment, and properties of reaction products.[17] The Cu film conversion rate, the profile of patterned structure, and the morphology of the etched Cu surface are determined by the plasma-Cu reaction. The formation rate of $CuCl_x$ or $CuBr_x$ compound and their morphologies are related to

plasma parameters, such as gas composition, plasma pressure, power, and substrate temperature.[17,19]

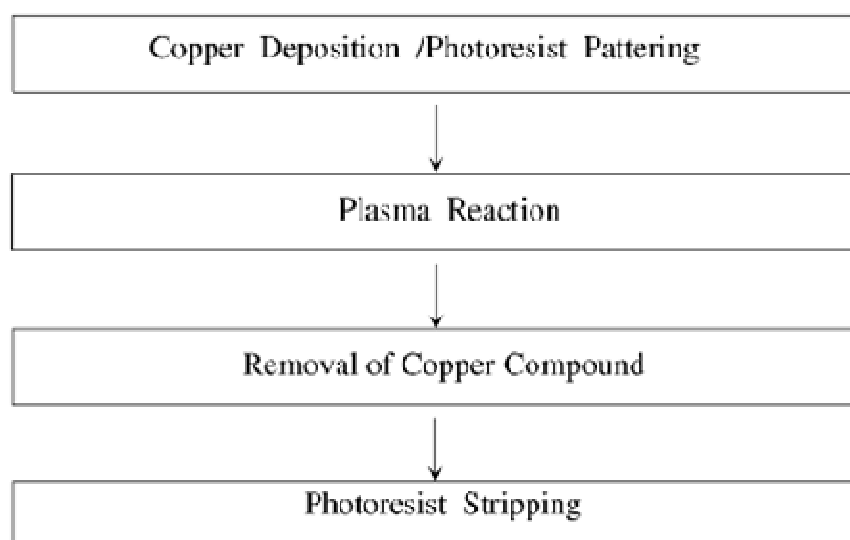

Figure 1.5 Flow chart of plasma-based copper etch process.

Cu-Cl_2 plasma reaction

Previously, most of the studies on the plasma-based Cu etching process were carried out on the as-deposited Cu film, i.e., the grain size and morphology were fixed. Many studies on plasma etching of metals show that the grain structure is critical to the etch process. For example, it was observed that the etch rate of molybdenum through the bulk grain is different from that at the grain boundary in the CF_4/O_2 plasma.[20] Similarly, for the reactive ion etching of aluminum with the CCl_4 plasma, the grain boundary was etched at a higher rate than the bulk gain was.[21] However, in the plasma etching of AlSiTi film, the grain boundary was etched at a lower rate than the bulk grain because impurities, such as Si, were accumulated at the grain boundary to hinder the etch process.[22] It is of great interest in investigating the effect of Cu microstructure on the etching process.

Reactions between Cu and Cl_2 have been studied under non-plasma and plasma conditions. Cu can react with HCl or Cl_2 without plasma but at a very low rate at room temperaure.[19] Under the HCl or Cl_2 plasma exposure condition, Cu can be converted to $CuCl_x$ at a very high rate. For example, a Cu conversion rate of 100 nm/min was obtained in the Cl_2 plasma at room temperature.[17] When Cu was converted into $CuCl_x$, the film thickness increased because the latter had a lower density and a more porous structure than the former. The $CuCl_x$/Cu volume expansion ratio of 3.1 was reported when Cu was exposed to the non-plasma Cl_2 environment[23], while the ratio was as high as 7 when Cu was exposed to the Cl_2 plasma.[17] At the non-plasma exposure condition, the $CuCl_x$ thickness increased linearly with time, which indicates that the thickness

growth is limited by the sticking probability of Cl_2. It is also possible that the $CuCl_x$ growth process is controlled by the reaction rate at the $CuCl_x$-Cu interface rather than the diffusion of Cl_2 through the Cu or $CuCl_x$ film.[24] The Cl/Cu ratio at the top surface was always smaller than 1, which was attributed to the mechanism that the top surface was continuously refreshed by the fast Cu diffusion from the bulk Cu film.[23] However, the Cl/Cu ratio of larger than 1 was obtained on the $CuCl_x$ film formed by exposing Cu to the Cl_2 plasma.[17] Under non-plasma condition, the metal chlorination process was analogous to the metal oxidation reaction, which was governed by the Cabrera-Mott model. The reaction included place exchange and diffusive motions of cations and anions in the crystal lattices.[25] The same mechanism was applied to explain the chlorination of Ag and Cu.[23] The Cl_2 plasma-Cu reaction product, i.e., $CuCl_x$, is polycrystalline with dominant (111) orientation, which is the same as the grain orientation of the original Cu film, as shown in Figure 1.6. The surface roughness and porosity of the $CuCl_x$ product increased with the reaction time.[17,23] For a polycrystalline Cu film, Zhang and Machlin reported that the Cu chlorination proceeded along the grain boundaries much faster than through the bulk grain when Cu was exposed to non-plasma Cl_2.[26] However, it was also reported the single crystal Cu film showed faster reaction rate than the polycrystalline Cu film in the Br_2 enviroment.[27] Therefore, the Cu film's microstructure greatly influences its plasma chlorination process, which is critical to the practical production process but has never been explored. In this dissertation, the temperature effect on the Cu microstructure and its influence on the Cl_2 plasma-Cu reaction process were investigated.

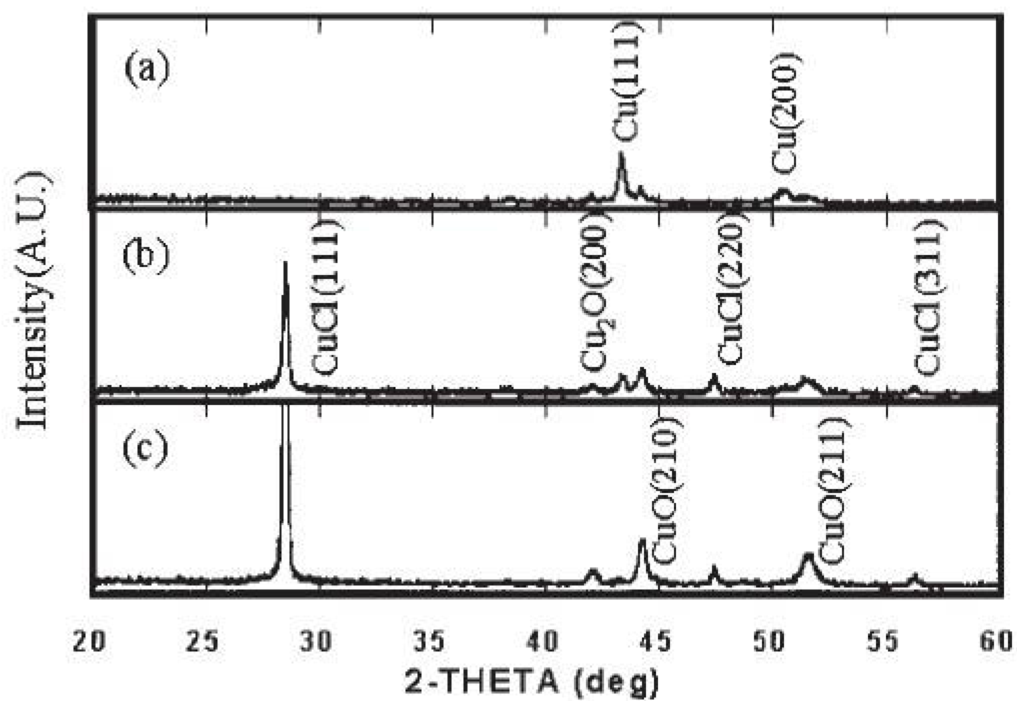

Figure 1.6 X-ray diffraction of (a) original Cu film, (b) after HCl plasma for 1 min, (c) after HCl plasma for 2 min. (after Lee and Kuo.[28])

Sidewall attack

The profile of the etched film is always a big concern in the plasma etching process. The local sidewall attack, i.e., "notching", is a serious problem in plasma etching of metals.[29-31] There are several possible reasons for the notching formation. For example, neutral radicals in the plasma phase can impinge the wafer surface obliquely, which results in excessive attack of the sidewall.[30] The photoresist pattern can contribute to the sidewall damage, too. The upper part of the photoresist sidewall can be negatively charged due to trapping of electrons generated in the plasma phase, which distorts the trajectory of the incident ions and intensifies the ion bombardment at the bottom sidewall to form the notch.[29] It was also reported that the stress at the film-film interface could induce spontaneous etching and cause sidewall notch.[32]

The sidewall attack can be reduced by adjusting the plasma phase chemistry. For example, in aluminum (Al) etch, by reducing BCl_3 ratio in Cl_2/BCl_3 plasma, the heavy ion concentration was reduced, which resulted in less sidewall attack.[29] By lowering the reactive radical concentration, the sidewall attack can also be reduced. Notch-free Al pattern was obtained in the HCl/He plasma in which the Cl concentration was lowered by the He diluent and H scavenge effect.[29] Another way of reducing the sidewall attack is to form a passivation layer on the sidewall surface. The introduction of CH_4 into the Cl_2 plasma promoted the formation of a polymeric surface layer which resulted in a smooth sidewall.[30] The passivation layer can also be an inert inorganic material. For example, during Si etch the addition of N_2 in the Cl_2 plasma caused the formation of Si-N bond on the sidewall, which stopped the sidewall attack.[33] However, the addition of

this kind of etchant in the gas could change the plasma chemistry, which may increase or decrease the etch rate of the film. The passivation layer also affects the etch rate, the surface morphology and roughness.

1.4 Diffusion barrier material and its etching process

Copper (Cu) has been widely accepted as a substitute for aluminum (Al) as the interconnect material in VLSI circuits because of its low resistivity and superior resistance to electromigration. However, Cu has high diffusivity in silicon. As shown in Figure 1.7, the diffusivity of Cu in Si is a few orders of magnitude higher than that of Al. In addition, Cu has poor adhesion to the underneath dielectric layer.[34] The high diffusivity of Cu causes device failure and the poor adhesion results in pealing-off from the dielectric layer. Hence, a diffusion barrier is necessary between Cu and the underneath material. Titanium tungsten (TiW) films have been used as the diffusion barrier for Al and Cu interconnect materials for many years.[35-37] TiW is an alloy of titanium and tungsten, both of which have been used in the integrated circuits.[38,39] The film properties are dependent on its composition, i.e., W to Ti ratio. It was proposed that W mainly serves as a barrier material, and that Ti mainly promotes the adhesion to the adjacent layer and stuffs grains boundaries.[40] Typically, the TiW film is rich in W with the W atomic concentration in the range of 70%-90%. Therefore, the film is also described as WTi.

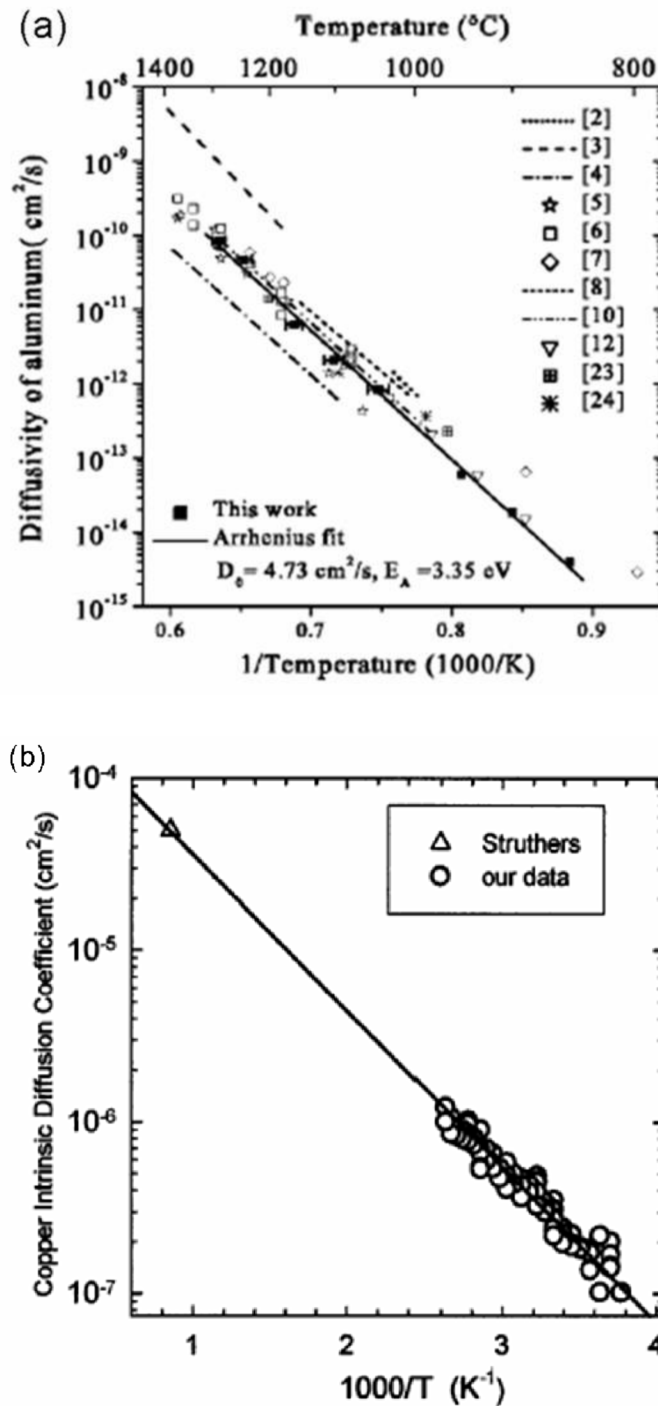

Figure 1.7 Intrinsic diffusivity of (a) Al and (b) Cu in silicon. (after Krause[41] and Istratov etc.[42])

There are only a few studies in literature on plasma etching of the TiW thin films; in contrast, many studies have been carried out on plasma etching of Ti or W. The volatility of reaction products is critical factor to the etch process. The volatility has a direct correlation to its melting point. Table 1.2 listed the melting and boiling temperatures of Ti and W chlorides and fluorides, which are the possible reaction products. $TiCl_4$ and WF_6 are considered as volatile materials at room temperature. Therefore in most cases, the etching process is carried out with halogen-containing gases, such as SF_6, CF_4, BCl_3, and Cl_2.[37-39,43] For example, Fishl and Hess reported that Cl atoms could react with W to form the volatile WCl_4 product; however, Cl_2 molecules did not react with W to form a volatile product.[44] For W etch, the F-based gases are more popular than the Cl-based gases. Although different tungsten fluoride (WF_x) stoichiometries could be formed from the plasma-W reaction, the main reaction product is WF_6 that has the lowest boiling temperature, i.e., 18°C, among all tungsten fluorides.[39] SF_6 has been used as the etch gas.[37,39] However, the role of the sulfur atoms in the SF_6 plasma etching process has been a concern. S atoms can bond to the surface to inhibit surface oxidation and enhance the etching process.[37,45] On the other hand, the S residue on the etched surface may cause contamination. Due to the latter, CF_4 appears to be a better etchant than SF_6 for W etching.[46] Separately, F- and Cl-based gases have been used in plasma etch of Ti with TiF_4 and $TiCl_4$ as the major reaction products. In some cases, $TiCl_2$ was also detected.[38,43] Fluorine has been reported as a catalyst in the Ti etching process. The adsorbed F makes the Ti surface more reactive with Cl, which facilitates the etching process.[38]

Table 1.2 Melting and boiling temperature of selective Ti and W chloride and fluoride.

	$TiCl_2$	$TiCl_4$	TiF_4	WCl_6	WF_6
Melting Point (°C)	1035	-24	284	275	2
Boiling Point (°C)	1500	136.5	N/A	346	18

Although many studies have been carried out on either W or Ti etching, the results can not be extrapolated to TiW etching. Some contradictory statements can be found in literature. For example, Riley concluded that Cl promoted the etch rate of TiW film.[47] However, Jin et al., concluded that Cl could hardly be incorporated in the etch of TiW.[37] In this dissertation, the plasma etching process of TiW was studied using various Cl- and F-containing gas mixtures under different operating conditions. The mechanism of the etching process has been investigated with regard to plasma phase chemistry and ion bombardment energy. Plasma attack of the TiW film was also investigated. In addition, since plasma enhanced chemical vapor deposition (PECVD) SiN_x is often used as a interlayer dielectric or passivation layer,[48] it is important to obtain a high etch selectivity between TiW and the underneath SiN_x. The plasma influence on the selectivity of these two films was also investigated.

1.5 Electromigration of Cu interconnect lines

Electromigration (EM) is one of the most critical reliability issues for VLSI circuits due to the aggressive decrease of interconnect dimension and the consequent very large current density.[2] Copper interconnects are typically patterned by a damascene process, using the chemical mechanical polishing to remove the Cu outside of the dielectric trench. EM studies on the damascene Cu line showed that it had a lifetime one or two orders of magnitude longer than that of the aluminum (Al) line.[2] However, the EM performance of the Cu lines patterned by the plasma-based etching process has not been explored.

EM tests to evaluate and project the reliability of Cu interconnects are usually conducted in ovens at elevated temperatures and moderate currents on packaged chips.[49] In this approach, temperature and current density can be varied independently. However, this kind of reliability test is very expensive and time consuming, which is especially true when applied to the Cu metallization due to the requirement of an extended test time. On the other hand, the isothermal EM test can be performed on a wafer probe station using an electrical current to supply both temperature and current acceleration. The major disadvantage to the isothermal EM test is that temperature and current density cannot be controlled independently. To make the lifetime projection by the isothermal EM test more reliable, many works were devoted to the comparison of the isothermal EM test and the package level EM test. It is generally recognized that the former could provide a similar in-deep understanding of the physical failure mechanism of the interconnect line as the latter could.[50,51]

In order to assess the reliability of interconnect lines at regular use condition, the tests that are carried out at high temperature and current densities need to be scaled to the use condition. The extrapolation is commonly based on Black equation, which expresses the median time to failure (MTTF), or 50th percentile fail time of a failure population as following.[52]

$$MTTF = \frac{A}{J^n}\exp(\frac{E_a}{kT}) \tag{1.3}$$

where J, k and T are current density, Boltzmann's constant and temperature, respectively, A is an empirical constant, n is the current density exponent, and E_a is the activation energy. To determine the MTTF at use condition, a ratio of Black equations between the use and test conditions can be employed for extrapolation.

$$\frac{MTTF_{use}}{MTTF_{Test}} = (\frac{J_{Test}}{J_{use}})^n \exp[\frac{E_a}{k}(\frac{1}{T_{use}} - \frac{1}{T_{test}})] \tag{1.4}$$

where $MTTF_{use}$ is the median time to failure at regular use condition. Figure 1.8 shows the required current density at operation conditions depicted by the International Technology Roadmap for Semiconductor. The key parameters such as n and E_a that affect the extrapolated electromigration reliability need to be determined in the reliability test.

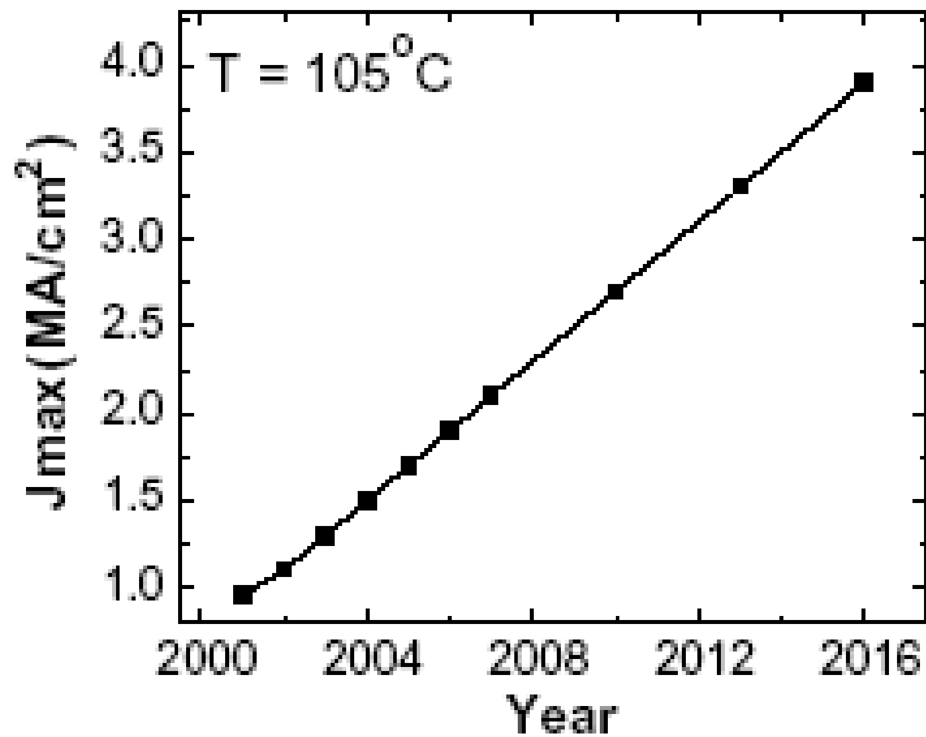

Figure 1.8 The required current density at operation conditions continues to rise with time as depicted by the International Technology Roadmap of Semiconductor. (2002 edition)

The EM induced failure occurs due to of the flux divergence. Microscopic divergence can happen at a triple junction point of the grain-boundary network or any other location where the inhomogenous mass transport occurs.[49] Macroscopic divergence may occur at the bottom of a via for the two-level testing structures where the via or the barrier layer blocks the EM flux, or the interface between Cu and the cap layer where the interfacial diffusion is the primary transport mechanism.[53] It is necessary to identify the diffusion path and to determine the activation energy (E_a) for the EM failure process when Cu line's reliability is assessed. Previously, a wide range of E_a values were reported due to different diffusion mechanisms. For example, the lattice diffusion corresponded to an E_a value of 2.1 eV and the grain boundary diffusion showed an E_a value of 1.2 eV.[54] For Cu metallization, the surface or interface diffusion is often the primary failure mechanism. Proost reported an E_a value of 1.06 eV for the Cu-metal interface diffusion.[55] Vairagar et al reported an E_a value between 0.6 and 0.88 eV on the Cu-dielectric interface diffusion mechanism.[56] An even lower E_a value, e.g., 0.4 to 0.5 eV was reported when the failure mode was associated with the extrusion or the non-perfect adhesion between Cu and the dielectric cap layer.[57,58]

The EM performance depends not only on the film structure, but also the patterning process. Fillipi et al. compared the EM tests of the AlCu lines fabricated by the damascene process and the reactive ion etching (RIE) process. The damascene lines showed a longer lifetime than the RIE lines. Although the lines from both processes showed similar values of E_a, the current density acceleration exponent was close to 2 for the damascene structures and close to 1 for the RIE structures.[59] Most Cu lines reported

in literature were fabricated with the damascene process. In this dissertation, the EM performance of the Cu lines patterned by the Cl_2 plasma-based etch process was reported.

1.6 Structure of this dissertation

Chapter II describes the primary experimental setups, and reviews the analytical techniques used in this dissertation. Chapter III focuses on the Cu microstructure effect on the plasma-based Cu etch process. The Cu films were sputtering deposited and annealed at various temperatures. The Cu grain size increases with the annealing temperature. The Cu grain size effects on the plasma-based Cu etch process such as $CuCl_x$ formation rate, Cu conversion rate, and surface morphology were investigated. Chapter IV focuses on the additive gas effects on the Cl_2-plasma based Cu etching process and sidewall attack. Various additive gases such as Ar, N_2, and CF_4 were introduced in the Cl_2 based plasma process. Their effects on the Cu etching process and sidewall attack were examined. With the proper plasma conditions, a smooth sidewall was obtained. Chapter V focuses on the reactive ion etching process of TiW film, which is commonly used as a diffusion barrier for the Cu film. The RIE process of TiW was investigated using various Cl- and F- based plasma. The etching mechanism was investigated regarding plasma chemistry and ion bombardment energy. Chapter VI focuses on the electromigration of Cu lines patterned by above plasma-based etching processes. The statistical reliability performance and the failure mechanism were investigated. Chapter VII summarizes all the work done in this dissertation.

CHAPTER II

EXPERIMENTAL AND ANALYTICAL METHODS

In this chapter, the sample preparation, the experimental setup, and the analytical methods are described in detail. The theories related to the experimental setup are briefly reviewed. The techniques of the chemical and physical analysis are reviewed in aspects of the operation principle and the application of each technique. The detail experimental procedure for each sub-topic will be described in the respective chapters.

2.1 Thin film preparation

The TiW and the Cu thin films used in this dissertation were deposited within a magnetron sputtering system with a RF or DC power supply. The sputtering chamber was equipped with two sputtering guns that were connected to an RF (13.6 MHz) or DC generator. The inert gas of Ar was introduced through a mass flow controller (MFC). The target size was 2 inch in diameter, and was loaded to the sputtering gun, which was about 15 cm above the substrate. For the TiW film, a composite target (10 atom % Ti/ 90 atom % W) was used. A high-purity Cu target (99.997%, Target Material Inc.) was used for the Cu deposition. The substrate was rotated at 20 rpm for uniform deposition. A base pressure of 10^{-7} Torr was reached before the deposition started. During the thin film deposition, the working pressure was kept at 5×10^{-3} Torr. Plasma was generated when a high voltage was applied to the sputtering gun. Due to the highly energetic ions striking,

the atoms were ejected from the TiW or Cu target surface and deposited onto the substrate. The power through the sputtering gun was adjusted to an optimal condition.

The silicon nitride film used in this dissertation was prepared by the plasma enhanced chemical vapor deposition (PECVD, Applied Materials, Model AMP 3300I, Santa Clara, CA). The PECVD system has a parallel-plate-electrode configuration with the electrode size of 65 cm in diameter and the electrodes distance of 6.25 cm. The bottom electrode is connected with an electrical heater and a heat exchanger. The substrate temperature can be controlled between 20ºC and 300ºC. The feed gases of SiH_4, NH_3 and N_2 were introduced into the PECVD chamber through the MFCs. The primary reaction on the substrate surface during the deposition is [7]

$$SiH_4 + NH_3 \rightarrow SiN_x + H_2 \qquad (2.1)$$

N_2 is used as a dilute to prevent the gas phase reaction. In order to obtain the uniform film, the PECVD deposition was controlled at the kinetics control region. Due to the nonequilibrium nature of the deposition process, the film properties (composition, density, stress, etc) can be easily altered. The nitride film is usually nonstoichiometric. A certain amout of hydrogen may exist in the film in the form of Si-H or N-H.[60] Both the stoichiometryand the dydrogen content of film affect its mechanical and electrical properties. The N/Si ratio depends on the deposition conditions such as feed gas flow rate, substrate temperature, and RF power. There are two advantages of the PECVD process. First, the film can be deposited at relative low temperature, i.e, 200-350ºC. The CVD process without plasma is usually carried out at least 600ºC. For a PECVD process, because of the additional energy from the plasma to the reactive species, the

reaction for deposition occurs at a lower temperature with less thermal budget. Secondly, the PECVD deposited film has conformal step coverage. This is attributed to the ion bombardment, which provides energy to the adsorbed species and allows them to diffuse along the surface. Silicon nitride is impermeable to most impurities, which qualifies its primary use as a passivation layer, especially as a diffusion barrier to moisture and sodium, or as a selective oxidation mask to prevent oxygen from penetration into the underneath layer. In this research, silicon nitride was used to prevent Cu from oxidation in the electromigration tests.

Silicon thermal oxidation was carried out in a tube furnace which can be electrically heated up to 1100ºC. Ultra high purity N_2 and O_2, and forming gas (N_2 90%/H_2 10%) were connected to the furnace through the MFCs. The bare silicon substrate was cleaned with a standard RCA procedure prior to the thermal oxidation. The detail RCA cleaning procedure can be found in the Appendix A. The Cu film post-deposition annealing was also carried out in the same tube furnace. During the Cu film annealing, the forming gas flow rate was kept at 200 sccm and the tube pressure was controlled below atmosphere. The tube furnace was well sealed without leaking. The Cu film was annealed in forming gas for 30 minutes at various high temperatures. In order to prevent the Cu film oxidation at the high temperature, for each annealing process the tube was purged with pure N_2 before and after the annealing temperature was reached.

Conventional photolithography was used to define the line-and-space pattern using a g-line (436 nm) sensitive positive photoresist AZ5214 (Clariant , Somerville, NJ). The photoresist was spin coated on the target film at 4000 rpm with a spinner (Headway

Research, Inc. Garland TX) followed by a soft-bake at 90ºC for 1 minute. A contact mask aligner (Quintel Q4000, Quintel Corporation, San Jose, CA) was used for the UV exposure. The UV exposed photoresist film was developed in an AZ MIF 300 developer solution (Clarient, Somerville, NJ) to reveal the pattern. After a hard-bake at 120ºC for 3 minutes, the patterned film was ready for the etching process.

2.2 Plasma reactor and plasma diagnosis

Plasma reactor

Plasma exposure was carried out in a plasma etch reactor (Plasma-Therm 700C, St. Petersbug, FL). Figure 2.1 shows a schematic diagram of the plasma reactor. It has a conventional parallel-plate configuration with the cathode size of 22.86 cm in diameter and the space of the electrodes of 7.3 cm. The plasma reactor is equipped with a RF (13.56 MHz) generator and a RF matching network. Multiple MFCs are used to connect various feed gases. A mechanical pump and a turbo pump are attached to the system. The upper electrode also functions as a shower-head distributor to improve the uniformity during the etch process. A heat exchanger was attached to the lower electrode to maintain the constant temperature during the plasma exposure. The whole system is controlled through a software interface programmed by Lookout®. Several high purity feed gases were used for plasma reaction. The feed gases includes hydrogen chloride (HCl) (ULSI 5.0 purity, 99.999%, Matheson Tri-Gas, Hurst, Texas), chlorine (Cl_2) (semiconductor 3.9 purity, 99.99%, Matheson Tri-Gas, Hurst, Texas), argon (Ar) (semiconductor 5.0 purity, 99.999%, Matheson Tri-Gas, Hurst, Texas), nitrogen (N_2)

(semiconductor 5.0 purity, 99.999%, Matheson Tri-Gas, Hurst, Texas), freon 14 (CF_4) (halocarbon 14 semiconductor 3.5 purity, 99.95%, Matheson Tri-Gas, Hurst, Texas), and oxygen (O_2) (OX 4.3UH, 99.993%, Praxair, Austin, Texas).

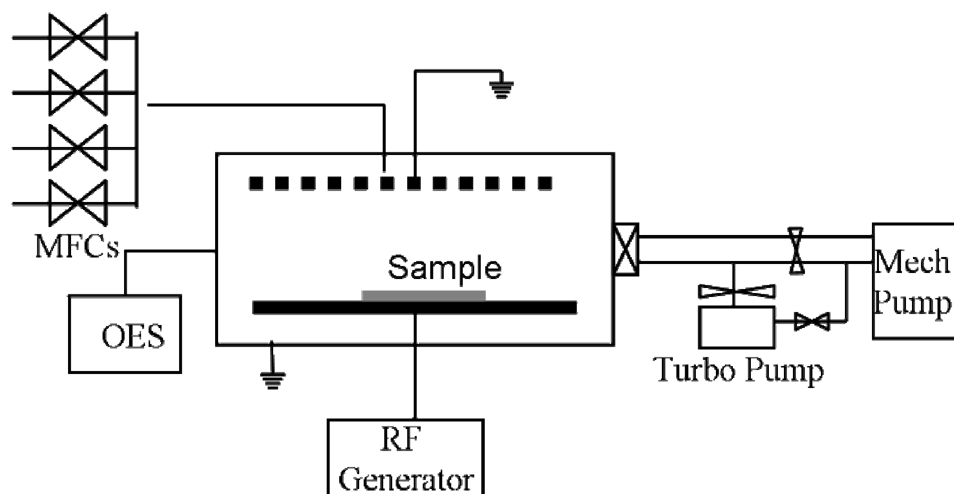

Figure 2.1 Schematic configuration of RIE system.

After a sample was loaded, the plasma chamber was pumped down by the mechanical pump and the turbo pump. A base pressure less than 10^{-5} Torr was reached before the plasma process started. The typical plasma process parameters such as the process pressure, the feed gas and its flow rate, the RF power, and the plasma exposure time were controlled through the operation software. The feed gases were introduced into the chamber through the MFCs. Plasma was generated when the RF power was applied across the electrodes. The system can work at plasma etching (PE) mode or reaction ion etch (RIE) mode depending on the electrode configuration. As illustrated in Figure 2.2, for RIE mode, the RF source is connected to the lower electrode, resulting in a substantial potential drop. The reversed situation occurs in the PE mode. During plasma exposure, the cathode bias voltage ($-V_{dc}$) can be considered as a reference to the ion bombardment. For most metal etch processes, the RIE mode is preferred because of the high ion bombardment energy. As discussed in Chapter I, the radical concentration is anther crucial parameter to the plasma etching process. In this study, the plasma phase was monitored with an optical emission spectroscope (OES, model PCM 100 SC technology, Fremont, CA). The detail about OES will be discussed in the following section.

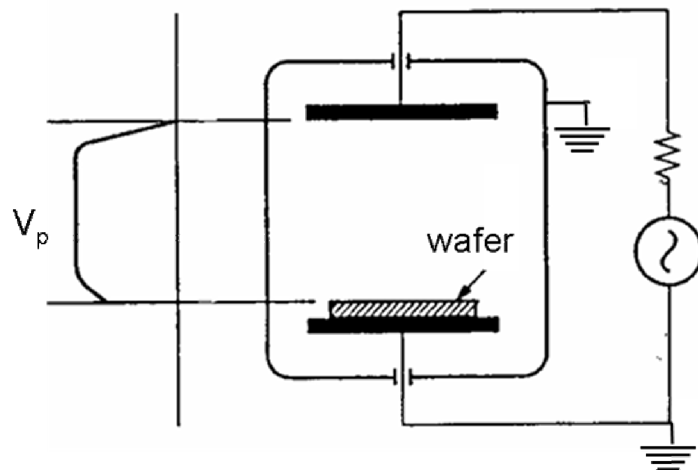

PE mode

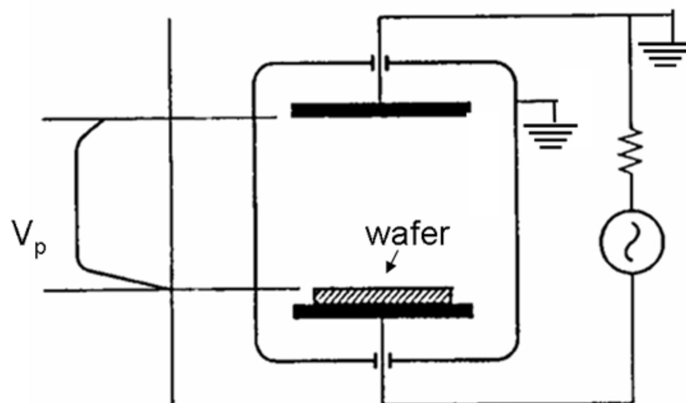

RIE mode

Figure 2.2 Electrode configuration in PE and RIE mode. (after Sugawara.[61] P.185)

Plasma diagnostics

Plasma process is complex in term of physical and chemical properties, therefore, a large array of process monitors, historically called “plasma diagnostics”, are applied to characterize the plasma, or to monitor critical parameters. It is not the scope of this chapter to review all plasma diagnostics techniques. General background and quantitative analysis of optical emission spectroscopy (OES) are reviewed as follow.

Plasma-induce optical emission can arise from electron impact excitation,

$$A + e \rightarrow A^{*} + e, \tag{2.2}$$

electron impact dissociation,

$$AB + e \rightarrow A^{*} + B + e \tag{2.3}$$

with emission process.

$$A^{*} \rightarrow A + hv \tag{2.4}$$

where A and B are atoms or molecules, * indicates the excited, emitting species. The excited species in the plasma emit photos when return to the ground state. The spectra emitted by the excited chemical species are practically unique, which makes spectroscopy extremely useful as an indicator of composition of a gas mixture. For CF_4/O_2 plasma, reaction (2.2) was mainly responsible for emission from excited F-atoms.[62] For Cl_2 plasma, both reaction (2.2) and (2.3) were reported.[63] The intensity of emission can be expressed as follow.[64]

$$I_{A^*} \propto n_{A^*} \propto n_A \int_{E^0}^{\infty} \sigma_A(E)\varepsilon(E)dE \tag{2.5}$$

where n_{A^*} is the number density of the excited species A^*, n_A is the ground state number density of A, σ_A is the energy-dependent electron impact excitation cross section, $\varepsilon(E)$ is the electron energy distribution function, and E^0 is the threshold energy. Electron energy distributions in plasma phase are complex. It is extremely difficult to accurately calculate the exact ground state density. In such a case, the actinometry has been used to obtain the relative density. A small amount of inert gas, such as Ar, is added to the plasma. For most plasma applications, the following assumptions can be made, (1) the excited state is formed only by single step electron excitation from the ground state, (2) the velocity dependence of the cross section for this excitation is similar to that of the species of interest, (3) emission probability is truly constant.[64] Under these circumstances, the concentration can be obtained by the following equation.

$$n_A = cn_{Ar}(\frac{I_A}{I_{Ar}}) \qquad (2.6)$$

where c is a proportionality constant, n_{Ar} and I_{Ar} are Ar concentration and emission intensity, respectively. Therefore, the concentration of the interested species can be estimated by normalizing the OES intensity of the species to that of Ar. This technique has been successfully applied for the CF_4/O_2 and Cl_2 plasma.[62] As shown in Figure 2.3, the normalized emission is directly proportional to the F concentration over a wide range of conditions, regardless of gas composition.[65] In this dissertation, the actinometry approach was used to estimate the relative concentrations of Cl and F at various plasma conditions.

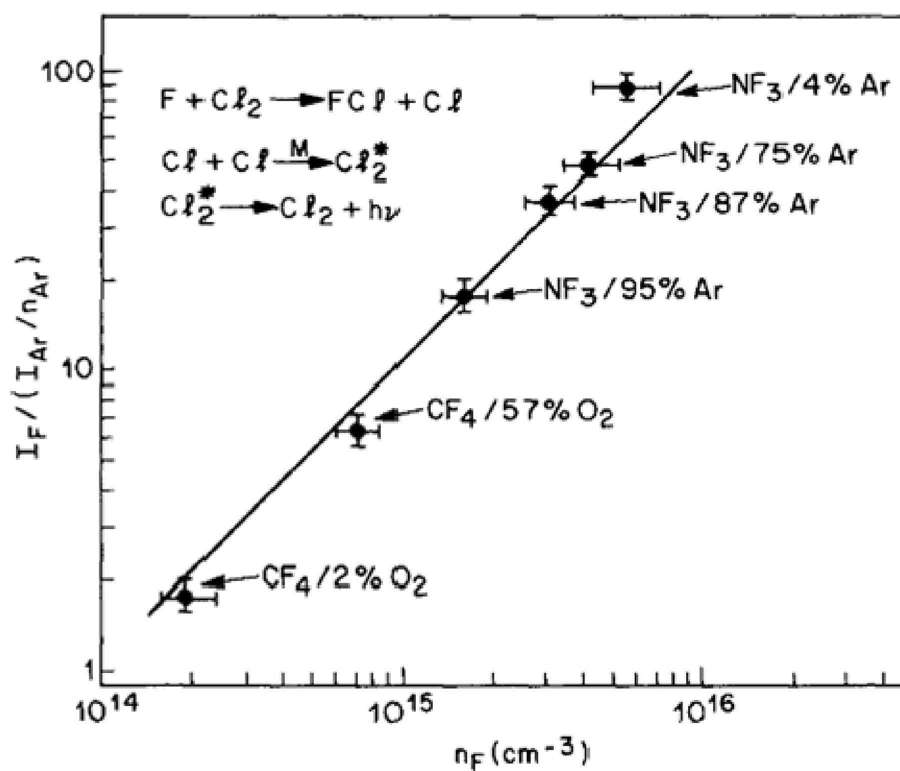

Figure 2.3 Correlation between F-atom emission normalized to Ar emission and number density $I_F/(I_{Ar}/n_{Ar})$, and fluorine atom number density n_F. (after Donelly.[63])

2.3 Electromigration test setup

The isothermal electromigration test is performed on the patterned Cu metallization which resembles the NIST structure with four Kelvin contact pads.. The test system was built around a probe station (Signatone s-1160) with a hot chuck. Figure 2.4 shows the schematic configuration of EM test setup. The chuck temperature can be controlled between 20ºC and 200ºC with an electrical heater and a heat exchanger. The current was provided from a programmable power source (E3645A, Agilent Technology, Inc., Santa Clara, CA). The potential drop along the test line was monitored by a digital multimeter (HP 3478A). The EM test was controlled by the software developed using the National Instruments Labview® version 7.2. The detailed algorithm of the EM test will be described in Chapter VI.

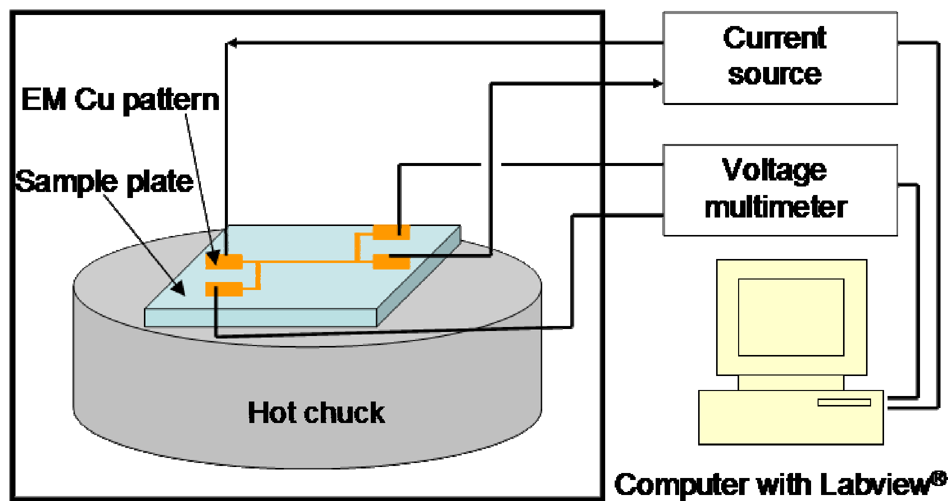

Figure 2.4 Schematic configuration of EM test setup. (drawing is not in scale)

2.4 Physical and chemical characterization

Dektak profilometer

The step height was measured by a Dektak III profilometer (Veeco Metrology Group, Santa Barbara, CA), which can accurately measure step heights from below 100Å to over 50 microns. Measurements are made electromechanically by moving the sample beneath a diamond-tipped stylus whose radius is 12.5 um. The high precision stage moves a sample beneath the stylus at a programmed length and speed. The stylus is mechanically coupled to the core of a LVDT (linear variable differential transformer). As the stage moves the sample, the stylus rides over the sample surface. The surface variations cause the stylus to be translated vertically. Electrical signal corresponding to the stylus movement is produced as the core position of the LVDT changes respectively. An analog signal proportional to the position change is produced by the LVDT, which in turn is conditioned and converted to a digital format and displayed on the monitor. The surface roughness can also be calculated based on the line scan of the surface topology.

Atomic force microscopy

Atomic force microscopy (AFM) is usually used to study film surface morphology or surface roughness. Similar to the profilometer, the surface roughness can be obtained from AFM measurement. AFM can provide a 3-D map of the surface, too. Figure 2.5 shows a schematic of AFM system. An AFM system consists of a cantilever with a sharp tip which is typically silicon or silicon nitride, a laser source, and a photodetector. When the tip is brought to proximity of a sample surface, the cantilever defection occurs. The

defection of cantilever is measured by the incident laser which reflects on the top surface of the cantilever to the photodetector. AFM can work at contact model or tapping model. In the contact mode, the probe tip is dragged across the surface and the resulting image is a topographical map of the sample surface. In the tapping model, instead of mechanically scanning the sample surface, the cantilever is driven to oscillate up and down at near its resonance frequency by a small piezoelectric element mounted in the AFM tip holder to reduce friction force and surface damage. The oscillation amplitude changes depending on the surface topography, resulting in a high-resolution image of the sample surface.

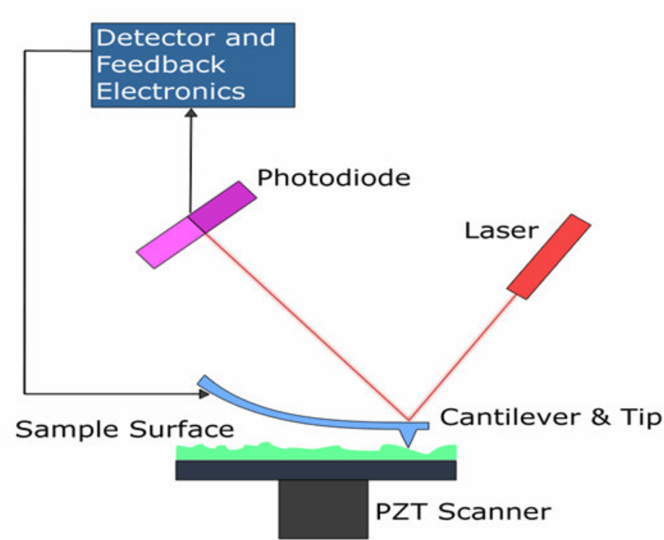

Figure 2.5 Schematic of AFM system. (after www.vikipedia.org)

Scanning electron microscope

Scanning Electron Microscope (SEM) can provide high resolution images of a sample surface. Figure 2.6 shows the schematic diagram of a SEM system. Electrons thermally emitted from the tungsten tip are accelerated by the electric field inside of the electron gun assembly. The highly coherent electron beam strikes the sample surface and results in the emission of backscattered and secondary electrons, which are collected by the Evehart-Thornely detector. Scanning coils deflects the electron beam in a television-like raster over the surface of the sample. The signal collected by the E-T detector is amplified and converted into a digital image. Image contrast arises from secondary and backscattered electrons. The emission of secondary electrons depends on the incident angle, therefore the SEM image is sensitive to the morphology of the sample surface. Secondary electron emission is also affected by the atomic weight of the surface material.

Practically, the sample surface charge can cause noises in the SEM image, and lower the resolution. Therefore, the sample surface is usually coated with a thin layer of highly conductive metal, such as gold-palladium (Pd/Au), which can effectively prevent the surface charging and avoid the image distortion. In addition, most materials, especially those with low atomic number, are not effective to emit the secondary electron. The Pd/Au coating film is rich in secondary electron emission, which increases the contrast and results in the formation of high resolution images.

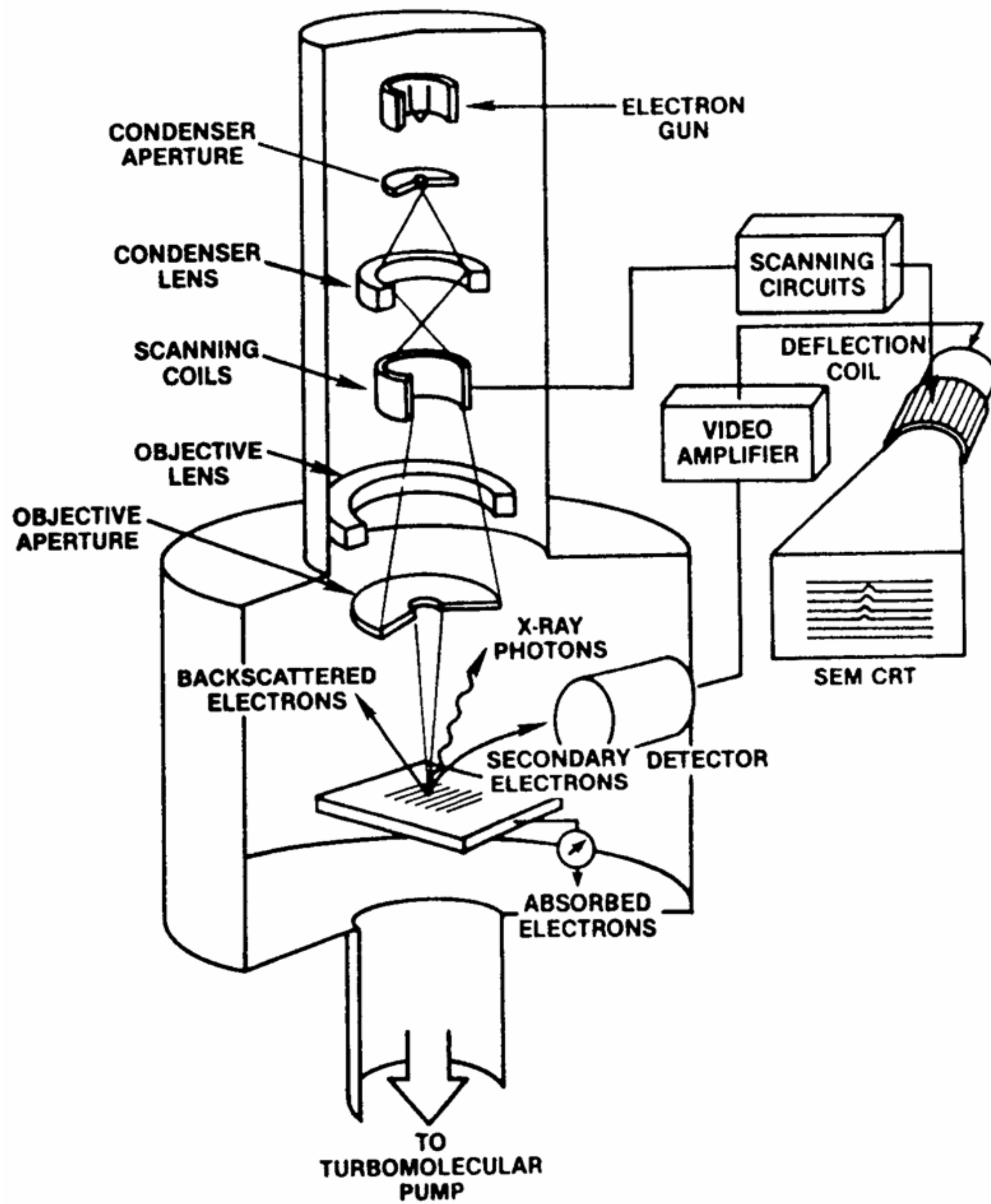

Figure 2.6 Schematic of SEM system (Jeol JSM-6400)

Energy dispersive x-ray spectrometer

Energy dispersive x-ray spectrometer (EDX) is frequently integrated into the SEM system for a quick chemical analysis. During EDX analysis, the electron beam strikes the target material to trigger the release of x-ray, which is the characteristic of the atom (or element) from which it is released. Figure 2.7 illustrates the generation of x-ray. Electrons in the inner shell are at lower energy states, while electrons in the outer shell are at higher energy states. Primary electrons bombarding the atom can knock off shell electrons out of their orbits, which are replaced by electrons from shells further out. Since there is a difference between the energy states, the excess energy is released in a form of X-ray. (The energy may also be released in other form such as Auger electron, which is not considered here.) The x-ray generated from any particular element is the characteristic of that element. Therefore, EDX can be used to identify the element which is present at the target spot. However, EDX is not sensitive to the chemical binding states, therefore can not tell the chemical state of the present element. Due to the high energy of the incident electrons, EDX can sample a volume about 1 cubic micrometer. Therefore, EDX is not considered as a surface analysis technique. In this research, the EDX system was integrated into the SEM system for a quick chemical analysis.

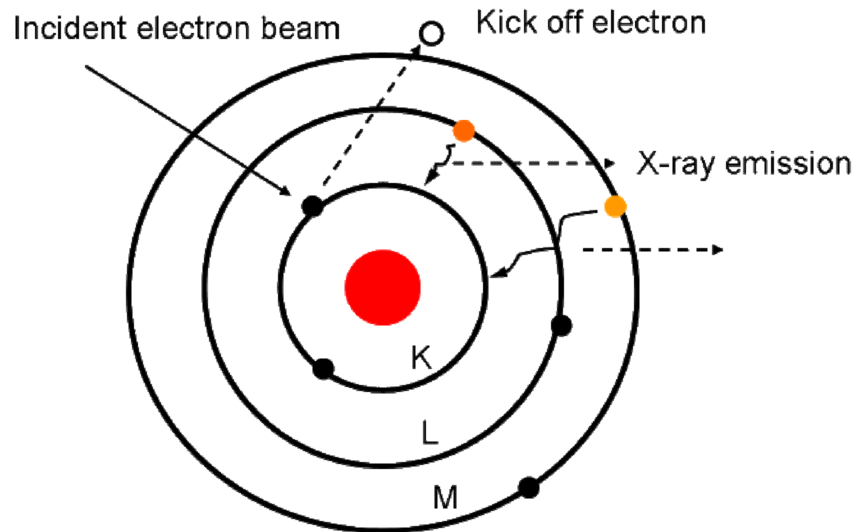

Figure 2.7 X-ray generation during EDX analysis

X-ray photoelectron spectroscopy

X-ray photoelectron spectroscopy (XPS), also known as electron spectroscopy for chemical analysis (ESCA), not only can identify the present element, but also tell the chemical binding structure. The detection depth is about 0.5 to 3 nm, therefore, XPS is a surface analytical technique. During XPS analysis, an X-ray beam strikes the sample surface. The core level electrons may be ejected, which is known as photoelectron effect.[66] Figure 2.8 illustrates the photoelectron emission process. The kinetic energy of the photoelectron is correlated to the binding energy in the following equation.

$$BE = hv - KE - \Phi \qquad (2.7)$$

where BE and KE are the binding energy and kinetic energy of photoelectron, respectively. hv is the energy of incident X- ray source, and Φ is the work function of the spectrometer. A unique property of XPS rests on the fact that the core level electrons nearest to the valence shells often exhibit shifts in binding energies due to the specific chemical environment of the atom. By identifying the XPS peaks and the binding energy shift for a given peak, the element and its chemical binding status on the sample surface can be obtained. Quantitative analysis with XPS is accomplished by determining the atom fractions of each constituent and normalizing to 100% of the detected element. Therefore, XPS is a powerful technique for characterizing surfaces or residues in cases where the composition is unknown. In this study, an Axis XPS instrument (Kratos Analytical Inc, Chestnut Ridge, NY) equipped with a monochromatic Al Ka (1486.6 eV) X-ray source was used to investigate the chemical bonding state of the target film. The carbon C 1s emission at 284.6 eV was used as a reference to correct the charging effect.

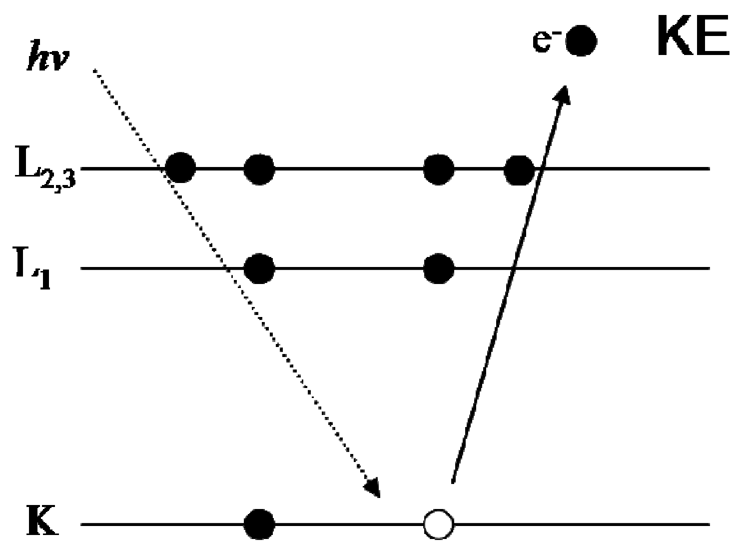

Figure 2.8 Photoelectron emission in XPS analysis.

X-ray diffraction

X-ray diffraction (XRD) is a common non-destructive analytical technique which reveals information about crystal structure, gain size, and preferred orientation in a polycrystalline film. This technique is based on observing the diffraction intensity of an incident X-ray beam. The atoms in a crystal are considered as lying in a series of planes of certain interplaner spacing. Due to the periodic nature of the crystalline, the diffraction occurs from the stacks of parallel planes. As shown in Figure 2.9, W. L. Bragg derived a simple relationship about the diffraction and the crystal structure in terms of reflections from the crystal planes.[67]

$$2d_{hkl}\sin\theta = n\lambda \qquad (2.8)$$

where d_{hkl} is crystal plane distance, hkl is miller index, θ and λ are the incident angle and wavelength of the X-ray, respectively, n is an integer (the order of diffraction). The broadened Bragg peak is usually correlated to the grain size of film by the Scherrer equation,

$$G = \frac{K\lambda}{FWHM\cos(\theta)} \qquad (2.9)$$

where K is constant, FWHM is the full width of half maximum at 2θ. The broadened peak also includes “instrumental” factors such as detector slit width, area of specimen irradiated, possible presence of $K\alpha_2$ component in the X-ray beam etc. The contribution from these factors must be deconvoluted from the observed peak. In this study, the TiW and Cu films were characterized by a Bruker D8 Power X-ray diffractometer equipped with CuKα x-ray ($\lambda = 1.5418 Å$) radiation. The preferred orientation is identified by the

position of the diffraction peak. The grain size was derived by the Scherrer equation due to the broadening effect.

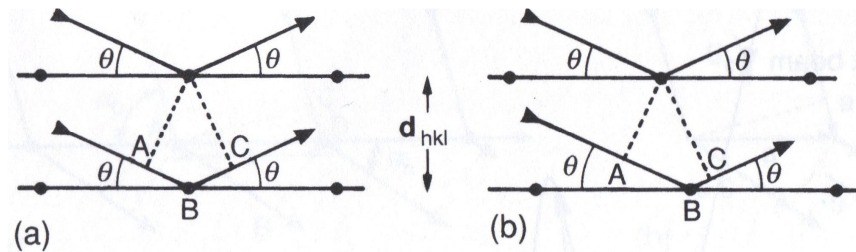

Figure 2.9 Bragg's law reflection: (a) rectangular grid, AB=BC, (AB+BC) = $2d_{hkl}\sin\theta$; (b) general case AB ≠ BC, (AB+BC) = $2d_{hkl}\sin\theta$. (after Hammond.[67] p.164)

CHAPTER III

GRAIN SIZE EFFECT ON PLASMA-BASED COPPER ETCH PROCESS*

The plasma etching process is affected not only by the plasma conditions, but also the microstructure the target film. Previous studies on the plasma-based Cu etch process were carried out on a given Cu film, i.e, the Cu film microstructure is fixed. The influence of Cu microstructure to the etch process has not been explored. In this chapter, a sputtering deposited Cu film was annealed at high temperatures. The temperature effect on the Cu microstructure and its influence to the Cl_2 plasma-Cu reaction process was investigated. This study provides high valuable information to the practical production process.

3.1 Experimental

The dual-layer TiW (20 nm)/Cu (240 nm) film was deposited sequentially in one pump down onto a thermally oxidized silicon substrate by DC sputtering. The background pressure of the chamber was 10^{-7} Torr. The TiW film was used as a diffusion barrier and adhesion layer for the Cu film. Subsequently, the sample was annealed in a tube furnace for 30 minutes under the atmosphere of forming gas, i.e., N_2/H_2 (90%/10%). The annealing temperature varied between 250°C and 400°C.

---

*Part of data reported in this chapter is reproduced from “Grain Size Effect on Plasma-based Copper Etch Process”, by Guojun Liu, Yue Kuo, Shafaat Ahmed, Denis N. Buckley, and Tanjim Tanaka-Ahmed, *Journal of the Electrochemical Society*, 155(6), H432-437 (2008), by permission of ECS-The Electrochemical Society.

The sheet resistance of the Cu film was measured using a four-point probe. The Cu film resistivity was calculated with the Cu film sheet resistance and the Cu layer thickness. The film's surface roughness was measured with an atomic force microscope (AFM). The microstructure was characterized with a scanning electron microscope (SEM) equipped with an energy-dispersive X-ray spectroscopy (EDS) and an X-ray diffractometer (D8, Bruker). The broadening of the x-ray diffraction (XRD) pattern peak is mainly attributed by the size of the diffracting crystalline. It is also affected by the instrumental factors such as detector slit, area of specimen irradiated, etc.[67] This instrumental effect on the peak broadening was deconvoluted from the shape and size of the peak. The average grain size G in the film was estimated using Scherrer's equation[67]

$$G = \frac{K\lambda}{FWHM\cos(\theta)} \tag{3.1}$$

where θ is the diffraction angel, FWHM is the full width of half maximum at 2θ, λ is wavelength of the x-ray source, which is 1.54Å, and K = 0.94 for the instrument.

The detail description of the Cl_2 plasma-based Cu etching process could be found in Chapter I. Briefly, the Cu film was coated with a positive photoresist and patterned with a line-and-space mask using the mask aligner. The sample was then exposed to the Cl_2 plasma in the RIE reactor, which had a parallel plate electrode configuration and was operated at 600 W, 60 mTorr, and Cl_2 flow rate of 12 sccm. After plasma exposure, the sample was removed from the reactor and dipped in a dilute HCl (6 H_2O:1 HCl) solution for 1 minute, which totally dissolved the $CuCl_x$ layer. After stripping the photoresist

layer, the Cu conversion and $CuCl_x$ formation rates were calculated from thickness of the $CuCl_x$ layer and the consumed Cu layer.

3.2 Microstructures of Cu films

Figure 3.1(a) shows XRD patterns of the as-deposited and annealed Cu films with the annealing temperature between 250°C and 400°C. A strong (111) diffraction peak and a much weaker (200) peak are observed in all samples. No TiW peak was observed, which indicated the thin TiW layer was probably amorphous or too thin to be detected. The (111) to (200) peak area ratios of all samples are about the same, i.e., 5, irrespective of the annealing temperature. Figure 3.1(a) also shows that the FWHM of the (111) peak decreases with the increase of the annealing temperature. According to equation (1), the Cu gain size increases with the increase of annealing temperature, as shown in Fig. 3.1 (b), which is consistent with the result of the chemical vapor deposited Cu film.[68] From the thermodynamic point of view, within the grain, since all atoms are lined up in crystallographic positions, the material is at the low energy state. At grain boundaries, atoms are at higher energy states because the existence of many unsatisfied or distorted bonds.[7] During the grain growth, the total energy of the film decreased due to the reduction of the grain boundary area, i.e., increasing the grain size.

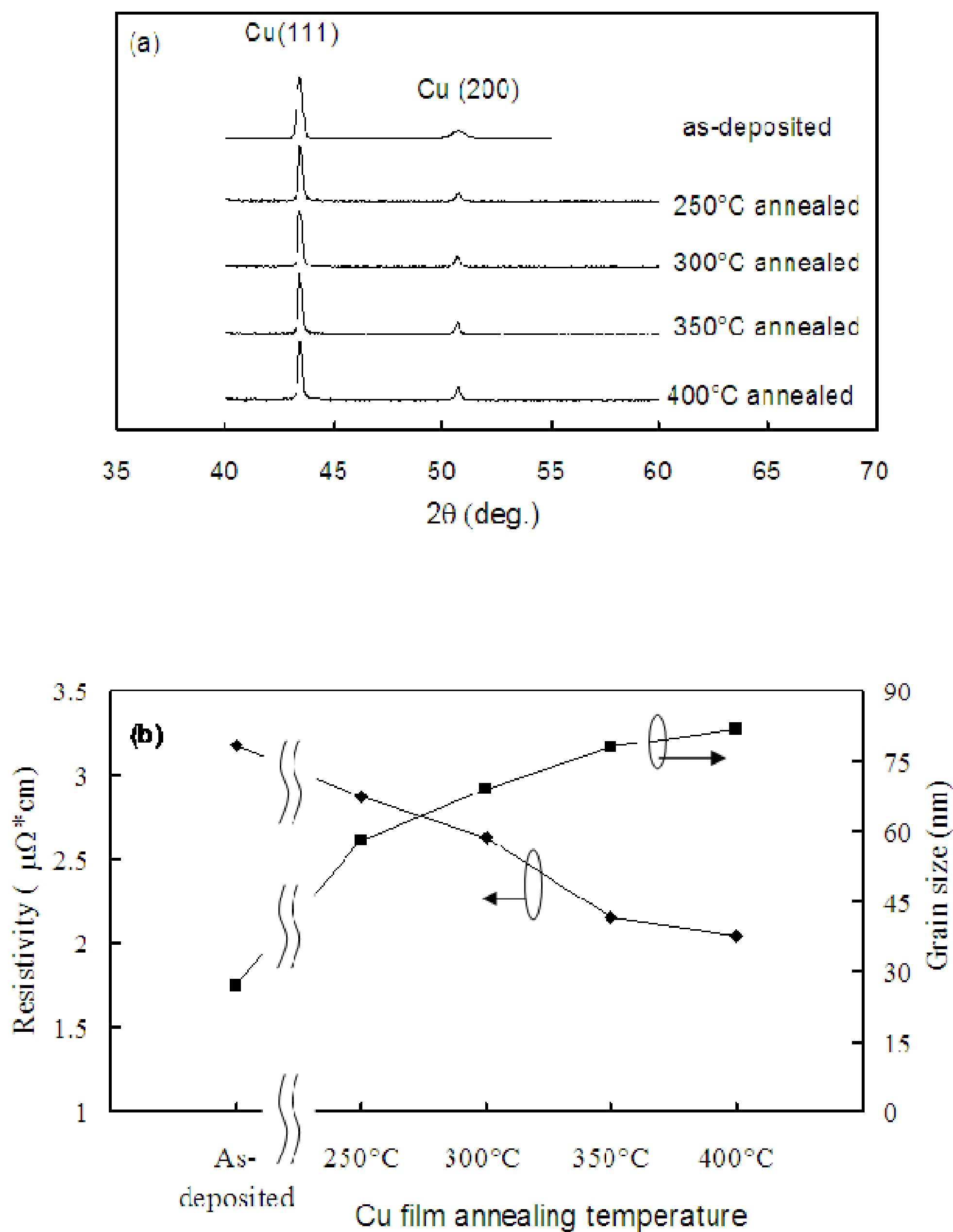

Figure 3.1 (a) XRD patterns of as-deposited and annealed Cu films. Annealing conditions: 250°C~400°C, forming gas H_2(10%)/N_2(90%), for 30 min; (b) Cu film grain size and resisitivity under (a) condition.

For the dual-layer TiW/Cu film, the sheet resistance (R_{sheet}) can be expressed by the following equation.

$$R_{sheet} = \frac{\rho_{Cu} / t_{Cu} \times \rho_{TiW} / t_{TiW}}{\rho_{Cu} / t_{Cu} + \rho_{TiW} / t_{TiW}} \qquad (3.2)$$

where ρ_{Cu}, ρ_{TiW}, t_{Cu} and t_{TiW} are the resistivities and thicknesses of Cu and TiW layer, respectively. The measured TiW resistivity was about $81.5\,\mu\Omega \bullet cm$, which did not change with annealing temperature.[69] The Cu film's resistivity was calculated using equation (3.2) and above measured numbers. Figure 3.1(b) shows that the Cu film resistivity decreases with the increase of the annealing temperature. The relationship between the grain size and the resistivity has been described by Mayadas and Shatzkes.[70] Since grain boundaries are randomly distributed, the electrons undergo specular reflection from boundaries parallel to the electron flow direction. Grain boundaries that transverse to the electron flow direction cause diffusive electron scattering with a reflection coefficient R ($0<R<1$). Harper and Cabral derived an equation relating the film resistivtiy with grain boundaries, ρ_G, to the grain size, G,

$$\rho_G / \rho_0 = 1 + 1.4(\lambda / G)R(1 - R) \qquad (3.3)$$

where ρ_0 is the resistivity of the film without grain boundaries, and λ is the intrinsic electron mean free path, i.e., 39 nm at the room temperature.[71] For the R value of 0.2 to 0.4,[70] when the grain size changes from 27 nm to 82 nm, the film resistivty should decrease by 23% – 39%. Fig. 1(b) shows the resistivity was decreased by 28.5%, 30.1%, 33.6% and 37.0% when the grain size increased from 27 nm to 58 nm, 69.8 nm 78.4 nm and 81.3 nm, respectively, which is consistent with the prediction of the equation (3.3).

Figure 3.2 shows the AFM images of the (a) as-deposited, (b) 300°C, and (c) 400°C annealed Cu film surfaces, respectively. The root-mean-square (RMS) roughness of the surface increased from 3.8 nm before annealing to 4.5 nm after 300°C annealing and to 11 nm after 400°C annealing. The grooves between grains also became wider as the annealing temperature was increased. A similar phenomenon of groove size enlargement after high temperature annealing was also reported on the electroplated Cu film.[72] This phenomenon may be attributed to the Cu surface diffusion that drives atoms on the free surface out of the grooved regions.[73] It may also be contributed by the vacancy diffusion. For example, excess vacancies may migrate to grain boundaries during the annealing, which creates free volumes and grooves.[74]

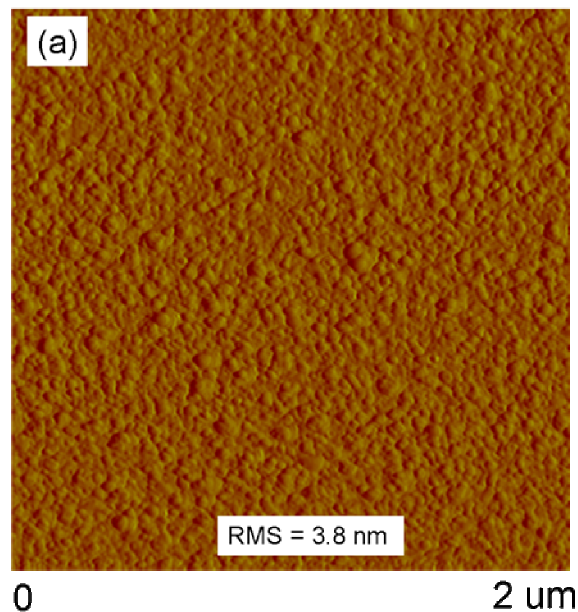

Figure 3.2 AFM images of the top surfaces of (a) as-deposited (b) 300 °C (c) 400 °C annealed Cu film.

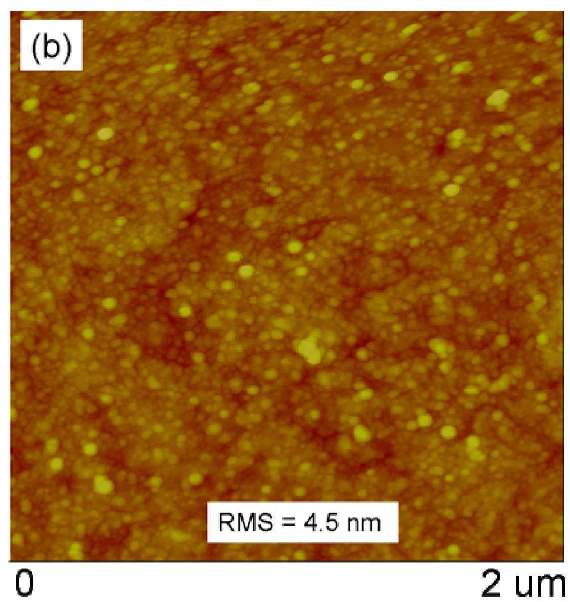

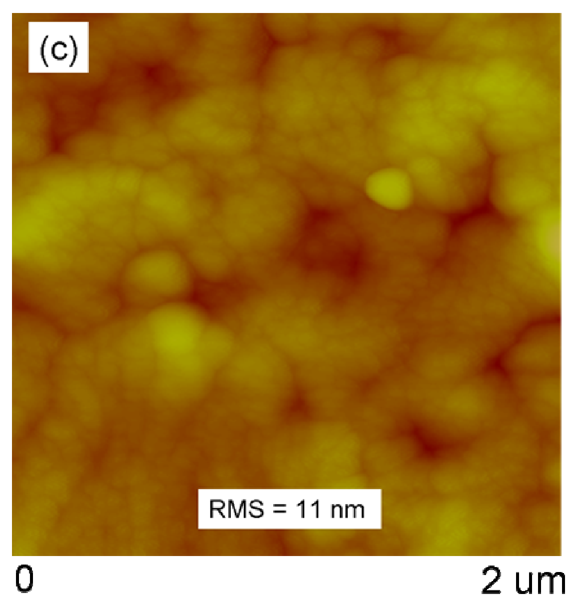

Figure 3.2 Continued.

3.3 Grain size effect on Cu chlorination process

Figure 3.3 shows the Cu conversion and $CuCl_x$ formation rates during the plasma-Cu reaction versus the original Cu film annealing temperature. The plasma exposure condition was fixed at 600 W, 60 mTorr and Cl_2 flow rate of 12 sccm. Both rates increase with the original Cu annealing temperature. However, when the annealing temperature was higher than 350°C, the temperature effect became less pronounced. This is consistent with the grain size vs. annealing temperature relationship in Fig. 1(b) in which the 400°C annealed Cu film has slightly larger grains than the 350°C annealed Cu film has. The ratio of $CuCl_x$ growth rate to the Cu consumption rate increased from 2.25 for the as-deposited Cu film to 2.32, 4.77, 5.3, and 5.43 for the 250°C, 300°C, 350°C, and 400°C annealed films, respectively. Therefore, the Cu consumption and $CuCl_x$ growth rates are related to the original Cu grain size.

When the Cl_2 plasma exposure time was less than 2 minutes, the Cu conversion rate was almost linearly proportional to the plasma exposure time.[17] The linearity implies that the $CuCl_x$/Cu interface reaction is critical to the Cu chlorination process. Otherwise, if the Cl diffusion through the $CuCl_x$ layer is the process limiting step, the Cu conversion rate vs. time should follow the parabolic relationship. Lee and Kuo studied the Cu conversion rate under the HCl plasma exposure at various substrate temperatures.[19] They reported that the activation energy was 0.53 kcal/mol, which is much smaller than the CuCl formation energy under the non-plasma exposure condition at room temperature, e.g. 28.3 kcal/mol.[75] Therefore, the Cu conversion rate in the plasma exposed process is not only dependent on the conventional chemical reaction mechanism. Other factors,

such as the microstructure of the original Cu film, the porosity of the $CuCl_x$ reaction product, and the ion bombardment energy, have major impacts to the reaction rate.[17]

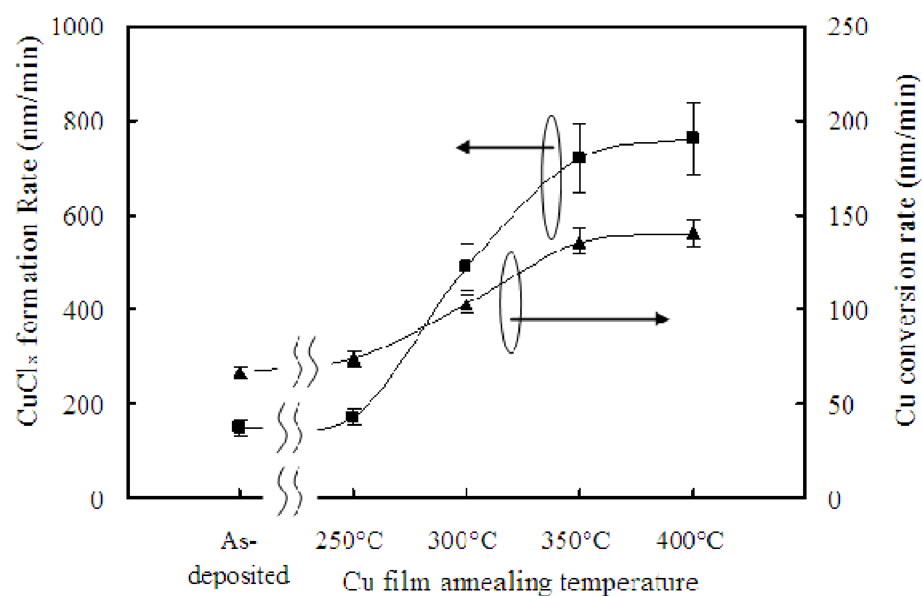

Figure 3.3 $CuCl_x$ formation rate and Cu conversion rate for the Cu films annealed at various temperatures.

Figure 3.4 (a) shows EDS diagrams of the $CuCl_x$/Cu/TiW stacks after the Cl_2 plasma exposure at 600 W and 60 mTorr for 1 minute. The peaks were assigned to Cu, Cl, and W, respectively. The Cl intensity in the film increases with the original Cu annealing temperature. The W and Cu intensities did not show apparent change for different Cu films. Meanwhile, Fig. 3.4(b) shows that the Cl/Cu ratio increases with the original Cu annealing temperature. Since the EDS sample volume is roughly 1 cubic micrometer, W in the bottom TiW is detected. The Cl and Cu elements in Fig. 3.4(a) are contributed from the whole $CuCl_x$/Cu stack. The ratio of Cl/Cu in Fig. 3.4 (b) is not the actual x value in the $CuCl_x$ layer. Since the reaction product $CuCl_x$ is not volatile, the amout of Cu atom should be approximately the same before and after the Cl_2 plasma exposure. Fig. 3.4 (b) can be considered as the indication of Cl content. It clearly shows that the larger the original Cu grain is, the more Cl is incorporated into the final $CuCl_x$ film. Since the bulk densities of Cu, CuCl and $CuCl_2$, are 8.92, 4.14 and 3.05 g/cm^3, respectively,[75] the more Cl is included in the $CuCl_x$, the more volume expands.

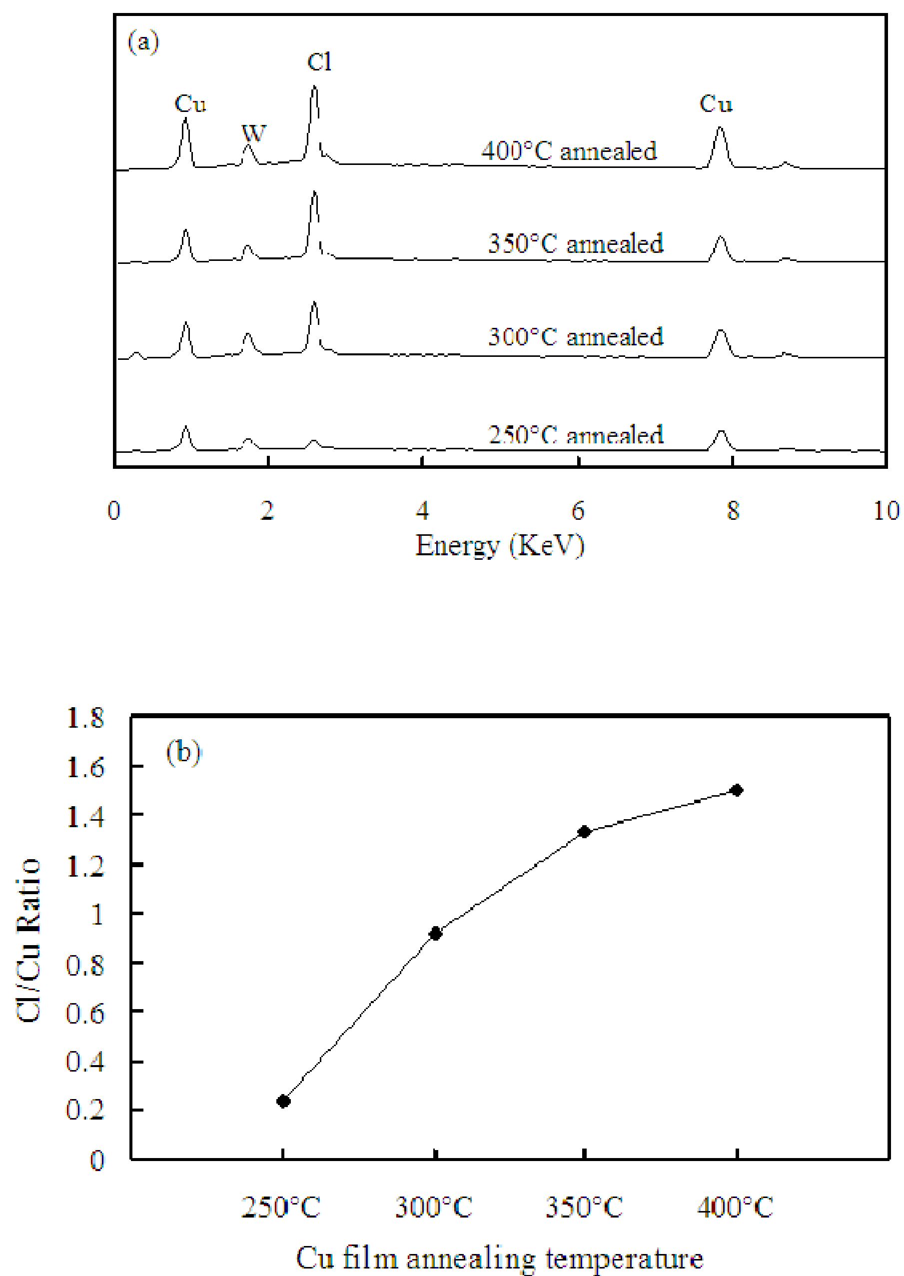

Figure 3.4 (a) EDS of 250°C, 300°C, 350°C and 400°C annealed Cu films after being exposed to Cl_2 plasma at 600 W, 60 mTorr, for 1 min; (b) the Cl/Cu ratio under (a) conditions.

Figure 3.5 (a) and (b) show cross-sectional and top views of the 250°C and 300°C annealed Cu films after being exposed to the same Cl_2 plasma, i.e. 600 W, 60 mTorr, for 1 minute. The top portion of the Cu film was converted into grainy and porous $CuCl_x$. The $CuCl_x$ layer converted from the 300ºC annealed Cu film is thicker than that from the 250ºC annealed Cu film. This is consistent with the trend shown in Fig. 3. In addition, the former layer contains larger grains and is more porous than the latter layer. The increase of Cu conversion and $CuCl_x$ formation rate with the increase of the original Cu grain size can be related to the Cl concentration on the surface and the porous structure of the $CuCl_x$ product. First, the high temperature annealed Cu film has a rougher surface than the low temperature annealed Cu film. The sticking probability of Cl to Cu is close to 1 up to about one monolayer.[76] Therefore, the former surface can adsorb more Cl atoms than the later surface. Cl radicals generated in the plasma are highly reactive and readily react with Cu. The high Cl concentration facilitates the surface reaction, i.e., the Cu conversion rate as well as the $CuCl_x$ growth rate. Second, the $CuCl_x$ formed from the high temperature annealed Cu is more porous than that from the low temperature annealed Cu, as shown in insets of Figs. 3.5(a) and (b). The more porous the $CuCl_x$ layer is, the easier for Cl radicals and ions are transported to the underneath fresh Cu, which enhances the Cu conversion process. The same phenomenon was observed in the Cl_2/N_2 plasma exposed Cu chlorination reaction.[77] Actually, it is difficult to separate the above two factors because they can influence each other. For example, it was observed that the high porosity $CuCl_x$ film contained a larger Cl concentration than the low porosity $CuCl_x$ film during the room temperature or high temperature plasma exposure.[17,5]

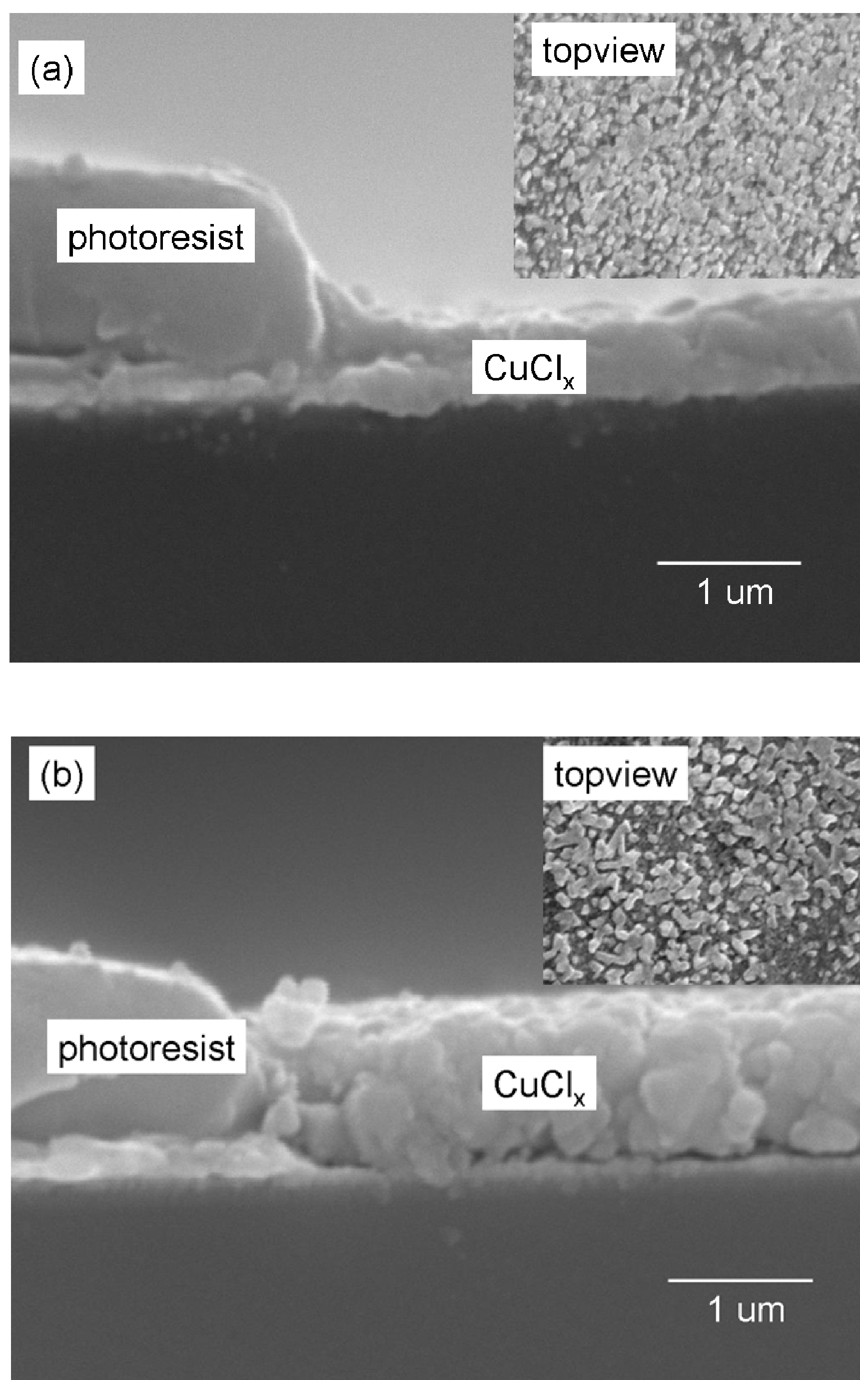

Figure 3.5 SEM cross-sectional and top views of (a) 250°C and (b) 300°C annealed Cu films after being exposed to Cl_2 plasma at 600 W, 60 mTorr, for 1 min. The inlets are the top views.

The high Cl concentration in the porous $CuCl_x$ film can provide more Cl to the underneath Cu for reaction than the less porous $CuCl_x$ film can. In short, Figs. 3.3, 3.4 and 3.5 results all confirm that the original Cu film's microstructure is critical to the Cu conversion process.

Cu chlorination is more than surface phenomena. For example, Cl adsorbed on the Cu surface can diffuse into the bulk film to facilitate the reaction process.[23] In addition, Cu can diffuse through the bulk region to the surface to react with the adsorbed Cl. For example, a tremendous increase of the Cu diffusion rate, up to four orders of magnitude, was observed when its surface was covered with a layer of Cl.[78] The Cu diffusion through the bulk film may play am important role in the $CuCl_x$ formation process. When the Cu film is covered with a monolayer of $CuCl_x$, the Cl sticking coefficient drops dramatically to 0.002.[76] Since the Cu chlorination process depends on the supply of Cl and Cu, the Cu conversion rate is controlled by either the rate of Cl diffusion to the fresh Cu site or the rate of Cu diffusion to the adsorbed Cl site. The Cu chlorination reaction may be governed by the Cabrera-Mott type field-assisted diffusion mechanism,[25] i.e., both Cu and Cl are quite ionic upon contact. The electric force between anion (Cl^-) and cation (Cu^+) promotes the diffusion. It is possible that Cu^+ diffuse faster than Cl^- because the radius for Cu^+ is much smaller than that of Cl^-, i.e., 0.96 vs. 1.81 Å.[75] Delamare and Rhead reported that the Cu^+ diffused much faster than the Cl^-.[79] Since the diffusion activation energy decreases with the increase of the Cu grain size,[80] the larger grain film may have a faster Cu self-diffusion rate than the small grain film does. The faster Cu

diffuses to the Cl sites, the quicker the $CuCl_x$ is formed, which could also explain the high Cu conversion rate of the originally high temperature annealed Cu film in Fig. 3.3

Figure 3.6 shows surface roughnesses of Cu films before and after Cl_2 plasma exposure followed by the removal of the top $CuCl_x$ layer. The original Cu films were annealed at various temperatures. The Cu surface roughness increased after high temperature annealing due to the grain growth and surface grooving, which was discussed in the Fig. 3.2 section. The Cu surface roughness increases dramatically after plasma exposure, especially for the high temperature annealed film. The roughness may be originated from the Cl_2 plasma-Cu reaction or due to the dilute HCl solution attack of Cu during the removal of $CuCl_x$. The latter assumption does not hold because in a separate experiment we observed that when the fresh Cu film was dipped in the same HCl solution for the same period of time as in the $CuCl_x$ removal process, its surface roughness remained almost the same as that before the dipping process. Therefore, the roughness of the Cu surface was caused by the plasma chlorination process.

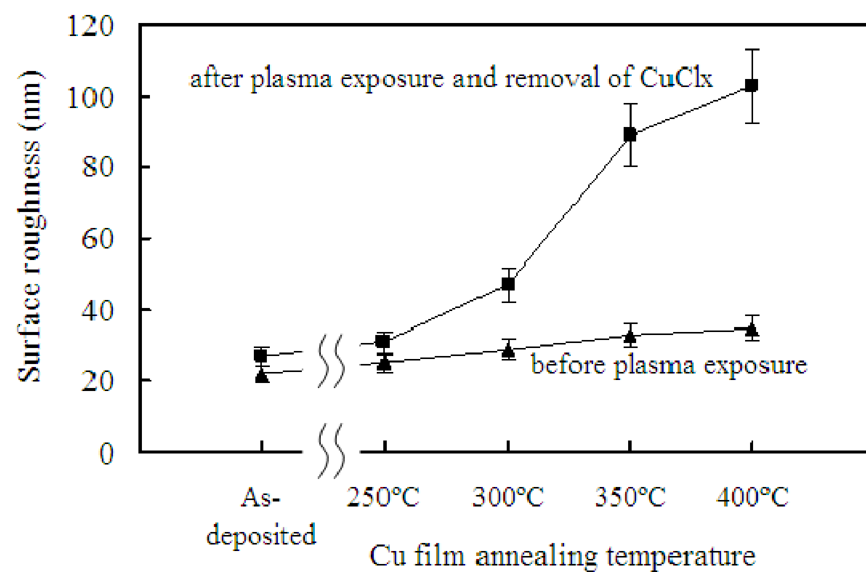

Figure 3.6 Surface roughness of the Cu film vs. annealing temperature, before and after plasma exposure and removal of $CuCl_x$. Plasma condition: 600 W, 60 mTorr, 12 sccm Cl_2, for 1 min.

The chlorination of polycrystalline Cu is not a layer-by-layer process. For example, under the non-plasma reaction condition, the Cl concentration continuously changed with depth,[79] which was explained by that the CuCl formation proceeded preferentially along the grain boundary.[26] The same kind of Cl concentration change was also observed in the HCl plasma exposed Cu film.[19] In order to verify this mechanism, Cu films with 3 different types of grain structures were exposed to the same Cl_2 plasma condition, i.e., 600 W, 60 mTorr, 12 sccm Cl_2, for 20 seconds, which was followed by the removal of $CuCl_x$ layer. Figure 3.7(a) sample, which was from the as-deposited Cu, has a surface rougher than that before plasma exposure, i.e., 5 nm vs. 3.8 nm. Figure 3.7(b) sample, which was from the 300ºC annealed Cu, has a surface much rougher than that before plasma exposure, i.e., 44 nm vs. 4.5 nm. Figure 3.7(c) shows the AFM scan line across the location indicated in Fig. 3.7(b). It has a volcano-like structure with various crater sizes. When the original Cu grain size was further increased, e.g., by annealing at 400ºC, the final Cu surface became extremely rough, e.g., 76 nm as shown in Figure 3.7(d). However, the crates had relative flat bottom surfaces, as shown in Figure 3.7(e). The rough topography is due to the different grain orientations in the original film and the preferential chlorination along the grain boundary. Raff reported the similar crater structure on the light-induced Cl_2 exposed Cu surface,[81] and the formation of the crater was attributed to the high Cu ionic diffusivity along the grain boundary.

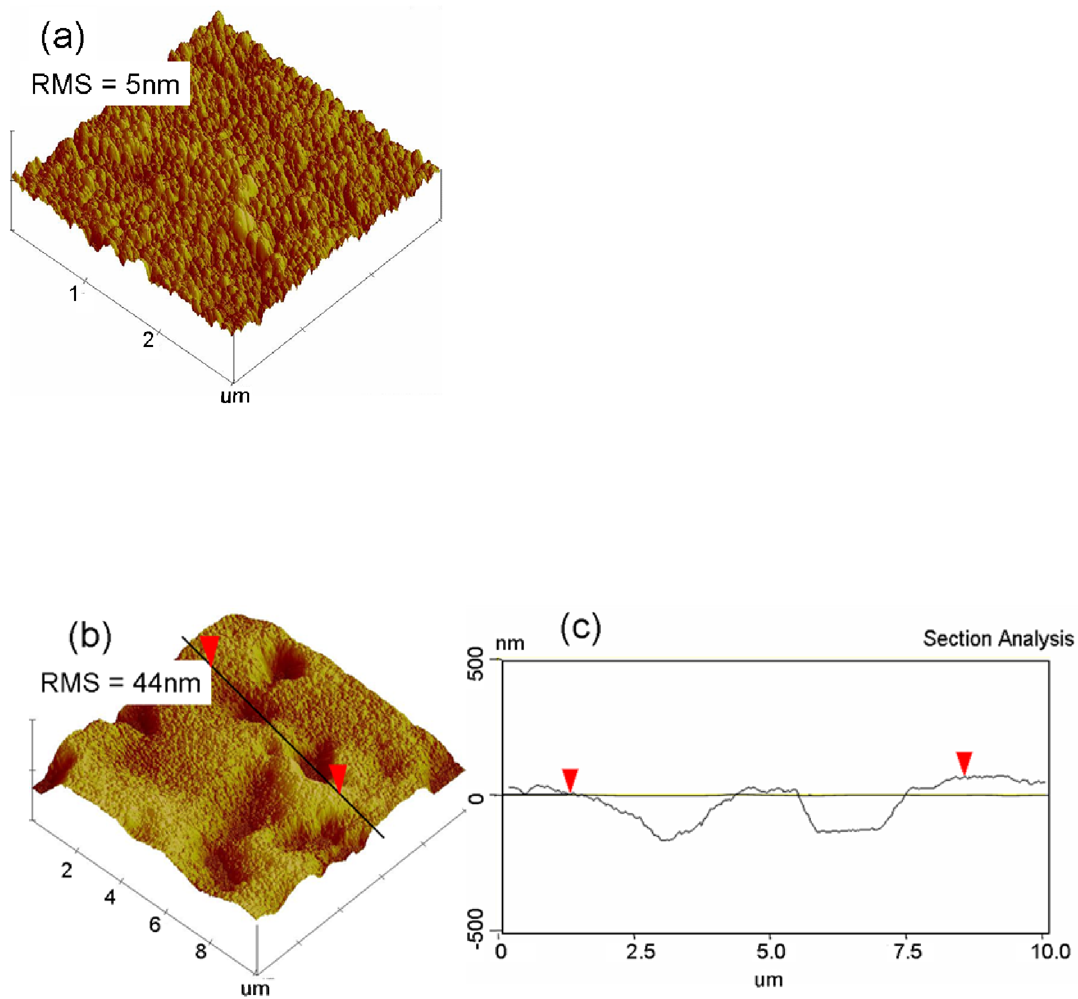

Figure 3.7 AFM of (a) as deposited, (b) 300°C annealed, (d) 400°C annealed Cu film after Cl_2 plasma exposure and removal of $CuCl_x$ layers. (c) and (e) are scan lines indicated in (b) and (d), respectively. Plasma condition: 600 W, 60 mTorr, 12 sccm Cl_2, for 20 seconds.

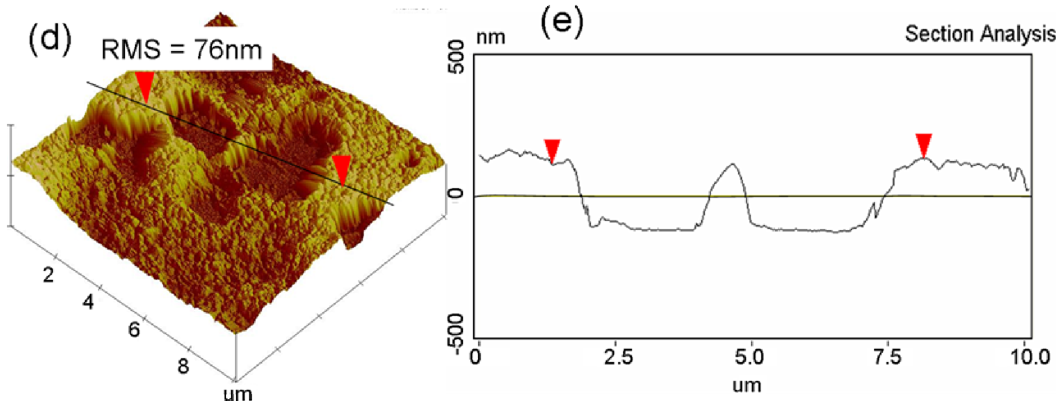

Figure 3.7 Continued.

Since Cl and Cu diffuse much faster along the grain boundary than within the bulk grain,[81] when the Cu film is exposed to Cl_2 plasma, the Cu chlorination proceeds faster along the grain boundary. For a Cu film, the grains are randomly oriented. When the chlorination reaction reaches the grain boundaries parallel to the substrate surface, the vertical Cu conversion rate will be slower than that along the grain boundary vertical to the surface. In addition, the original large surface groove of the high temperature annealed sample can trap more Cl than the non-annealed sample can.[82] Therefore, the chlorination rate along the grain boundary of large grains is faster than that of the small grains.

Previously, Kuo and Lee presented a simple model to explain the Cu chlorination process under the plasma exposure condition.[17] Results from this study can expand the model to include the grain size effect. Figure 3.8 shows the chlorination process for two Cu films with different grain size distribution. The reaction along grain boundary is much faster than through bulk Cu grain due to the fast inter-diffusion of Cu and Cl. Therefore, the grain boundaries in vertical direction contribute more to the Cu conversion rate than those in other directions do. For the small-grain film, as shown in Fig. 3.8(a), the path to the certain depth of the Cu film meanders along grain boundaries. For the large-grain film, as shown in Fig. 3.8(b), some vertical grain boundaries can reach deeper than those in Fig. 3.8 (a). The grain size difference, together with other factors discussed above such as Cu and Cl diffusion and $CuCl_x$ structure, resulted in a high conversion rate of the larger-grain Cu film and left a rougher surface.

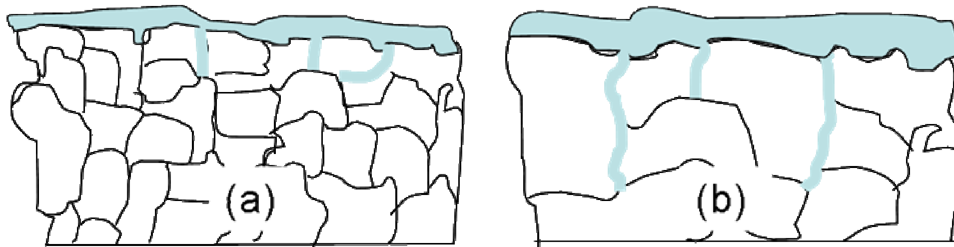

Figure 3.8 Schematic diagram of etching process with (a) small grain (b) large grain Cu film.

For a simplified mode, the following assumption is made: the Cu grains are spheres with uniform diameter r. Therefore, the ratio of the total grain boundary area to the total volume surrounded can be expressed by

$$\frac{4\pi r^2}{4/3\pi r^3} = \frac{3}{r} \tag{3.4}$$

This ratio would be 1.5/G using G = 2r, where the average grain size, G, was obtained in Fig.3.1. Figure 3.9 shows the Cu conversion rate as a function the ratio of grain boundary area to volume, i.e., 1.5/G. The Cu film with a higher value of 1.5/G showed a lower Cu conversion rate. The negative slope suggests that samples with many grain boundaries were chlorinated slower than samples with less grain boundaries. For the same amount of grain boundary, the former contained less volume than the latter did. Fig. 3.9 shows only the qualitative tendency, the detail correlation would also affected by the grain size distribution. However, the expected increase of the Cu conversion rate with decrease of grain boundary density should be consistent.

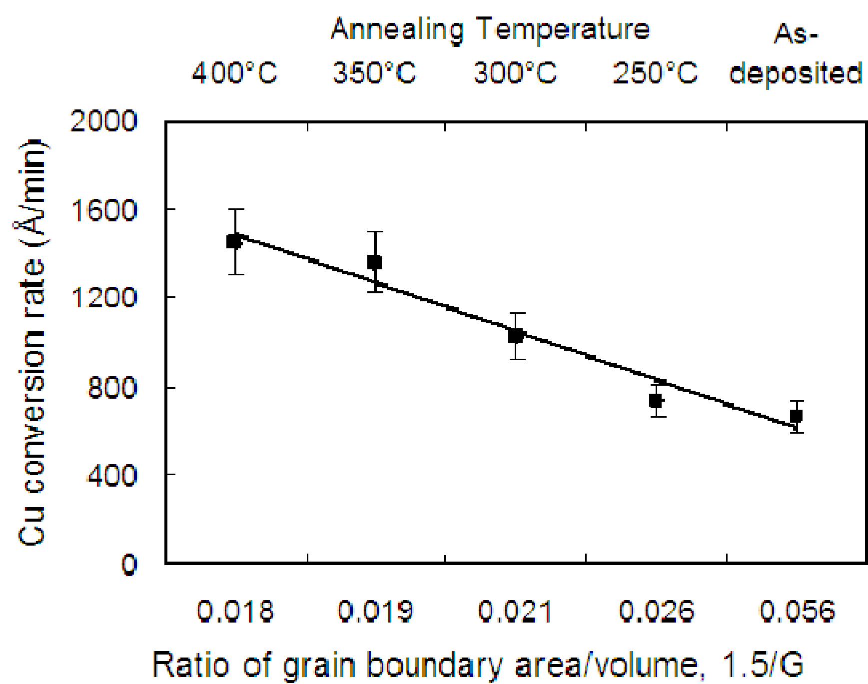

Figure 3.9 Cu conversion rate as a function of total grain boundary area to total grain volume (1.5/G) and fitted straight line.

3.4 Summary

The grain size effect on the Cl_2 plasma-based Cu etch process has been studied. With the increase of the annealing temperature, the Cu film's grain size increased, the resistivity decreased, and the surface roughness increased. These factors had major impacts to the plasma-Cu reaction. Under the same Cl_2 plasma condition, both the Cu conversion rate and the $CuCl_x$ formation rate increased with the grain size of the starting Cu film. Cu and Cl diffused through the bulk Cu grain at much slower rates than along the grain boundary. The reaction rate of the former was also much slower than that of the latter. The $CuCl_x$ layer's porosity and Cl content were also critical to Cu conversation process because they both influence the Cl supply mechanism. The grain size and boundary effects were further confirmed through examining the surface structure of the chlorinated Cu. This study delineated critical Cu microstructure effects on the plasma-based Cu etch process, which is potentially important for the fabrication of many microelectronic and optoelectronic products.

CHAPTER IV

ADDITIVE-GAS EFFECT ON CL_2 PLASA-BASED COPPER ETCH PROCESS AND SIDEWALL ATTACK*

An additive gas can dramatically change the plasma chemistry and ion bombardment, and consequently affect the etch profile. As discussed in Chapter I, the plasma/Cu reaction is the most critical step of the plasma-based Cu etch process.[16,17] In this chapter, the effect of the additive gas, such as Ar, N_2, and CF_4, on the plasma/Cu reaction was investigated. The influence of the additive gas to the sidewall attack of a pre-defined thick Cu pattern was also studied.

4.1 Experimental

A 200 nm thick Cu thin film was deposited on top of a 30 nm thick TiW film that was pre-deposited on a plasma enhanced chemical vapor deposition (PECVD) SiN_x coated Si wafer. The Cu film was coated with a positive photoresist layer. A thick Cu layer and a Ni/Pd hard mask layer were subsequently electroplated on the open areas of the pattern. Figure 4.1 shows the cross sectional diagram of the metal stack after the removal of the photoresist layer. The bottom thin Cu layer was then etched with a

---

*Part of data reported in this chapter is reproduced from "Additive-Gas Effect on CL_2 Plasma-Based Copper-Etch Process and Sidewall Attack" by Guojun Liu and Yue Kuo, *Journal of the Electrochemical Society*, 155 (2), H97-H102 (2008), by permission of ECS - The Electrochemical Society.

plasma-based process, which included a Cl_2/additive plasma exposure step followed by dilute HCl solution dipping. The detailed description of this process can be found in Chapter I. During the plasma process, the sidewall of the thick Cu layer was exposed to the plasma, which roughened the surface.

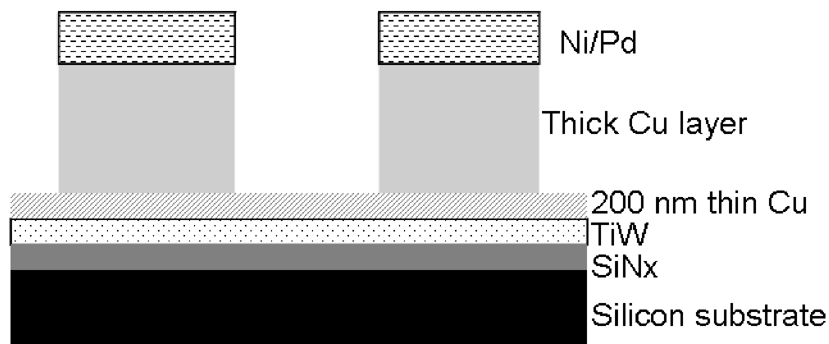

Figure 4.1 Cross-section diagram of the metal stack prior to plasma exposure.

The plasma exposure step was carried out in a reactive ion etching (RIE) chamber with a diode-type electrode configuration and a 13.56 MHz radio frequency (RF) generator connected to an automatic matching network. The pressure was fixed at 30 mTorr, the power was 600 W, and the total feed gas flow rate was 20 sccm. Three types of additive gases, i.e., Ar, N_2, and CF_4, were examined. The plasma phase Cl

concentration was monitored with an optical emission spectroscopy (OES) and estimated by the actinometry method.[8] The Cu consumption rate was calculated from the Dektak III profilometer measurement and the plasma exposure time. The composition and chemical structure of the plasma exposed Cu surface were analyzed with the energy dispersive spectroscopy (EDS) and electron spectroscopy for chemical analysis (ESCA). The Cu sidewall surface was examined with scanning electron microscopy (SEM).

4.2 Additive gas effect

Cu sidewall attack by Cl_2 plasma

Figure 4.2 shows the sidewall of the upper thick Cu layer after the bottom thin Cu layer was exposed to the Cl_2 plasma followed by HCl solution dipping. “Mouse bites” at the foot of the sidewall are observable. As discussed in the “Introduction” section, a possible mechanism of the sidewall attack is the surface charging or ion trajectory distortion.[29,31] However, this mechanism does not apply to this case because the Ni/Pd hard mask and the thick Cu layer are conductors that do not accumulate electrons on the sidewall. The “mouse bites” are probably caused by the excessive Cl reaction near the bottom interface.

The Cl_2 plasma/Cu reaction product $CuCl_x$ is porous and has a density much smaller than that of Cu, i.e., the densities of bulk Cu, CuCl, and $CuCl_2$ are 8.92, 4.14, and 3.05 g/cm^3, repectively.[83] When Cu is converted to $CuCl_x$, the volume expands. Since the horizontal space is limited, the volume expands to the vertical direction,[17] i.e., the $CuCl_x$ layer surface is higher than the original Cu surface. This volume expansion is

quite similar to the Si oxidation process. For the oxidation of the patterned silicon, due to the volume expansion, there was a large compressive stress at the silicon edge and a large tensile stress adjacently at the oxide edge.[84] The similar kind of stress difference could exist at the Cu/$CuCl_x$ interface. The high stress can facilitate the Cu–Cl bond formation.[32] Further studies are required to verify this point. In addition, the Cl/Cu ratio in the Cl_2 plasma exposed Cu is greater than 1.0.[85] Since the TiW barrier layer can not be etched with Cl in the absence of ion bombardment, an excessive amount of Cl may accumulate at the $CuCl_x$/TiW interface, which enhances the Cu consumption rate at the adjacent region. Therefore, the "mouse bites" at the bottom corner are contributed by the combination of the high film-film stress and the local excess amount of Cl.

The sidewall surface of the upper thick Cu layer was converted into a $CuCl_x$ layer during Cl_2 plasma exposure. After the HCl dip, the sidewall became rough because the Cl_2 plasma attacked the sidewall nonuniformly. In order to reduce the Cu sidewall attack, the Cl radical concentration in the plasma phase should be lowered or a protection layer needs to be formed. Gases, such as Ar, N_2 or CF_4, can either serve as diluents in the Cl_2 plasma, which reduce the Cl concentration, or form an inert surface coating the Cu sidewall, which protects the sidewall surface from excessive Cl attack. Each additive gas effect will be discussed in detail as follows.

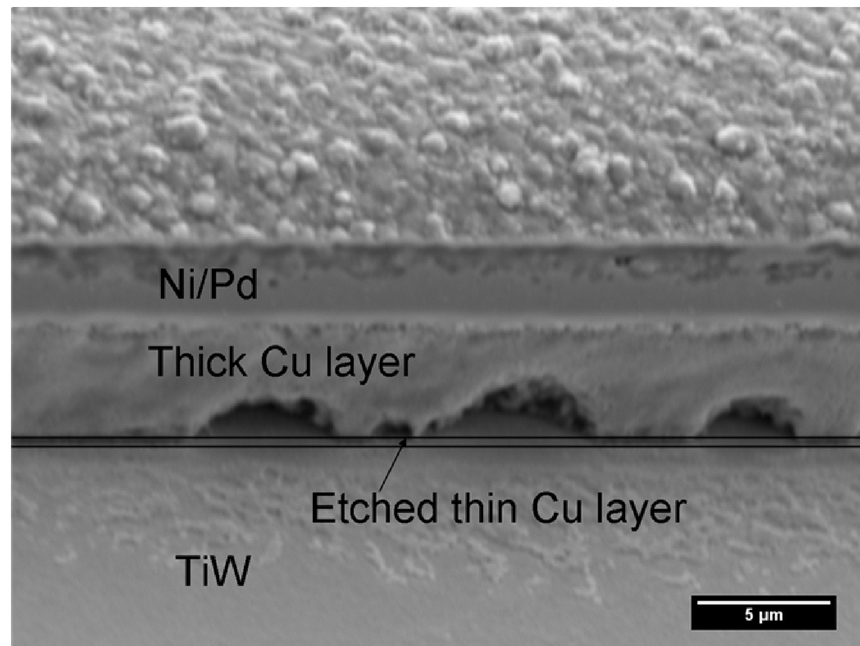

Figure 4.2 Cu sidewall profile after Cl_2 plasma exposure and removal of $CuCl_x$, plasma conditions: 600 W, 30 mTorr, 20 sccm Cl_2. The sample was tilt 55° for SEM imaging.

Ar additive effect

The Cl concentration and ion bombardment energy in the Cl_2 plasma are major contributing factors in the Cu consumption process.[17] The cathode self bias voltage,-V_{dc}, in a RIE process is a reference of the ion bombardment energy. Figure 4.3 shows the -V_{dc} increases monotonically with the increase of Ar concentration in the feed stream. As a neutral scatter,[86] the addition of Ar can increase the ion density therefore, enhance the ion bombardment effect.[87] The Cl concentration in the Cl_2/Ar plasma can not be estimated using the actinometry method, because the Ar concentration is too high, more than 5%.[8] Some researchers reported that the Cl concentration in the plasma phase increased with the addition of Ar, and attributed the Cl concentration increase to the dissociation of Cl_2 by meta-stable Ar atoms as the following reaction: [14]

$$Cl_2 + Ar^* \rightarrow 2Cl + Ar \qquad (4.1)$$

The energy of the meta-stable Ar atom, i.e., 11.9 eV, is higher than the bond-dissociation energy of the Cl_2 molecule, i.e., 2.5 eV. When the Ar concentration is low, the collision of Ar with Cl_2 molecules could increase the Cl radical concentration in the plasma phase, which compensates the loss of Cl due to the diluent’s effect.

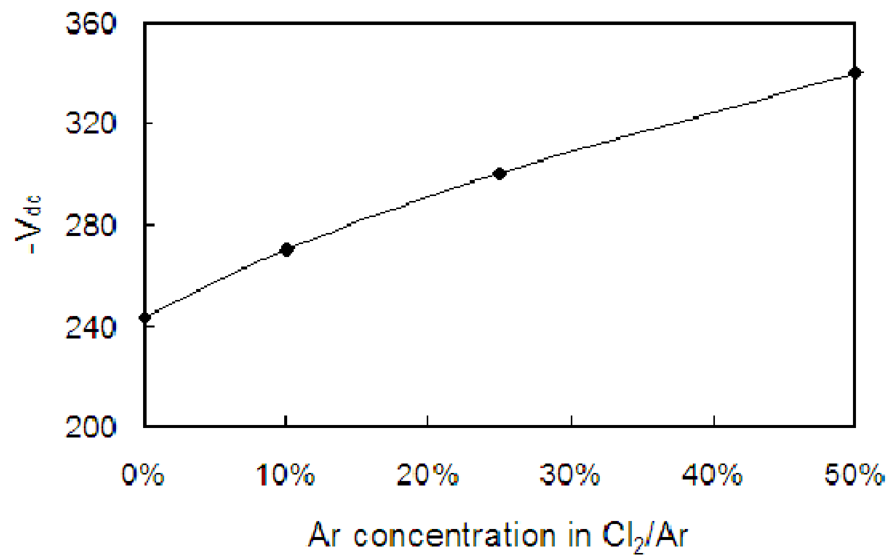

Figure 4.3 Effect of Ar concentration on cathode bias voltage in the Cl_2/Ar plasma at 600 W, 30 mTorr and 20 sccm total feed gas rate.

The Cu film consumption rate increases with the addition of Ar. For example, the Cu consumption rate in the Cl_2/Ar (20%) plasma was more than 2 times that in the Cl_2 plasma, e.g. 1100Å/min vs. 500A/min,[85] under the same pressure (20 mTorr) and power (600 W) conditions. The increase of Cu consumption rate is contributed by both increases of the Cl concentration and the ion bombardment energy. The former is the major reagent for Cu chlorination, while the latter enhances the reaction rate by disrupting Cu-Cu bond.[17]

Figure 4.4 shows the tilt view of the upper thick Cu sidewall after the bottom thin Cu film was exposed to the Cl_2/Ar (20%) plasma followed by the HCl solution dipping. Compared with the Cl_2 plasma exposed Cu sidewall of Fig. 4.2, the "mouse bites" phenomenon is greatly reduced, but the sidewall surface becomes rougher. Since the sidewall of the thick Cu layer is parallel to the direction of the ion bombardment, i.e., perpendicular to the wafer surface, the increase of the $-V_{dc}$ has little effect on the sidewall roughening. Instead, the high Cl concentration probably caused the roughness. It is possible that Cu reacts with Cu on the bulk grain different from that on the grain boundary, which also contributed to the non-uniform sidewall attack.

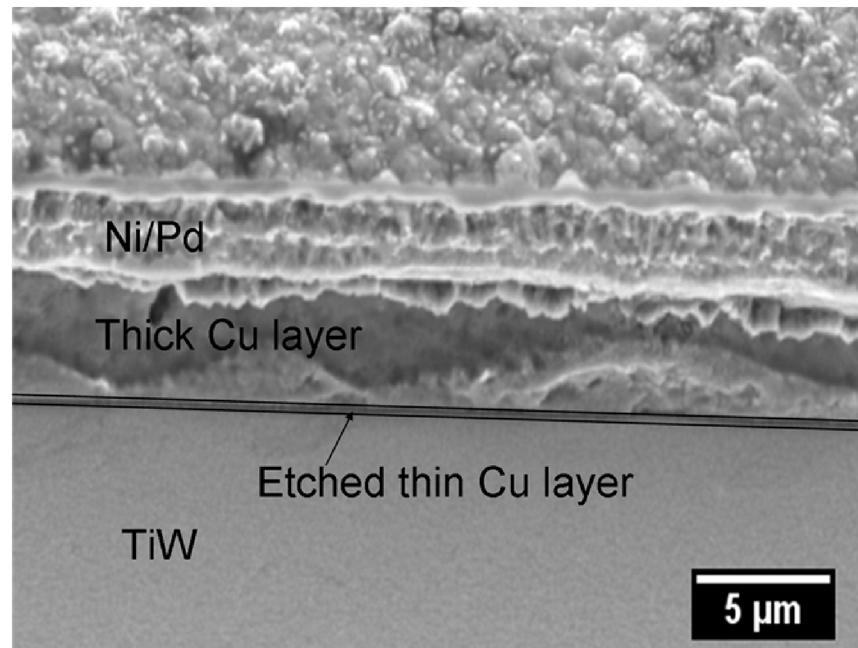

Figure 4.4 Cu sidewall after Cl_2/Ar (20%) plasma exposure and removal of $CuCl_x$. Sample was tilt 55° for SEM imaging.

N_2 additive effect

Figure 4.5 shows the influence of the N_2 concentration in the Cl_2/N_2 feed gas on the plasma phase Cl concentration and $-V_{dc}$. The Cl concentration decreases monotonically with the increase of the N_2 concentration, which is consistent with literature report.[88] Since N_2 is chemically inactive with a large N-N bond energy, i.e., 9.8 eV,[83] it mainly functions as a diluent to reduce the Cl concentration. The different trends of the Cl concentration in the Cl_2/N_2 and Cl_2/Ar plasma indicate that the addition of N_2 is less effective to promote the dissociation of Cl_2 than the addition of Ar does.[89] Fig. 4.5 also shows that $-V_{dc}$ increases with the N_2 concentration. The Cu consumption rate in the Cl_2/N_2 plasma was higher than that in the Cl_2 plasma. For example, under the same plasma condition, i.e., 600 W, 20 mTorr, and 20 sccm feed gas, the Cu consumption rate in the Cl_2/N_2 plasma was 1300Å/min, however, that in the Cl_2 plasma was 500Å/min.[85] Therefore, ion bombardment influences the Cu consumption process more than the Cl concentration does.

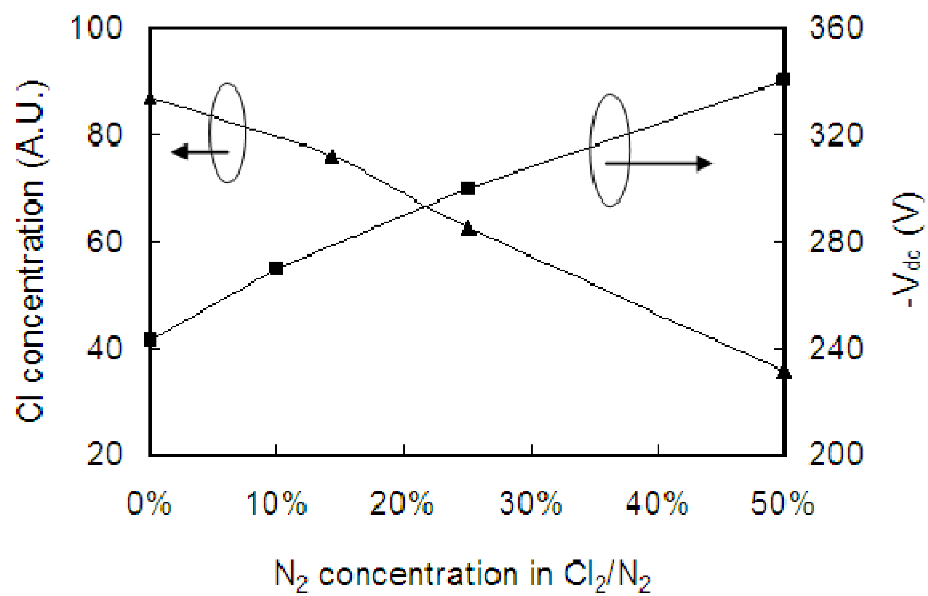

Figure 4.5 Effect of N_2 concentration on Cl concentration and cathode bias $-V_{dc}$ in Cl_2/N_2 plasma at 600 W, 30 mTorr, and 20 sccm total feed gas rate.

The microstructure of $CuCl_x$ can influence the Cu consumption rate. For example, when $CuCl_x$ layer is porous, ions can easily penetrate through it to reach the underneath fresh Cu layer for further reaction. Figure 4.6 shows the Cu surfaces after being exposed to (a) Cl_2 plasma and (b) Cl_2/N_2 (20%) plasma, respectively. The Cl_2/N_2 plasma exposed surface contains larger grains than the Cl_2 plasma exposed surface. Previously, it was reported that for the same plasma exposure time, the thickness of the $CuCl_x$ layer formed from the Cl_2/N_2 plasma exposure was 4 times that from the pure Cl_2 plasma exposure.[85] Therefore, the addition of N_2 into the Cl_2 plasma caused the reaction product $CuCl_x$ more porous. EDS analysis showed the Cl/Cu ratio of the Cl_2/N_2 plasma formed $CuCl_x$ was lower than that of the Cl_2 plasma formed $CuCl_x$, i.e., 1.1 vs. 1.6, which is consistent with the plasma phase Cl concentrations shown in Fig.4.5. Separately, it was observed that both $CuCl_x$ layers shown in Fig. 4.6 were completely soluble in the dilute HCl solution. The effect of the N_2 in the Cl_2 plasma on the Cu consumption rate and $CuCl_x$ porosity is similar to that of the substrate temperature effect, i.e., the high temperature enhanced the Cu consumption rate and increased the reaction product porousity.[17]

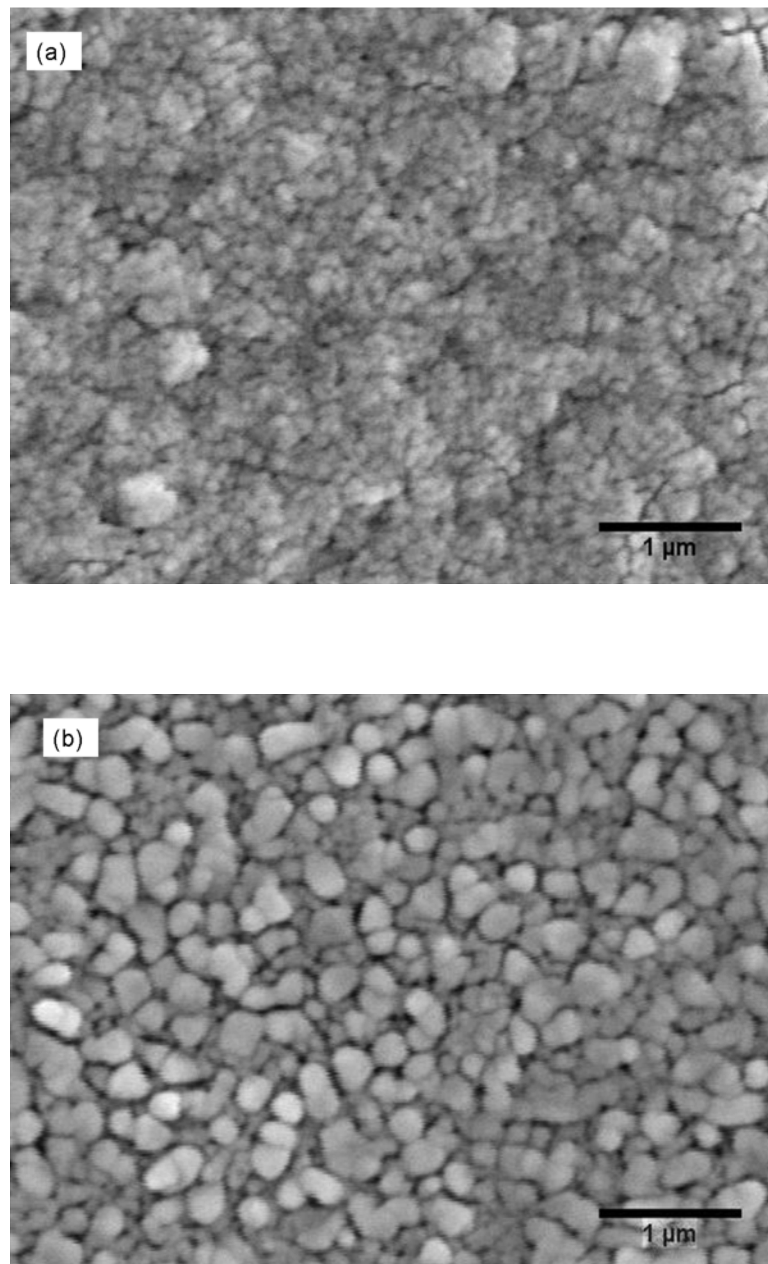

Figure 4.6 Top view of Cu film after being exposed to (a) Cl_2 and (b) Cl_2/N_2 (20%) plasma at 600 W, 30 mTorr, and 20 sccm total feed stream.

The Cu-N bond was detected on the N_2 plasma treated Cu-Ag eutectic surface.[90] For the Cl_2/N_2 plasma exposed Cu surface, it is difficult to differentiate Cu-Cl bond from Cu-N bond by ESCA because their binding energies overlay. A separate experiment was carried out to verify the Cu-N bond. Figure 4.7(a) shows binding energies of the Cu surface before and after being exposed to the N_2 plasma. The former has a binding energy of 931.6 eV, while the latter has a higher binding energy of 932.6 eV. The shift of Cu binding energy to a larger value is due to the formation of the ionic Cu.[91] Fig. 4.7(b) shows the N 1s peak of the N_2 plasma exposed Cu surface. The binding energy of 398.3eV is from the anionic nitrogen,[90] which is much lower than the covalent binding energy of N, i.e., 404 eV.[92] The N(1s)/Cu($2p_{3/2}$) peak area ratio is very low, similar to that of the N_2 plasma treated Cu-Ag surface.[90] It is difficult to estimate the N/Cu ratio. Kwon et. al. reported that the CuN_x surface layer lowered the Cu etch rate in the inductively coupled Cl_2 plasma.[12] This nitride layer may block the available surface for the etchant adsorption and reaction.[93] Because the Cu chlorination rate in the Cl_2/N_2 plasma was high, the CuN_x blocking efficiency on the horizontal surface was probably low. The CuN_x can be easily sputtered off by ion bombardment. However, because the sidewall is parallel to the ion bombardment direction, more CuN_x may be formed on the sidewall to protect it from vigorous Cl attack.

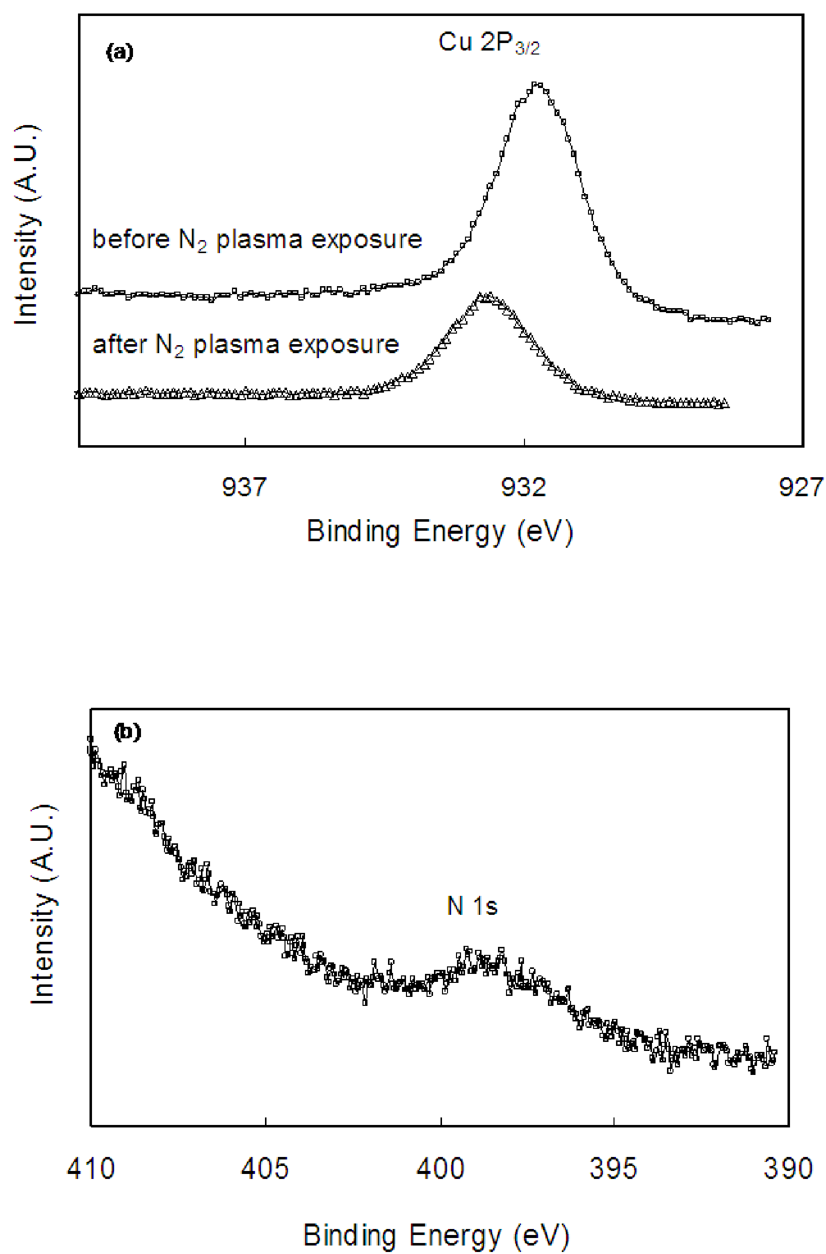

Figure 4.7 ESCA spectra of Cu surface (a) Cu $2P_{3/2}$ before and after N_2 plasma exposure, and (b) N 1s after N_2 plasma exposure.

Figure 4.8 shows the tilt view of the thick Cu sidewall after the bottom thin Cu film was exposed to the Cl_2/N_2 (20%) plasma followed by HCl solution dipping. No "mouse bites" are observed and the sidewall is smoother than those of Fig. 4.2 and 4.4. This result can be explained by the low Cl concentration in the plasma phase, the prorosity of the reaction product, the sidewall passivation, or the combination of above factors. Judging from the low Cl concentration, the sidewall $CuCl_x$ formation rate in the Cl_2/N_2 plasma should be lower than that in the Cl_2 or Cl_2/Ar plasma. As a result, the Cu sidewall attack is reduced with the addition of N_2 to the Cl_2 plasma. The combination of ion bombardment and the porous structure of the reaction product promote the Cu consumption in the vertical direction, leaving less Cl to attack the sidewall. Since high ion bombardment energy is unfavorable for the formation of CuN_x,[94] the chance of forming CuN_x layer on the sidewall is higher than that on the horizontal surface. Therefore, the nitride passivation layer could be another reason for the smooth sidewall.

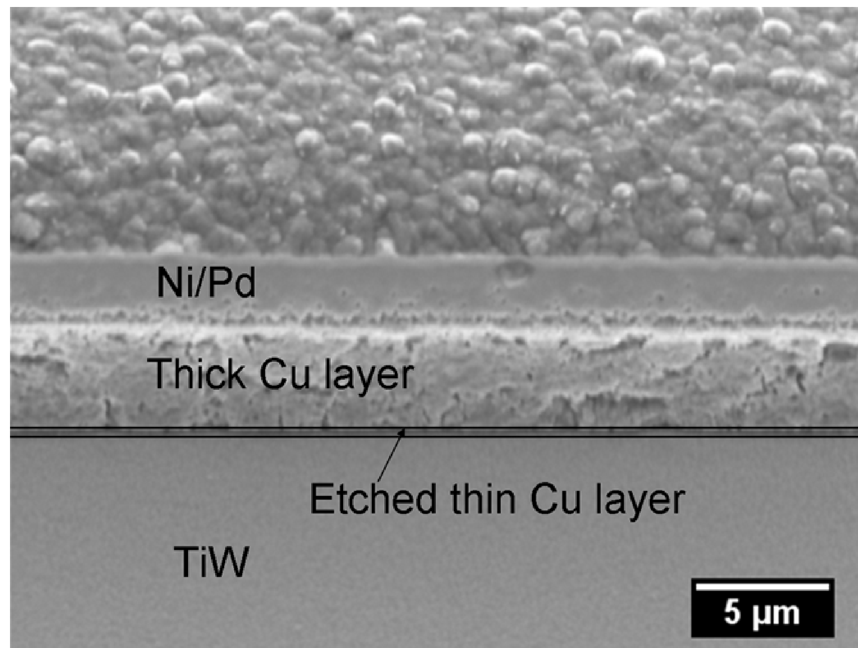

Figure 4.8 Cu sidewall after Cl_2/N_2 (20%) plasma exposure and removal of $CuCl_x$. Sample was tilt 55° for SEM imaging.

CF_4 additive effect

Figure 4.9 shows the effect of the CF_4 concentration on the Cl concentration and $-V_{dc}$ in the Cl_2/CF_4 plasma. The Cl concentration increases first with the CF_4 concentration, peaks at around 25% and then decreases with the further increase of the CF_4 concentration. The similar trend was observed in the inductively coupled Cl_2/CF_4 plasma.[95] The Cl concentration increase in low CF_4 concentration range was attributed to the CF_4-enhanced Cl_2 dissociation, i.e. through the reaction[95]

$$CF_2 + Cl_2 \rightarrow ClCF_2 + Cl \quad (4.2)$$

where CF_2 was from the dissociated CF_4. The Cl concentration decrease in the high CF_4 concentration range was due to the diluent effect, i.e., lowering the concentration of Cl_2. Fig. 4.9 also shows the $-V_{dc}$ increased monotonically with the increase of the CF_4 concentration. The $-V_{dc}$ change may be attributed to the fact that the C-F bond is stronger than the Cl-Cl bond, i.e., 488 kJ/mol vs. 243 kJ/mol.[83] Previously, it was observed that the magnitude of $-V_{dc}$ increased with the increase of the molecule's bond strength.[96]

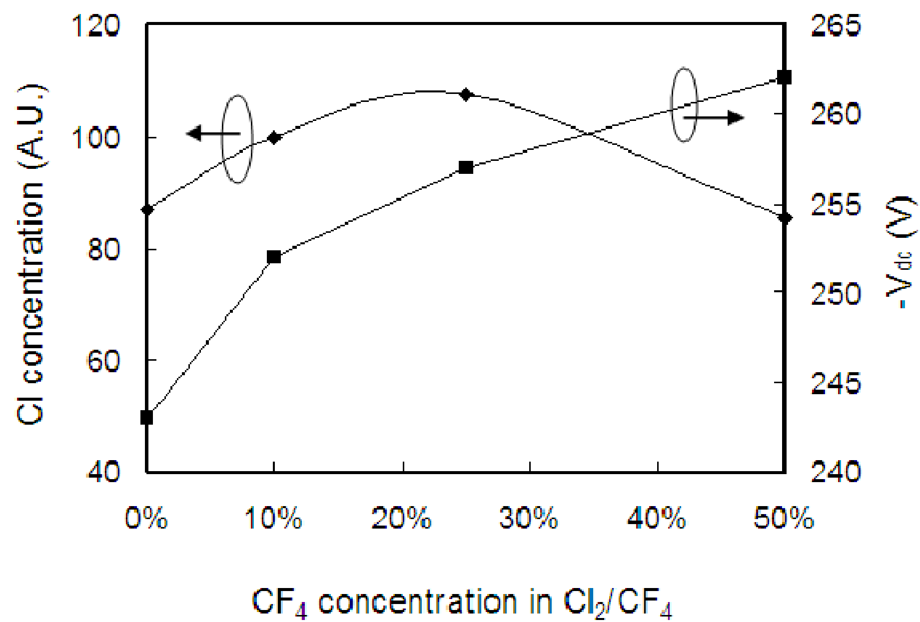

Figure 4.9 Effect of CF_4 concentration on Cl concentration and cathode bias $-V_{dc}$ in Cl_2/CF_4 plasma at 600 W, 30 mTorr, and 20 sccm total flow rate.

Although the addition of a small amount of CF_4 into Cl_2 plasma increased the Cl concentration and the ion bombardment energy, the Cu consumption rate was decreased. For example, the Cu consumption rate in the Cl_2/CF_4 (20%) plasma is lower than that in the Cl_2 plasma under the same plasma pressure (20 mTorr) and power (600 W) condition, i.e., 400A/min vs. 500A/min.[85] This is attributed to the change of the surface structure or composition. Figure 4.10 shows the ESCA spectra of the Cl_2/CF_4 (20%) plasma exposed Cu surface. The 685.5 eV peak in Fig. 4.10(a) is from ionic fluorides, such as CuF or CuF_2.[97] The minor peak at 688-692 eV belongs to CF_x from the dissociated CF_4.[98] The existence of the fluorocarbon is also confirmed from the C 1s spectra, as shown in Fig. 4.10(b). The large C 1s peak at 285 eV belongs to the C-C bond, which may come from the plasma process or from the air contaminant because the sample was exposed to air before ESCA analysis. The small peaks between 288 eV and 290 eV correspond to CF_2, CF and C-CF_x, respectively,[98] which are common on the CF_4 plasma exposed surface.[99] Figure 4.10(c) shows that the surface has a large CuCl or CuF peak at 931.5 eV,[100] and a smaller $CuCl_2$ or CuF_2 peak at 933 eV. Figure 4.10(d) shows a strong Cl $2p_{3/2}$ peak at 199.1 eV corresponding to CuCl.[100] Therefore, the addition of CF_4 in the Cl_2 plasma promotes the formation of CuF, CuF_2, and fluorocarbon.

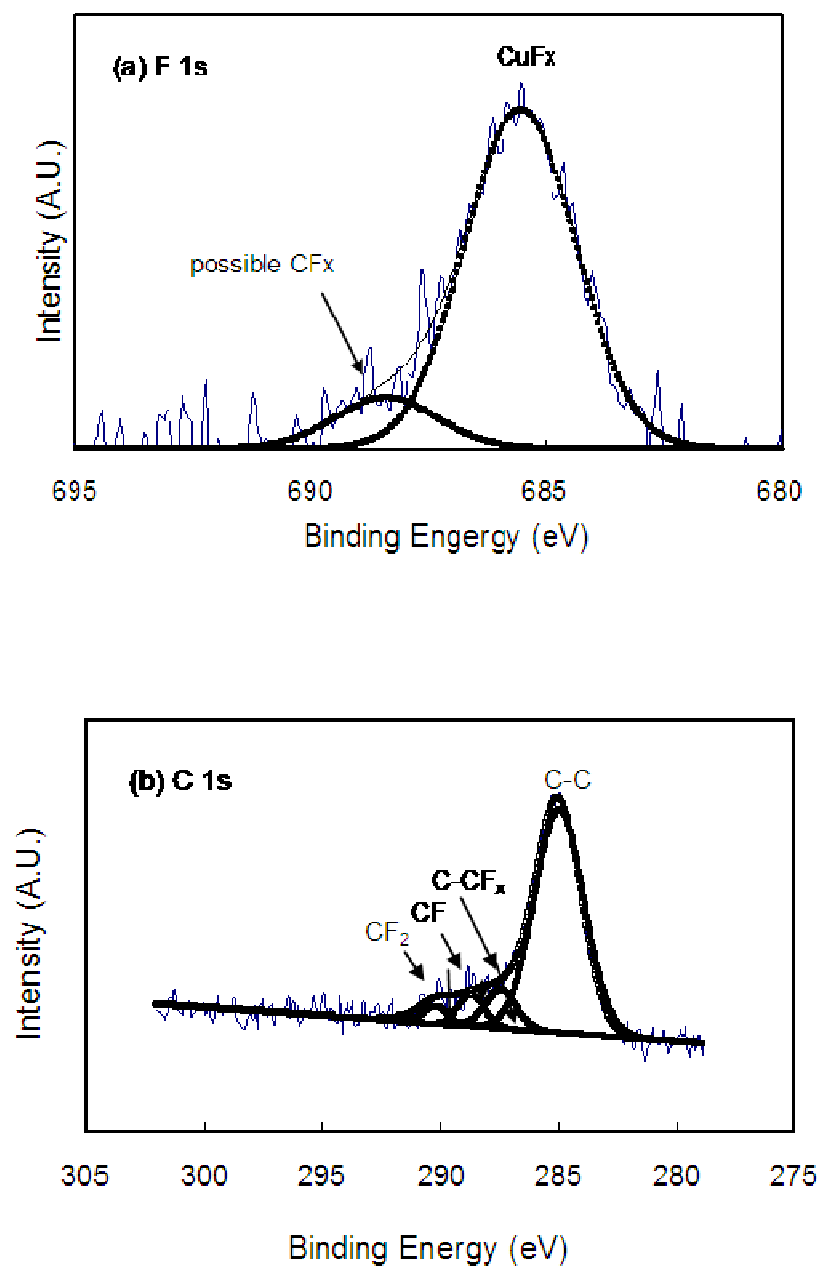

Figure 4.10 ESCA spectra of Cu surface after Cl_2/CF_4(20%) plasma at 600 W, 30 mTorr, and 20 sccm total feed stream. (a) F 1s, (b) C 1s, (c) Cu 2p, and (d) Cl 2p.

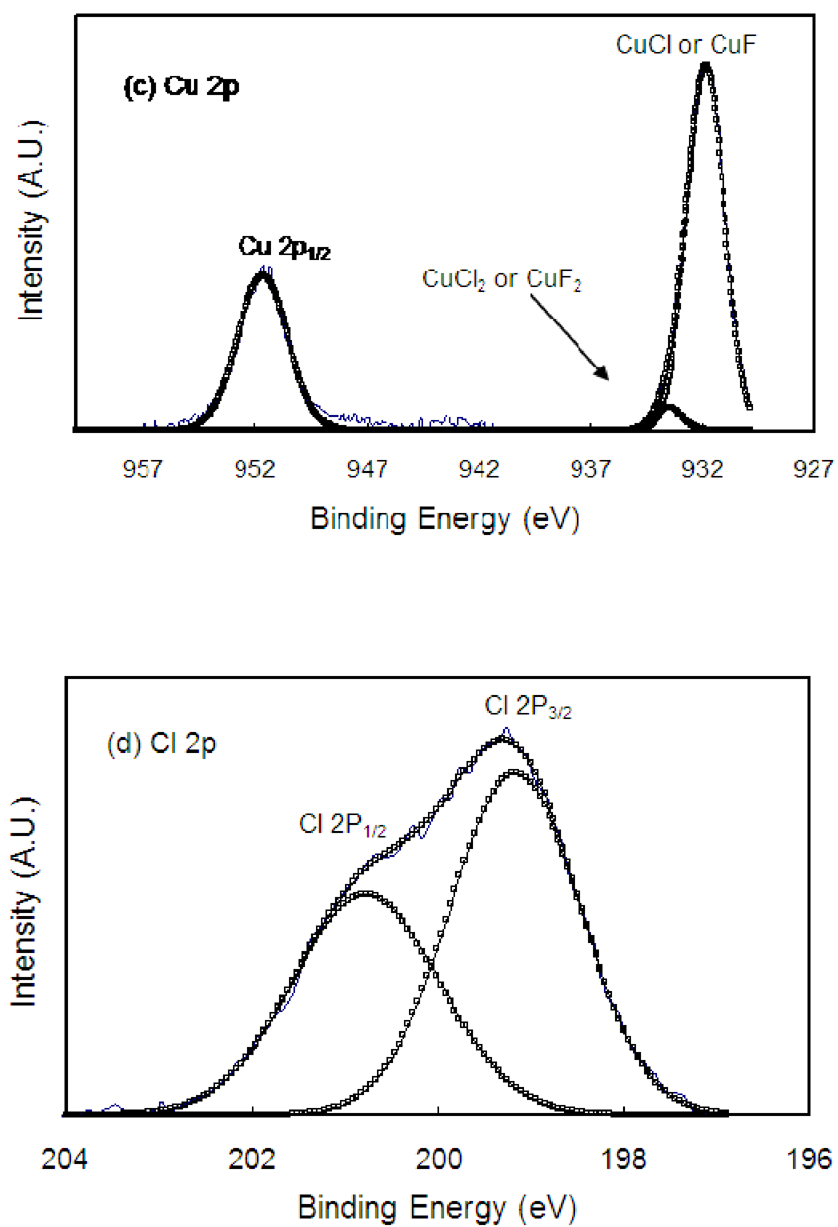

Figure 4.10 Continued.

Unlike the copper chloride, the copper fluoride is a passivation layer that blocks the diffusion of chemicals.[79] Separately, we observed that Cu was not consumed when exposed to pure CF_4 plasma. CF_4 was reported to lower the Cu film etch rate in the CCl_4 plasma due to the formation of copper fluoride.[13] The fluorocarbon layer can also lower the Cu consumption rate. Therefore, although the Cl radical can actively react with Cu, the reaction does not occur if Cl is not in direct contact with the Cu surface. Furthermore, it was reported that CHF_3 plasma formed a passivation layer on the aluminum surface, which decreased the sticking probability of Cl on the surface.[101] The similar phenomenon can be expected on the Cl_2/CF_4 plasma exposed Cu surface.

Figure 4.11 shows the thick Cu sidewall after the bottom thin Cu film was exposed to the Cl_2/CF_4 (20%) plasma followed by HCl solution dipping. In spite of the high Cl concentration in the plasma phase, the sidewall surface is smooth and contains no "mouse bites". Since it is difficult to measure the chemical bond structure on the sidewall, the surface composition of the plasma exposed bottom thin Cu surface could only be used as a reference to explain the sidewall surface morphology. The major difference between the sidewall and the horizontal surface is the ion bombardment energy. Since the ion bombardment direction is parallel to the sidewall, the ion bombardment effect on the sidewall is negligible. On the other hand, the fluorocarbon fragment from the plasma phase may deposit onto the sample surface. It is easier to form CF_x on the low ion bombarded surface than the high ion bombarded surface.[48] Therefore, the sidewall of the thick Cu layer may have a thicker CF_x layer than the horizontal surface has. The fluorocarbon residue and copper fluoride are also easier to form on the

sidewall to protect the Cu sidewall from Cl attack. To differentiate the passivation effect of CF_x from CuF_x, more studies are required.

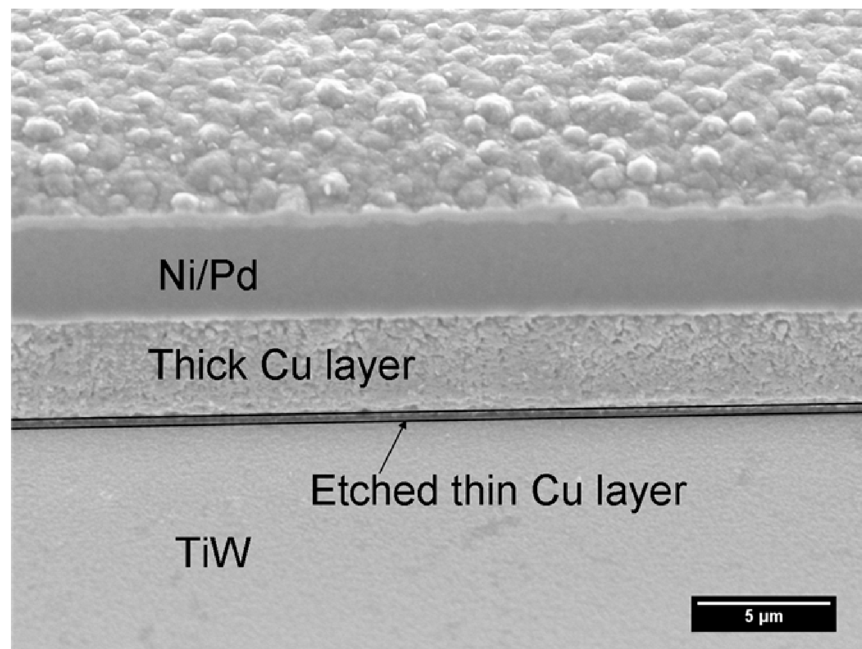

Figure 4.11 Cu sidewall after Cl_2/CF_4 (20%) plasma exposure and removal of $CuCl_x$. Sample was tilt 55° for SEM imaging.

4.3 Summary

The additive gas strongly affects the Cu consumption rate and the sidewall roughness in the Cl_2 plasma process. This is because the plasma phase chemistry, ion bombardment energy, and the surface structure all change with the additive gas. The addition of Ar enhanced the Cu consumption rate due to the strong ion bombardment and the increase of the Cl concentration; the latter also increased the sidewall roughness. The addition of N_2 increased the Cu consumption rate due to the increase of ion bombardment energy. However, due to the dilution of the Cl concentration, Cu sidewall did not show “mouse bites”. The addition of CF_4 can either increase or decrease the Cl concentration in the plasma phase depending on the CF_4 concentration. The ion bombardment energy increased monotonically with the CF_4 concentration. The Cl_2/CF_4 plasma exposed Cu sidewall was smooth and free of “mouse bites” due to the formation of a protection layer of CF_x, CuF_x, or both. In summary, the vertical direction Cu consumption process is related to the ion bombardment energy and the Cl concentration. The sidewall attack can be reduced or eliminated with the formation of a protective layer by adding N_2 or CF_4 into the Cl_2 plasma.

CHAPTER V

REACTIVE ION ETCHING OF TITANIUM TUNGSTEN THIN FILMS*

TiW films are usually used as the diffusion barrier for the Cu film because Cu has high diffusivity in silicon and dielectric layers. In this chapter, the plasma etching process of TiW was investigated using various Cl- and F-containing gas mixtures under different plasma conditions. The mechanism of the etching process has been investigated with regard to plasma phase chemistry and ion bombardment energy. In addition, since silicon nitride (SiN_x) is often used as a interlayer dielectric or passivation layer,[48] it is important to obtain a high etch selectivity between TiW and the underneath SiN_x. In this chapter, the plasma influence on the selectivity of these two films was also studied.

5.1 Experimental

The TiW film, e.g. 300 nm, was deposited by DC sputtering using a composite TiW (10 at.% Ti) target on a PECVD SiN_x film coated silicon (100) wafer. The crystal structure and composition of the TiW film were analyzed with X-ray diffraction (XRD) and Electron Spectroscopy for Chemical Analysis (ESCA), respectively. After the TiW film was patterned with a line-and-space mask using the AZ 5214 positive photoresist,

*Part of data reported in this chapter is reproduced from "Reactive Ion Etching of Titanium Tungsten Thin Films" by Guojun Liu and Yue Kuo, *Journal of the Electrochemical Society*, 154 (7), H653-H658 (2007), by permission of ECS - The Electrochemical Society.

the sample was transferred into the plasma etch reactor (Plasma Therm 700), which had a parallel-plate-electrode configuration and operated under the reactive ion etching (RIE) mode. Semiconductor grade CF_4, Cl_2, HCl, and O_2 gases were used as the feed gases. A wide range of process conditions were studied, e.g., gas mixtures of CF_4/Cl_2, CF_4/HCl, or CF_4/O_2, RF power between 300 W and 500 W at 13.56 MHz, and the chamber pressure between 70 mTorr and 160 mTorr. After plasma exposure, the photoresist layer was stripped off with acetone in an ultrasonic bath.

SiN_x was deposited at 250°C using the feed gases of SiH_4 40 sccm, NH_3 120 sccm, and N_2 720sccm. The RF power was 500 W. The nitride film obtained by this process was non-stoichiometric with the N/Si ratio of 0.85, and contained hydrogen in the forms of N-H or Si-H.[102] The plasma etching of the SiN_x was carried out with similar procedures as those of the TiW film.

The step height was measured with the Dektak 3 profilometer. The etch rate was calculated from the measured height and plasma exposure time. The chemical properties of the etched sample were examined with ESCA. The plasma phase chemistry was monitored with an optical emission spectroscope (OES). Intensity of Cl at 726 nm and F at 686 nm were monitored, and the Cl and F concentrations were calculated with the actinometry method using Ar at 750 nm as the reference.[83,17]

5.2 TiW film microstructure

Figure 5.1 shows the XRD pattern of the sputter deposited TiW film. Only metallic W peaks of (110) and (200) are observed while (100) and (111) peaks are absent,

indicating the film has a BCC structure.[67] No Ti peak is observed in this figure, which is similar to that of literature.[36] There are two possible reasons for the absence of Ti peak. First, the TiW film contains a high W concentration, e.g., 90 at. %, obtained from ESCA analysis. Since W has a higher atomic number than Ti (Z_w = 74 vs Z_{Ti} = 22), and the XRD intensity is directly proportional to the Z value, the Ti peak is probably too weak to show up.[35] Second, the small amount of Ti atoms probably occupy the W lattice position without forming a separate Ti phase. The pure Ti has a hexagonal close-packed (HCP) structure, which is not observed in the TiW film. According to Bragg's Law,[67]

$$d_{khl} = \frac{n\lambda}{2\sin\theta} \qquad (5.1)$$

where n=1 for first order diffraction, λ is the wavelength of the X-ray source, which is 1.5418Å. The W (110) peak in Fig. 1 corresponds to a lattice parameter of 3.187 Å, which is slightly larger than the W lattice parameter of 3.165 Å.[103] The W lattice parameter increasing may be due to the intermix of the Ti and W atoms during deposition.[104] Therefore, TiW can be taken as a solid solution where Ti dissolves in a W matrix.

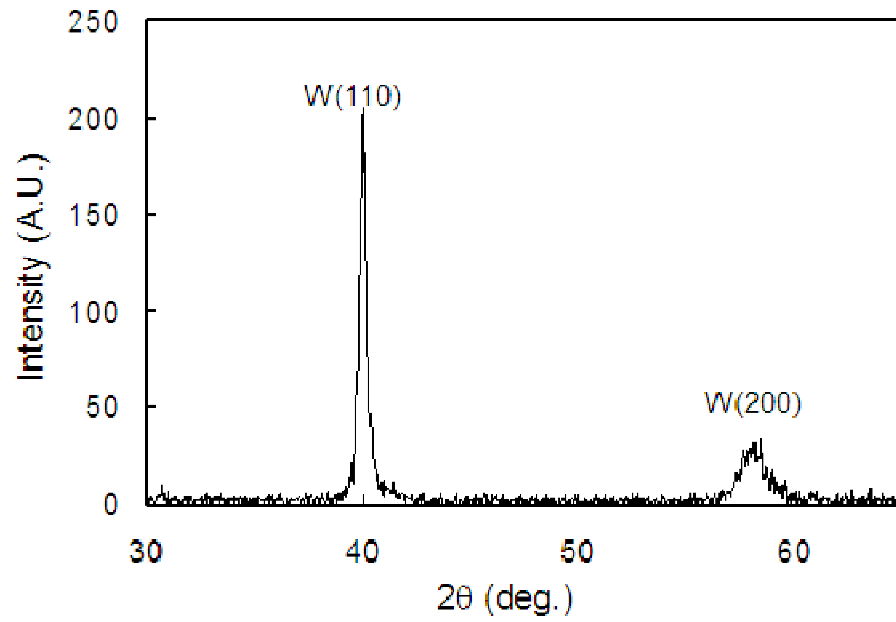

Figure 5.1 X-ray diffraction pattern of the sputter deposited TiW film.

5.3 TiW film etching characteristics

Feed gas effect on the TiW film etch rate

The etch rate of TiW film was studied by varying the feed gas composition of CF_4 with O_2, Cl_2, or HCl. Figure 5.2 shows the etch rate of TiW film as a function of the CF_4 concentration in the feed gas at 300 W plasma power, 100 mTorr pressure, and 20 sccm of total gas flow rate. For the CF_4/O_2 plasma, the etch rate curve peaked at about 70% CF_4. The introduction of O_2 promotes the dissociation of CF_4. The highest F radical concentration in the CF_4/O_2 mixture was at 70% CF_4.[8] In the CF_4/O_2 plasma, F and O radicals are two active species. Although O was reported to retard the etching reaction by blocking the active surface site during the etch of Si film,[105] it did not compete effectively with F radical in the reaction with Ti.[43] The etch rate of either Ti or W metal increased with the F concentration in the CF_4/O_2 plasma.[43,106] Fig. 5.2 shows the same trend. Therefore, in the CF_4/O_2 plasma, F is probably the dominant etchant for both Ti and W.

For the CF_4/Cl_2 plasma, the TiW etch rate increases first with the increase of the CF_4 concentration, e.g., from 400 Å/min for pure Cl_2 to 2500 Å/min for 50% Cl_2. The etch rate deceases with the further increase of the CF_4 concentration, e.g., to 500 Å/min for pure CF_4. Cl is an effective etchant for TiW although it is not as effective as F in the CF_4 plasma, i.e., etch rate of 400 Å/min in the Cl_2 plasma vs 500 Å/min in the CF_4 plasma.

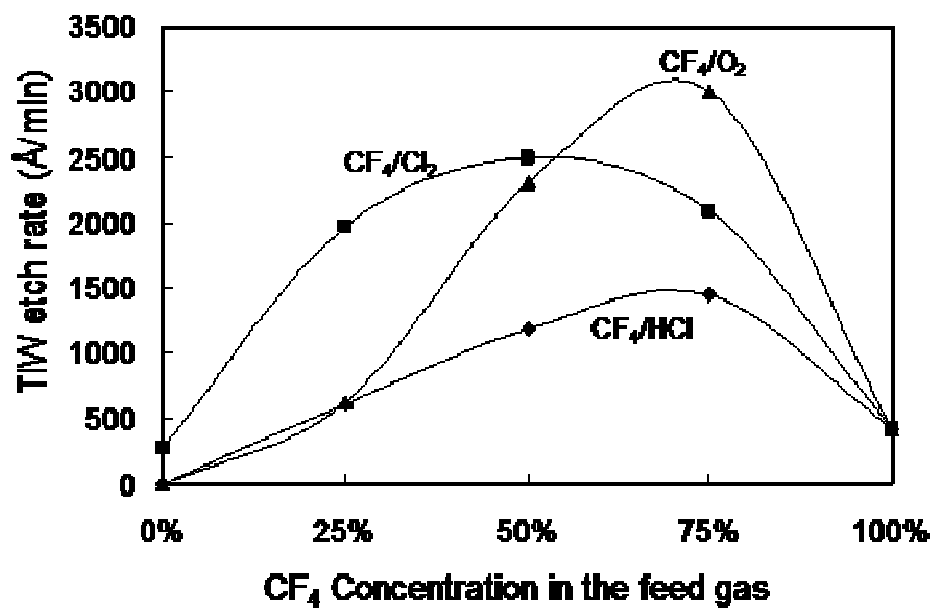

Figure 5.2 Effect of feed gas composition on etch rate of TiW film at 100 mTorr and 300 W (total flow rate 20 sccm)

Figure 5.3 shows the dependence of the Cl and F radical concentrations on the CF_4 gas concentration in the feed gas of CF_4/Cl_2. The F radical concentration increases with the increase of the CF_4 gas concentration. The plasma induced dissociation is proportional to gas pressure.[107] In this case, the chamber pressure and RF power were fixed. Therefore, the generation of F is probably proportional to the CF_4 concentration in the feed stream. On the other hand, the Cl radical concentration increases as the CF_4 concentration increases until the CF_4 concentration reaches about 50%, then it decreases as the CF_4 concentration further increases. The peak for Cl concentration in the CF_4/Cl_2 plasma may be due to the following reactions [95]

$$Cl_2 + e^- \rightarrow Cl + Cl \qquad (5.2)$$

$$Cl_2 + F \rightarrow ClF + Cl \qquad (5.3)$$

$$Cl_2 + CF_2 \rightarrow CClF_2 + Cl \qquad (5.4)$$

F and CF_2 are from the dissociation of CF_4. Equation (5.2) represents the electron impact dissociation of Cl_2. When CF_4 was added into the feed gas, the Cl concentration increased due to the enhanced generation of Cl by reactions (5.3) and (5.4). However, when CF_4 concentration was above 50%, the Cl concentration decreased due to the decrease of the supply of Cl_2. Fig. 5.3 shows that the sum of the Cl and F radical concentrations peaks at about 50% CF_4, which is consistent with the etch rate change in Fig. 5.2. Therefore, the etch process is contributed by both Cl and F radicals in stead of only individual F or Cl radical.

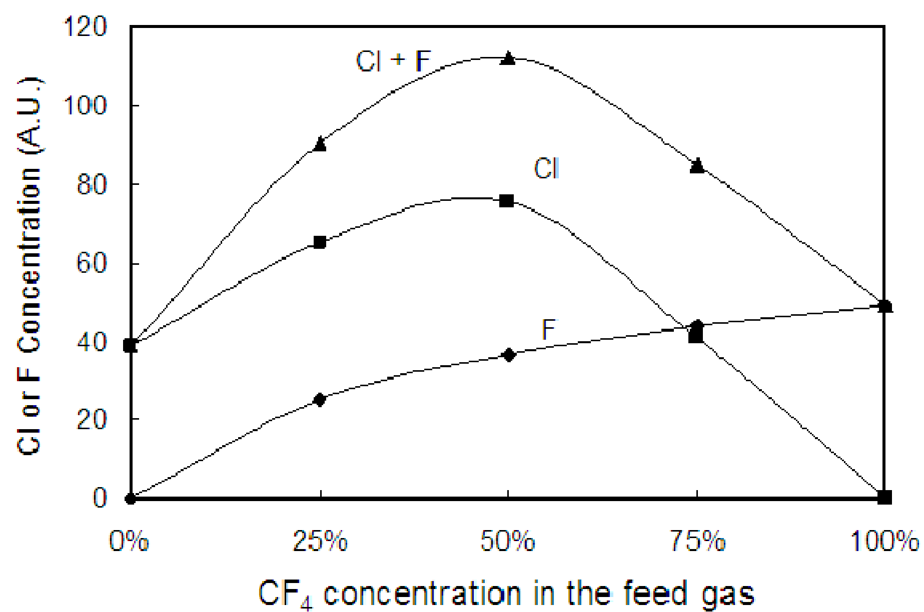

Figure 5.3 Effect of CF_4 concentration on Cl and F concentrations in the CF_4/Cl_2 plasma under the same conditions as in Fig. 5.2

For the CF_4/HCl plasma, the TiW etch rate is dependent on the CF_4 concentration, as shown in Fig. 5.2, which is similar to the CF_4/Cl_2 case. Cl and F radicals are the dominant etchants in CF_4/HCl plasma. However, HCl is not as effective as Cl_2 in providing the Cl radicals in the plasma phase, e.g., the etch rate in the pure HCl plasma is almost zero and that in the Cl_2 plasma is 400 Å/min. When hydrogen is added into CF_4 plasma, a Teflon-type of surface layer can be formed on the film surface, which may block the etch reaction.[48] In addition, H can getter F in the plasma phase, which lowers F concentration in the plasma.[108] Equations (5.2) and (5.3) reactions can be slowed down by this mechanism. Therefore, both the Cl and F radical concentrations in the CF_4/HCl plasma are lower than those in the CF_4/Cl_2 plasma at the same CF_4 concentration condition. As a result, the TiW film etch rate in the CF_4/HCl plasma is consistently lower than that in the CF_4/Cl_2 plasma under the similar conditions.

RF power effect on TiW etching

Figure 5.4 (a) shows the change of cathode self bias voltage ($-V_{dc}$), which is a reference of the ion bombardment energy, with the RF power. The feed gases were CF_4/Cl_2 mixtures with various CF_4 concentrations, but the total flow rate was fixed at 20 sccm. For the same feed gas composition, the $-V_{dc}$ increases as the RF power increases. Fig. 5.4 (a) also shows that for the same RF power, the $-V_{dc}$ increases as the CF_4 concentration increases. Previously, it was reported that the magnitude of $-V_{dc}$ is directly related to the molecular bond strength of the feed gas molecule.[96] Here, the change of -

V_{dc} is consistent with the bond strengths of CF_4 and Cl_2, i.e., 488 kJ/mol for C-F and 243 kJ/mol for Cl-Cl.[83]

Fig. 5.4 (b) shows the relationship between the TiW etch rate and $-V_{dc}$. For the same feed gas composition, the film etch rate increases with the increase of $-V_{dc}$, and the slope increases when the $-V_{dc}$ is increased, indicating ion bombardment energy is an important factor in this etching process. Ion bombardment enhances the surface reaction rate and the reaction product desorption rate. However, for the same $-V_{dc}$ the TiW etch rate does not change monotonically with the CF_4 concentration in the feed gas. In stead, the etch rate increases with the increase of the sum of the F and Cl concentrations, as shown in Fig. 5.3. In addition, the slope of the pure CF_4 curve is smaller than that of the Cl_2/CF_4 (50%) curve, especially at the high $-V_{dc}$ condition. Therefore, the slope appears to be related to the total F and Cl radical concentration in the plasma. The TiW etch rate is affected by both the ion bombardment energy and the effective etchant concentration in the plasma phase.

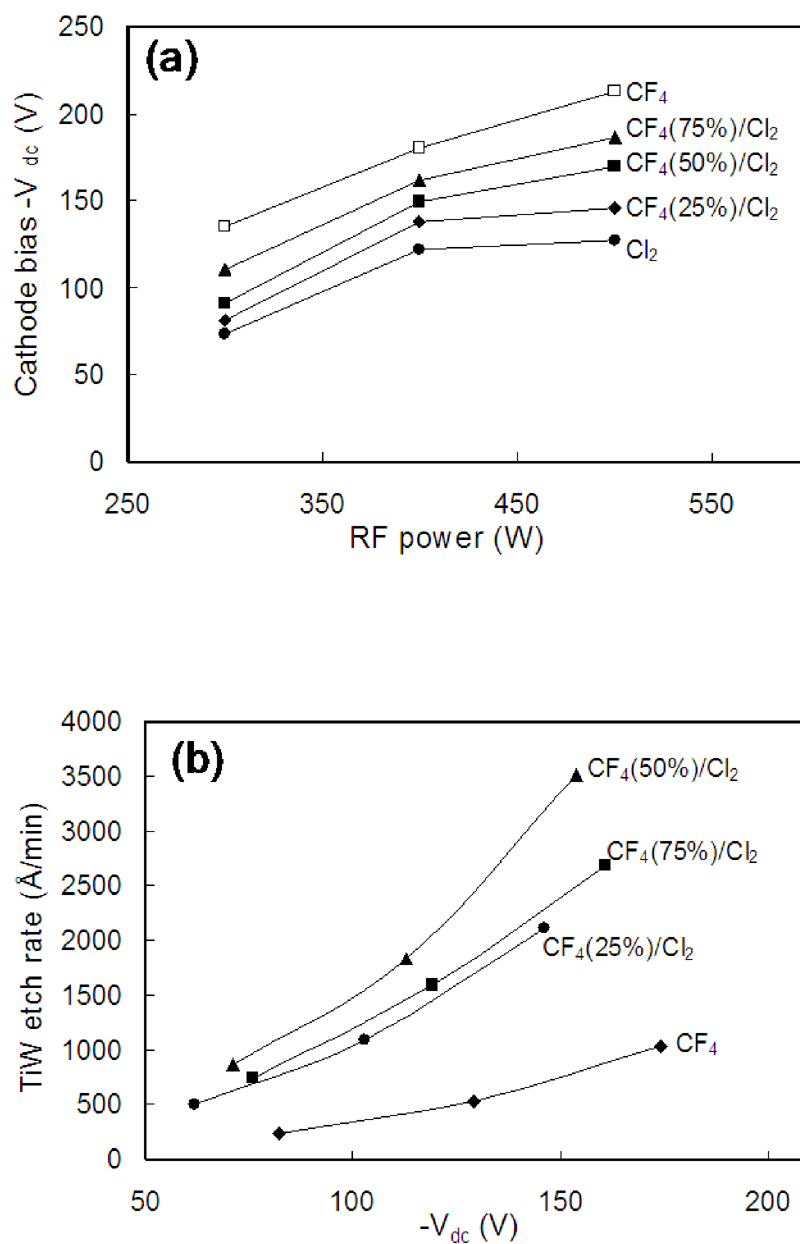

Figure 5.4 (a) Effect of RF power on cathode self-bias voltage in the CF_4/Cl_2 plasma at 100 mTorr pressure (total flow rate 20 sccm); (b) effect of cathode self-bias voltage on TiW film etch rate in the CF_4/Cl_2 plasma with the CF_4 concentration of 25 %, 50 %, 75 %, and 100% respectively.

Pressure effect on TiW etching

Figure 5.5 (a) shows the pressure effect on the TiW etch rate in the Cl_2/CF_4(50%) plasma at 300 W. TiW film etch rate increases with the increase of pressure from 70 to 100 mTorr, then decreases with the further increase of pressure. This pressure effect is similar to other plasma etching processes, such as Cl_2/BCl_3 etching of aluminum or SF_6/Ar etching of TiN.[109,110]

The pressure effect is due to the combination of the ion bombardment energy and the plasma phase chemistry. Fig. 5.5 (b) shows the changes of Cl and F radical concentrations as well as $-V_{dc}$ with the pressure. Both Cl and F concentrations increase with the increase of pressure. The Cl concentration is higher than the F concentration, probably because the Cl-Cl bond energy, i.e., 243 kJ/mol, is weaker than the C-F bond energy, i.e., 488 kJ/mol.[13] In the previous section, it was discussed that the TiW etch rate increased with the increase of the sum of Cl and F concentrations, which seems to be contradictory to the Fig. 5.5 (a) trend. However, Fig. 5.5 (b) also shows that the $-V_{dc}$ decreases with the increase of pressure, which is opposite to the change of the sum of Cl and F concentrations. When the pressure was below 100 mTorr, the ion bombardment energy was high enough to instantaneously remove the surface reaction product. Therefore, the TiW etch rate was determined by the supply of the Cl and F radicals from the plasma phase. When the pressure was above 100 mTorr, the etch rate was determined by the efficiency of the removal of the surface reaction product, i.e., the magnitude of $-V_{dc.}$

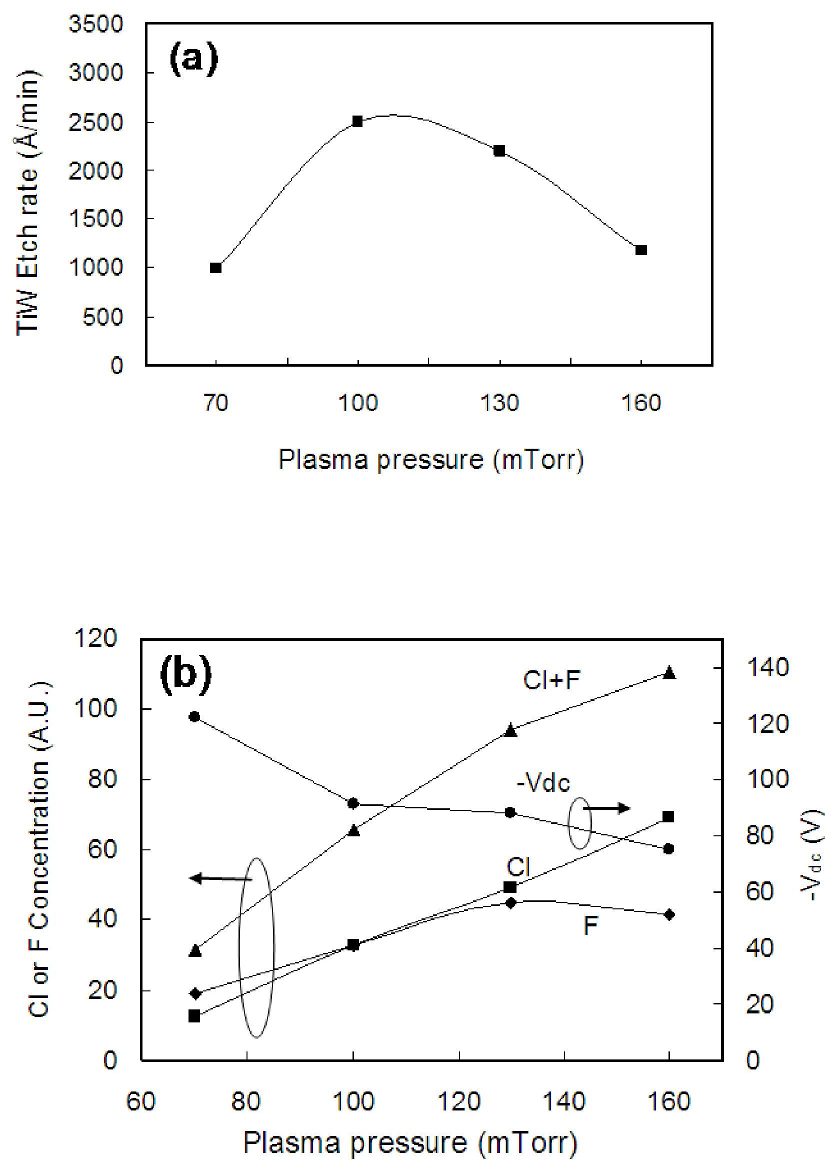

Figure 5.5 (a) Pressure effect on TiW etch rate in the CF_4(50%)/Cl_2 plasma at 300 W (total flow rate 20 sccm); (b) pressure effect on Cl and F concentrations and cathode self-bias voltage at the same plasma conditions as (a).

Surface chemical structure change with plasma condition

The plasma etched TiW surface was examined by ESCA to determine the possible etching mechanism. Figure 5.6 shows the spectra of (a) W 4f, (b) Ti 2p and (c) F 1s of TiW films before and after being exposed to various plasmas. W $4f_{7/2}$ and $4f_{5/2}$ peaks at binding energies of 31.2 and 33.4 eV are attributed to metallic W, and the doublet at 36.2 and 38.3 eV are attributed to WO_3. These W-O bonds are due to the surface oxidation when the samples were exposed to air before they were transferred into the ESCA chamber. After CF_4 plasma exposure, the WO_3 doublet shifted about 0.1eV to higher binding energies probably due to the formation of tungsten oxyfluoride.[111] F is more electronic negative than O. The weak doublet at 31.8 and 34.1 eV was assigned to W-F bonds by Turban.[39] However, it could also be attributed to tungsten suboxide (WO_x), because the same weak peaks were also detected on the TiW film without plasma exposure. After the CF_4 plasma exposure, the ratio of WO_3 to W is 1.53, which is lower than that before the plasma exposure, i.e., 1.73. The result is contradictory to the surface damage mechanism. Since the plasma etch process damages the film surface, which makes it easier to be oxidized, the CF_4 plasma exposed surface should have a higher WO_3 to W ratio. The above result is probably due to the blocking of the W surface from the residue generated from CF_4 plasma, such as F or CF_x, which will be shown later.

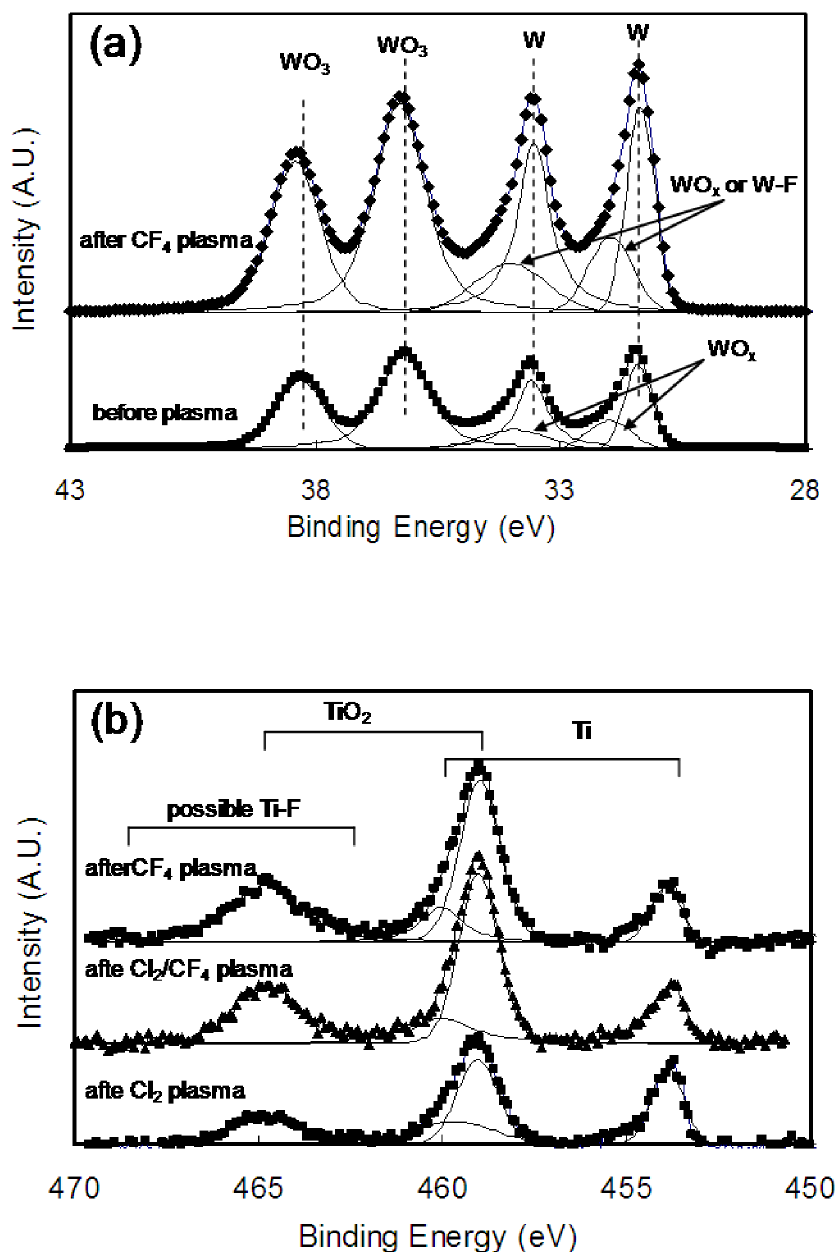

Figure 5.6 ESCA spectra of TiW films after being exposed to various plasmas at 100 mTorr, 300 W (total flow rate 20 sccm).
(a) W $4f_{7/2,\ 5/2}$ peaks before and after CF_4 plasma exposure.
(b) Ti $2p_{3/2,\ 1/2}$ peaks after CF_4, CF_4(50%)/Cl_2, and Cl_2 plasma exposure.
(c) Cl $2p_{3/2,1/2}$ peaks after CF_4(50%)/Cl_2 and Cl_2 plasma exposure.
(d) F 1s peaks after CF_4 and CF_4(50%)/Cl_2 plasma exposure.

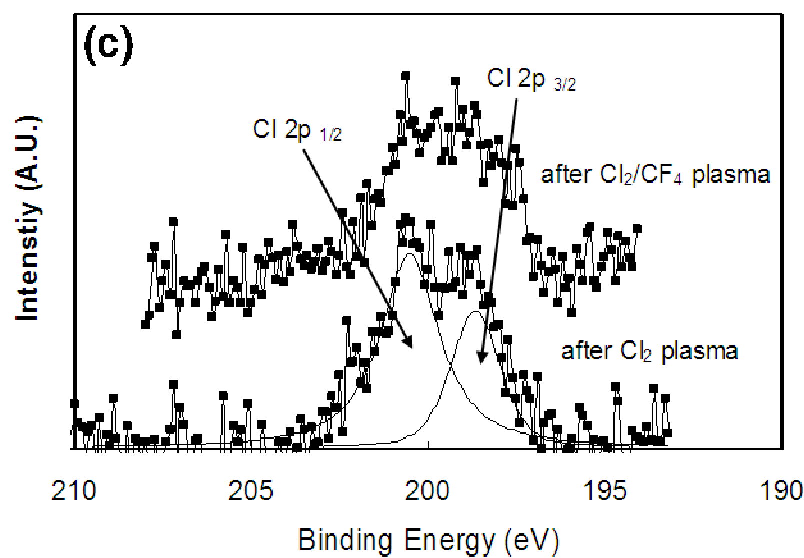

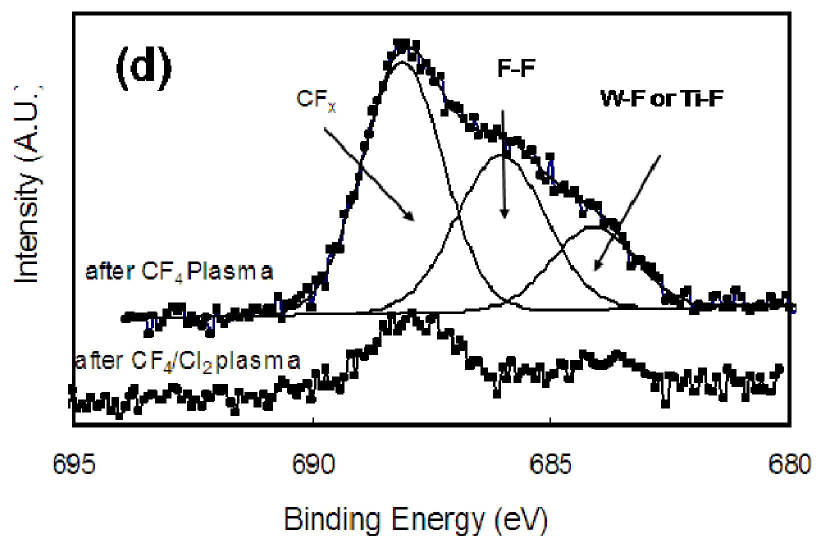

Figure 5.6 Continued.

Fig. 5.6 (b) shows Ti 2p core levels of the TiW film after being exposed to the CF_4, CF_4/Cl_2, and Cl_2 plasmas respectively. The Ti $2p_{3/2}$ and $2p_{1/2}$ at 453.8 and 460.1 eV are from metallic Ti, and the doublet at 459 and 464.5 eV are attributed to TiO_2 due to exposure to air. A very weak doublet at 462 and 468 eV was observed after CF_4 plasma exposure. Similar peaks were reported on the TiN surface after CF_4 etching and were assigned to TiF_3.[112] No apparent metal-Cl bond was observed on the TiW film after CF_4/Cl_2 or Cl_2 plasma exposure, although a trace amount, i.e., < 1.6 at.%, of Cl was detected on the both etched surfaces, as shown in Fig. 5.6 (c). Probably Cl or Cl_2 was physically adsorbed in the surface without forming strong chemical bonds since the surface chlorides were instantaneously removed during etch. Fig. 5.6 (c) also shows that the Cl peaks on the CF_4/Cl_2 plasma etched TiW surface are weaker than those on the Cl_2 plasma etched surface. Since the Cl concentration in the former plasma is higher than that in the latter plasma, as shown in Fig. 5.3, the surface Cl residue cannot be directly related to the plasma phase Cl concentration. It was learned from Fig. 5.4 (a) that the -V_{dc} in the CF_4/Cl_2 plasma was larger than that in the Cl_2 plasma. The higher removal rate of the surface Cl was due to the higher ion bombardment energy.

Fig. 5.6 (d) shows the F 1s spectra on the TiW surface after CF_4 and CF_4/Cl_2 plasmas exposures, respectively. The broad peak of F 1s has been deconvoluted into three peaks at 689.3 eV, 687.3 eV and 684.9 eV. The 684.9 eV peak belongs to the typical metal-fluorine bond. It may also belong to WF_4, which is located at 684.7eV in a previous report.[113] The 689.3 eV peak may be attributed to the CF_x compound, which is deposited from the CF_4 dissociated component. This is consistent with the surface C 1s

peaks located at around 288-290 eV. The 687.3 eV peak is likely attributed to the physically adsorbed F. In a previous report, the physically adsorbed F_2 (or F_2^-) showed the 687.6 eV F-F bond.[45] This physically adsorbed F peak was not observed on the CF_4/Cl_2 plasma etched TiW surface. Only very weak 684.9 and 689.3 eV peaks were detected. When the F concentration in the plasma phase decreased, the physically adsorbed F became less significant due to its preference to bind with metals.

Surface morphology after plasma etching

Figure 5.7 shows the TiW surface after the Cl_2 and CF_4/Cl_2 plasma exposure, respectively. The former shows a relatively smooth surface, while the latter shows a rougher surface with the “grass-like” appearance. The surface morphology was plasma chemistry dependent. ESCA results showed the W/Ti ratio on the Cl_2 plasma exposed surface was about 8.4, which was similar to that of the original TiW film, i.e. about 9. While the W/Ti ratio on the CF_4/Cl_2 plasma exposed surface was 5.6. The W/Ti ratio change was due to the preferential etch of W by the fluorine radicals. Since titanium fluoride is less volatile than tungsten fluoride, the latter would desorb quicker from the surface than the former, leading to the higher etch rate of W and lower W/Ti ratio. In the Cl_2 plasma, the TiW etch rate was low. No apparent etch preference of Ti or W was observed. Consequently, the surface after the Cl_2 plasma exposure is smooth. In the CF_4/Cl_2 plasma, the TiW etch rate was much faster than that in the pure Cl_2 plasma. The difference in the etch rate of Ti and W resulted in the “grass-like” appearance.

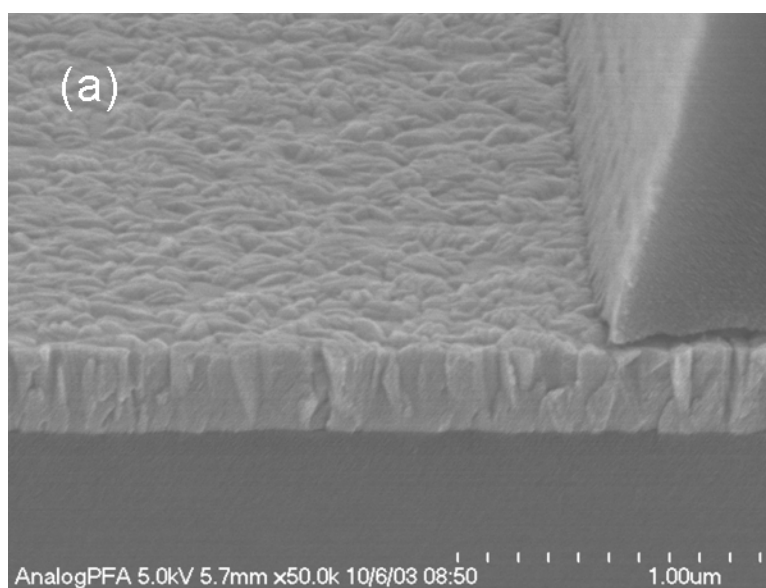

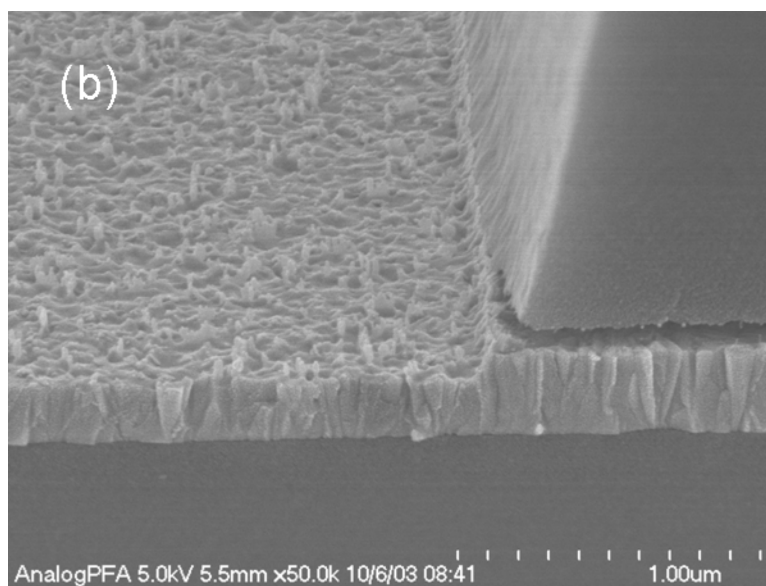

Figure 5.7 TiW surface after (a) Cl_2, (b) CF_4/Cl_2 plasma etch. Plasma condition: 300 W, 100 mTorr, 20 sccm, 20 seconds.

5.4 Selectivity of TiW to PECVD SiN_x

A high etch selectivity of TiW over the underneath dielectric layer, such as PECVD SiN_x is important for the interconnect process. Since the PECVD SiN_x can be etched with the CF_4 containing plasma,[48] it is important to study how to maximize the selectivity by adjusting the plasma process.

Figure 5.8 shows the etch rate of SiN_x as a function of the CF_4 concentration in CF_4/Cl_2 and CF_4/HCl mixtures under various plasma conditions. The etch rate of SiN_x increases with the increase of CF_4 concentration, which is due to the increase of the effective etchant, i.e., F in the plasma phase. The overall plasma etching reaction of PECVD nitride can be expressed as the followings,[48]

$$SiN_x + 4F \rightarrow SiF_4 + \frac{x}{2} N_2 \qquad (5.4)$$

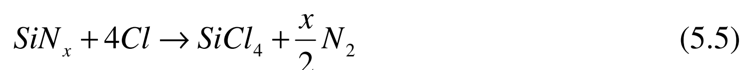

$$SiN_x + 4Cl \rightarrow SiCl_4 + \frac{x}{2} N_2 \qquad (5.5)$$

SiF_4 can desorb more easily from the SiN_x surface than $SiCl_4$ during the plasma exposure since the boiling point of SiF_4 is lower than that of $SiCl_4$, e.g, -86°C vs. 56°C.[75] In addition, the Si-F bond energy is 135 kcal/mole, which is larger than that of the Si-Cl bond energy, i.e., 90 kcal/mole.[75] Therefore, F-based plasma is more effective in etching SiN_x film than Cl-based plasma. The increase in etch rate becomes less significant when the CF_4 concentration is above 50%. At the high CF_4 concentration, the plasma phase F concentration is probably not the etch rate limiting factor. Other factors, such as the surface blockage from the CF_x component, may play an important role in the process.[48] This is supported by comparison of the etch rates in the CF_4/Cl_2 plasma at 300 W and

500 W. When the power increases, the ion bombardment energy increases; the film deposition rate is lowered and blockage effect is lessened. As a result, the SiN_x etch rate dramatically increased with power.

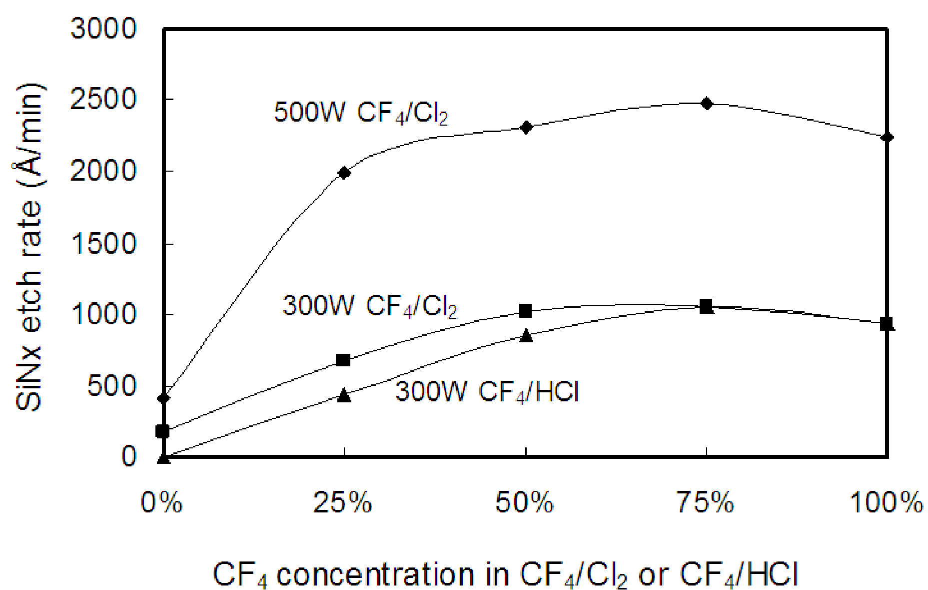

Figure 5.8 Effect of CF_4 concentration on SiN_x etch rate under CF_4/Cl_2 and CF_4/HCl plasmas at 100 mTorr (total flow rate 20 sccm)

Figure 5.9 shows the selectivity of TiW to SiN_x under various plasma conditions. For each curve, the selectivity decreases as the CF_4 concentration in the feed gas increases. The TiW and SiN_x etch rates behave differently with the CF_4 concentration, as shown in Fig. 5.2 and Fig. 5.8. The former peaks at around 50% CF_4; the latter monotonically increases with the CF_4 concentration. When the CF_4 concentration is higher than 50%, the TiW etch rate decreases and the SiN_x etch rate increases with the CF_4 concentration, resulting in the decrease of the selectivity. For pure CF_4 plasma, the selectivity is about 0.5, which means the SiN_x etch rate is larger than the TiW etch rate. By adjusting the CF_4 concentration in the feed gas, a selectivity of 2~3 is obtained, which is desirable for the practical application.

The etch selectivity of TiW to SiN_x decreased as the plasma power increased in the CF_4/Cl_2 plasmas. For both films, the etch rates are influenced by both the plasma phase chemistry, e.g., F and Cl radical concentrations, and the physical process, e.g., the ion bombardment energy. Since the ion bombardment process is less selective than the chemical reaction, the high power process gives a low selectivity. Further more, the etch selectivity of TiW to SiN_x in the CF_4/HCl plasma was lower than that in the CF_4/Cl_2 plasma. The SiN_x etch rate in the CF_4/HCl plasma was slightly lower than that in the CF_4/Cl_2 plasma under the same CF_4 concentration. In contrast, the TiW etch rate in the CF_4/HCl plasma was much lower than that in the CF_4/Cl_2 plasma, as shown in Fig. 5.2. Therefore, the plasma chemistry influences more on the TiW etch rate than on the SiN_x etch rate.

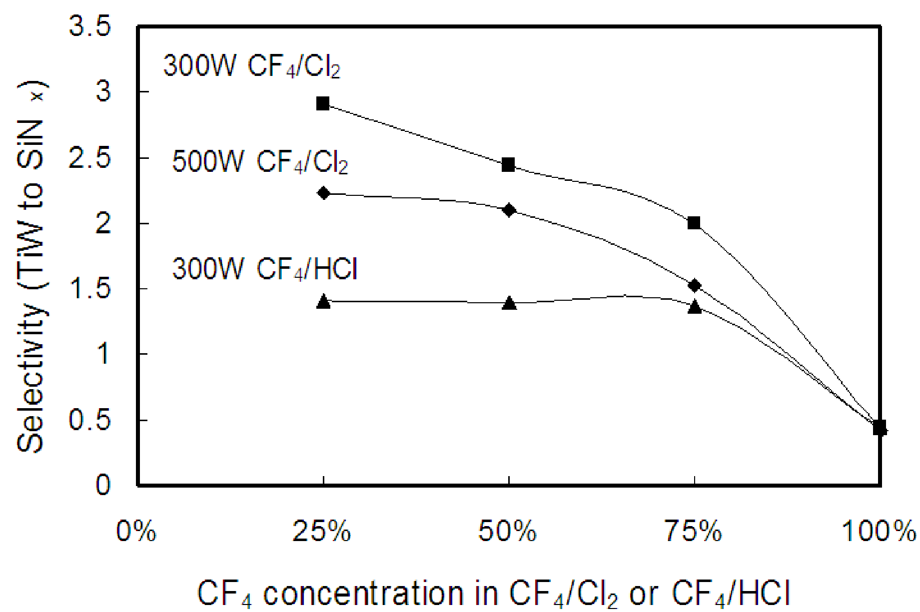

Figure 5.9 Effect CF_4 concentration on selectivity of TiW to SiN_x under the same plasma conditions as in Fig. 5.8.

5.5 Summary

Plasma etching of the TiW film has been investigated using the CF_4/O_2, CF_4/Cl_2, and CF_4/HCl feed gases under various gas compositions, RF powers, and plasma pressures. The etch rate behaviors are different in various plasmas. In the CF_4/O_2 plasmas, the F is the dominant etchant and the etch rate changes consistently with the F concentration. However, in the CF_4/Cl_2 and CF_4/HCl plasmas, the etch rate changes with the sum of Cl and F concentrations. The increase of RF power increases ion bombardment energy, which enhances the etch rate. The maximum TiW etch rate was achieved with the proper combination of plasma phase chemistry and ion bombardment energy at the medium pressure condition. The CF_4 plasma exposed TiW surface contains two types of F: physically adsorbed F, and chemically bonded F such as tungsten oxyfluoride or titanium fluoride. The Cl_2 plasma exposed TiW surface contains a trace amount of physically adsorbed Cl, however, metal-Cl bonds were not observed due to the instantaneous removal of the chloride during etch. The etch selectivity of TiW to SiN_x decreases with the increase of the CF_4 concentration and with the increase of the RF power. A etch ratio of TiW/SiN_x greater than 2 is readily obtained.

CHAPTER VI

ELECTROMIGRATION OF COPPER LINES PATTERNED BY CL_2 PLASMA-BASED ETCHING PROCESS

Electromigration (EM) is one of the most critical reliability issues in VLSI technology. EM performance not only depends on the materilal and structure, but also the patterning process. Most Cu EM tests were carried out with the lines patterned by the damascene process. The EM performance of Cu lines patterned with the unique plasma-based etching process was reported in this chapter.

6.1 Experimental

Single level test lines were patterned on two kinds of Cu films with multilayer structure, i.e., Cu(800 nm)/Ta(10 nm)/SiN_x/Si and Cu(240 nm)/TiW(20 nm)/SiO_2/Si, using a Cl_2 plasma-based etch process. Ta or TiW was used as the adhesion and diffusion barrier for Cu. The EM Cu line was 800 um long and 7 um wide resembling the NIST straight line with 4 Kelvin contact pads. The Cu film was patterned with the AZ5214 positive photoresist, followed by a Cl_2-based plasma etch process. The detailed Cu film etching process was described in Chapter I. After the Cl_2 plasma exposure, the Cu at the unprotected area was converted into $CuCl_x$, which was dissolved by a dilute HCl solution. Subsequently, the Ta or TiW barrier layer was etched by another RIE process using CF_4 plasma which did not attack the Cu line.[77] The photoresist layer was stripped off with acetone in an ultrasonic bath. Finally, a silicon nitride layer was

deposited by a plasma enhanced chemical vapor deposition (PECVD) process at 300°C to cover the patterned Cu lines, which prevented Cu from oxidation during the EM tests. The detailed PECVD SiN_x deposition condition is described in the reference.[114] The silicon nitride layer at the probe contact pad area was etched off with a dilute buffered oxide etch (BOE) solution, i.e., BOE: water = 1:6.

EM tests were carried out on a probe station (Signatone s-1160), which contains a hot chuck with the temperature control 200°C. The detailed experimental setup is described in Chapter II. The Cu lines after EM was pictured with scanning electron microscopy (SEM) and energy dispersive spectroscopy (EDX). Planar views were obtained after the passivation SiN_x cap layer was removed by a dilute HF solution.

Two tyes of EM tests were carried out: Cu lines with and without mechanical bending. For the former, the test sample was directly mounted onto the hot chuck. For the latter, the sample patterned on the thick (800 nm) Cu film was cut into a 1.2 x 2 cm^2 plate, which was placed on the three-point bending aluminum (Al) holder on the hot chuck. As shown in Figure 6.1(a), two tungsten wires (60 um in diameter) were placed underneath the 700 um thick sample plate, perpendicular to the Cu line direction. Two screws were used to clamp the center line of the sample plate. Fig. 6.1(b) shows the bended sample plate. The detail view of Cu line for EM tests is shown in Fig. 6.1(c). The damge of the Cu test lines was compared to the dummy lines after EM tests.Knowing the positions of the wires and the screws, and the diameter of the tungsten wire, the stress caused by the mechanical bending can roughly estimated through the curvature of the

bened film.[115] It was bout 85MPa in this setup, far more than the internal stress without mechanical bending.[32]

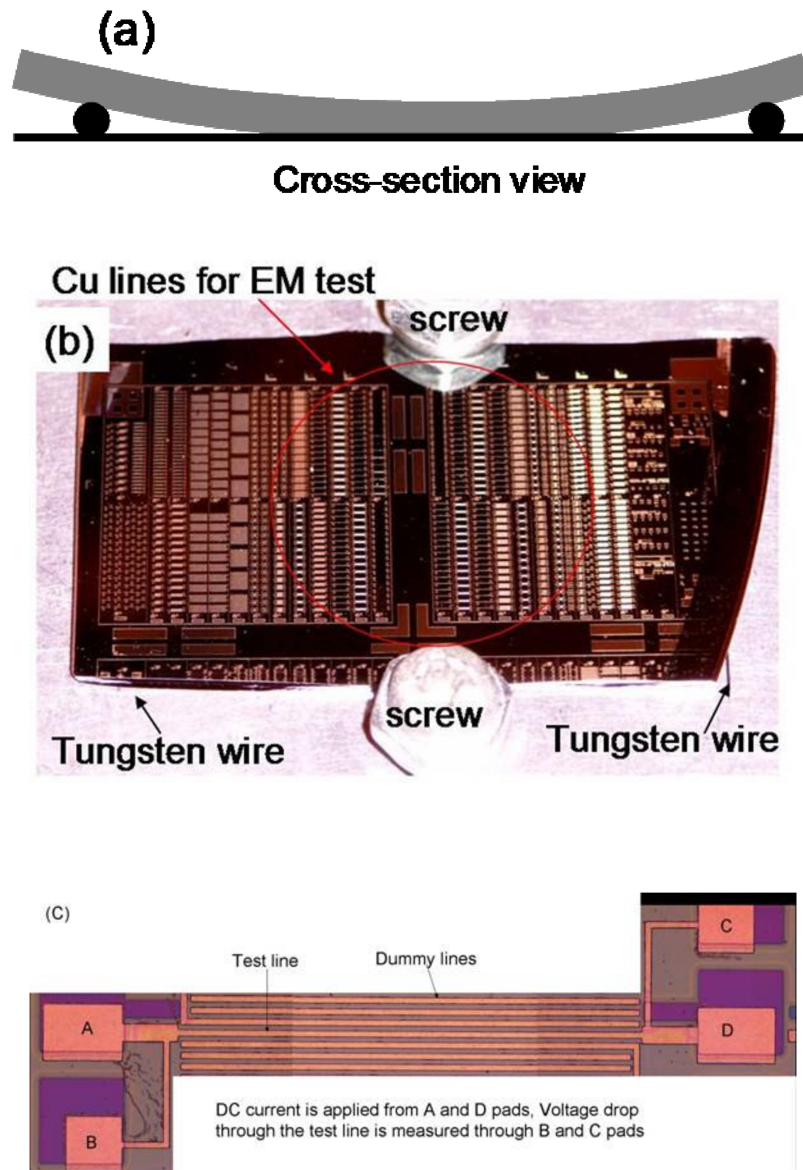

Figure 6.1 (a) Illustration of the three-point bending setup for EM test; (b) optical image of the bended sample plate; (c) optical image of Cu line for EM test.

6.2 Isothermal EM algorithm

The isothermal EM test was executed using a feedback control loop that adjusted the current to the Cu line so that the effective temperature of the test line was kept within a narrow error band of the test temperature. The algorithm of the test is similar to that of JESD61.[116] Each EM test includes 3 phases, i.e., initialization, temperature ramping and convergence, and stress. Figure 6.2 shows the flow chart of the isothermal EM test procedure. The temperature coefficient of resistance (TCR) was measured prior to the EM test following the guidelines of JESD33-B.[117] The Cu line resistance was measured at the chuck temperature of 20, 50, 80, and 110°C, respectively. The current was kept small enough, i.e., 2 mA, to minimize the Joule heating during the measurement. The TCR value was calculated with the following equation.

$$TCR(T) = \frac{1}{R(T)} \times \frac{\Delta R}{\Delta T} \tag{6.1}$$

where $R(T)$ is the resistance of the Cu line at the temperature of T.

In the temperature ramp phase, the effective temperature of the Cu line was gradually increased toward the target temperature, T_{test}, by gradually adjusting the applied current. At any current, the effective temperature was calculated by the following equation:

$$T_{cal} = T_{chuck} + \frac{R(T_{cal}) - R_{chuck}}{R_{chuck} \times TCR_{chuck}} \tag{6.2}$$

where $R(T_{cal})$ is the measured line resistance.

When the effective temperature was above 230°C, the departure of the calculated temperature from the above linearity was not negligible. Therefore, the following correction factor was applied.[118]

$$F_{corr}(T_{cal}) = 1.0167 - 8.39752 \times 10^{-5} \bullet T_{cal} - 3.74768 \bullet T_{cal}^{2} \quad (6.3)$$

$$T_{real} = F_{corr}(T_{cal}) \bullet T_{cal} \quad (6.4)$$

During the temperature ramp phase, the power dissipation (P) in the Cu line was also calculated. The thermal resistance (r_{th}) of the Cu line was obtained using the linear relationship of T vs. P.

$$T = t_0 + r_{th} \bullet P \quad (6.5)$$

where t_0 is the empirical temperature constant. When the effective temperature was close to the target temperature, i.e., within 90% of T_{test}, the test line temperature could not be estimated with equations (6.2), (6.3) and (6.4) due to the possible EM damage. Then the temperature was estimated using r_{th} by the following equation.

$$T = T_{ref} + r_{th}(P - P_{ref}) \quad (6.6)$$

where T_{ref} and P_{ref} are the temperature and the power dissipation at the end of ramp phase. Meanwhile, the current increase rate was reduced to avoid the temperature overshoot. Once the effective temperature reached T_{test}, the test reached the stress phase where the input power was kept constant assuming the constant heat dissipation.[116] The value of the current was adjusted slightly depending on the measured line resistance.

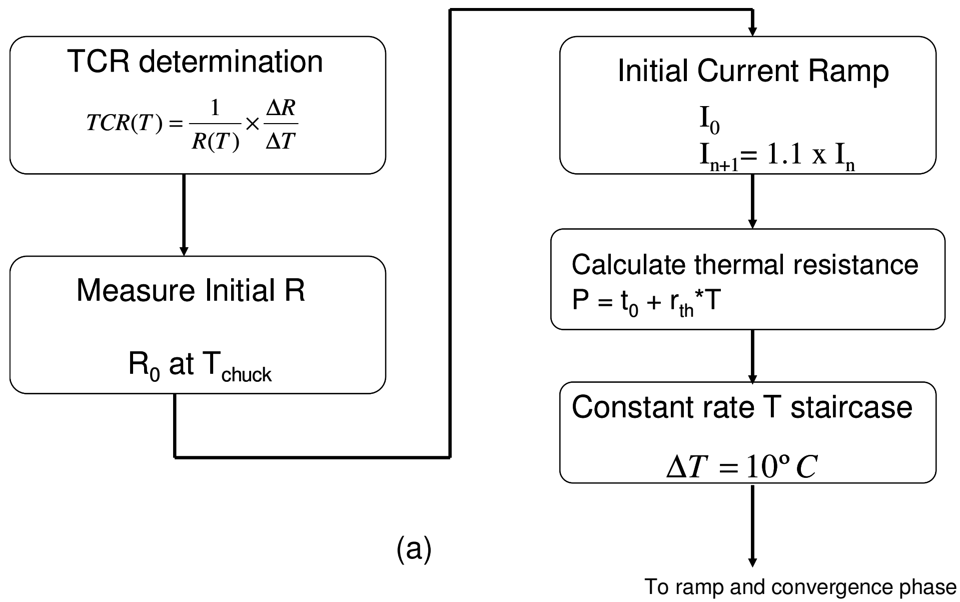

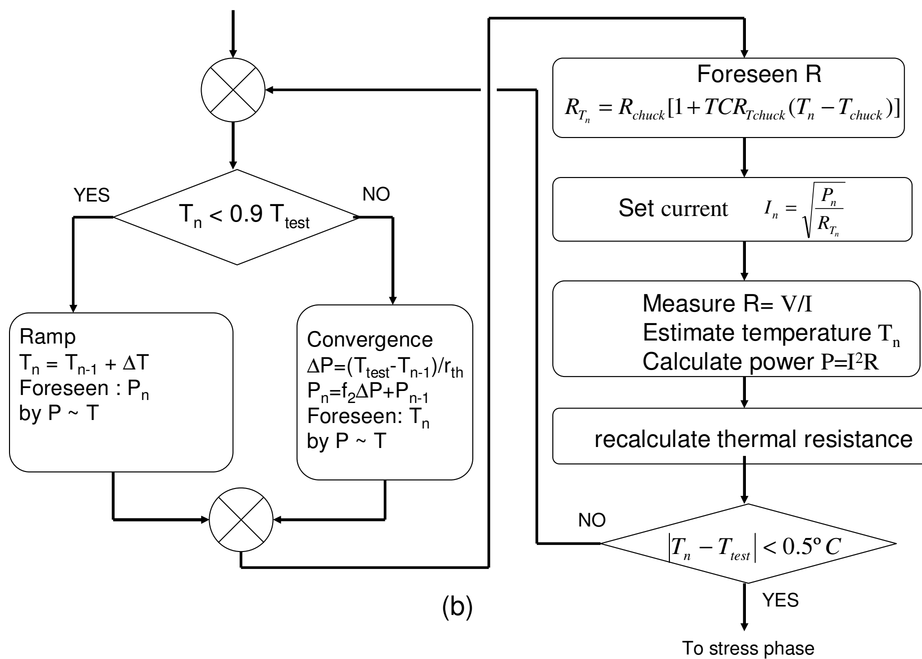

Figure 6.2 Flow chart of isothermal EM algorithm. (a) initialization phase; (b) temperature ramp and convergence phase; (c) constant power stress phase.

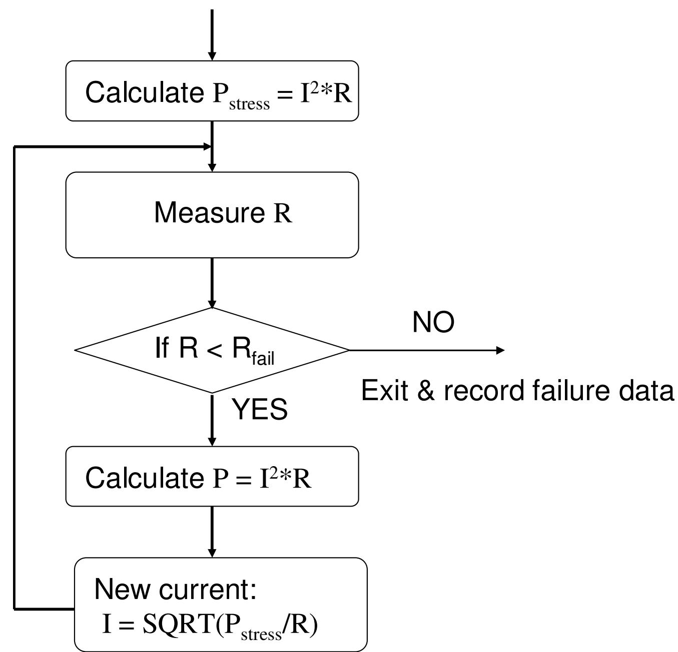

Figure 6.2 Continued.

Figure 6.3(a) shows a typical example of the resistance change with time during the test. In zone I, the current increased by a fixed factor, i.e., $I_{n+1}=1.1*I_n$, after the chosen initial current. This phase ended when the initial thermal resistance was obtained. In zone II, the temperature increment, e.g., $\Delta T = 10°C$, was fixed. The Cu line resistance increased gradually due to the temperature increase caused by the Joule heating. Zone III is the stress phase where the resistance increased slightly but almost linearly with time. This resistance behavior is consistent with the growth of many voids located along the line length. When the line was near the breaking point, its resistance increased rapidly. The test was stopped when the failure criterion was met, i.e., 5% increase of the relative resistance.

Fig. 6.3(b) shows a typical example of the Cu line temperature change with time during the test. The temperature increased gradually by the increase of Joule heating. Thermal resistance, r_{th}, obtained initially in zone I and recalculated iteratively in zone II, was used to estimate the effective temperature when the temperature was close to the T_{test}. The convergence algorithm brought the temperature of the Cu line smoothly to the T_{test} without overshooting. The effective temperature remained constant during the stress phase, i.e., zone III.

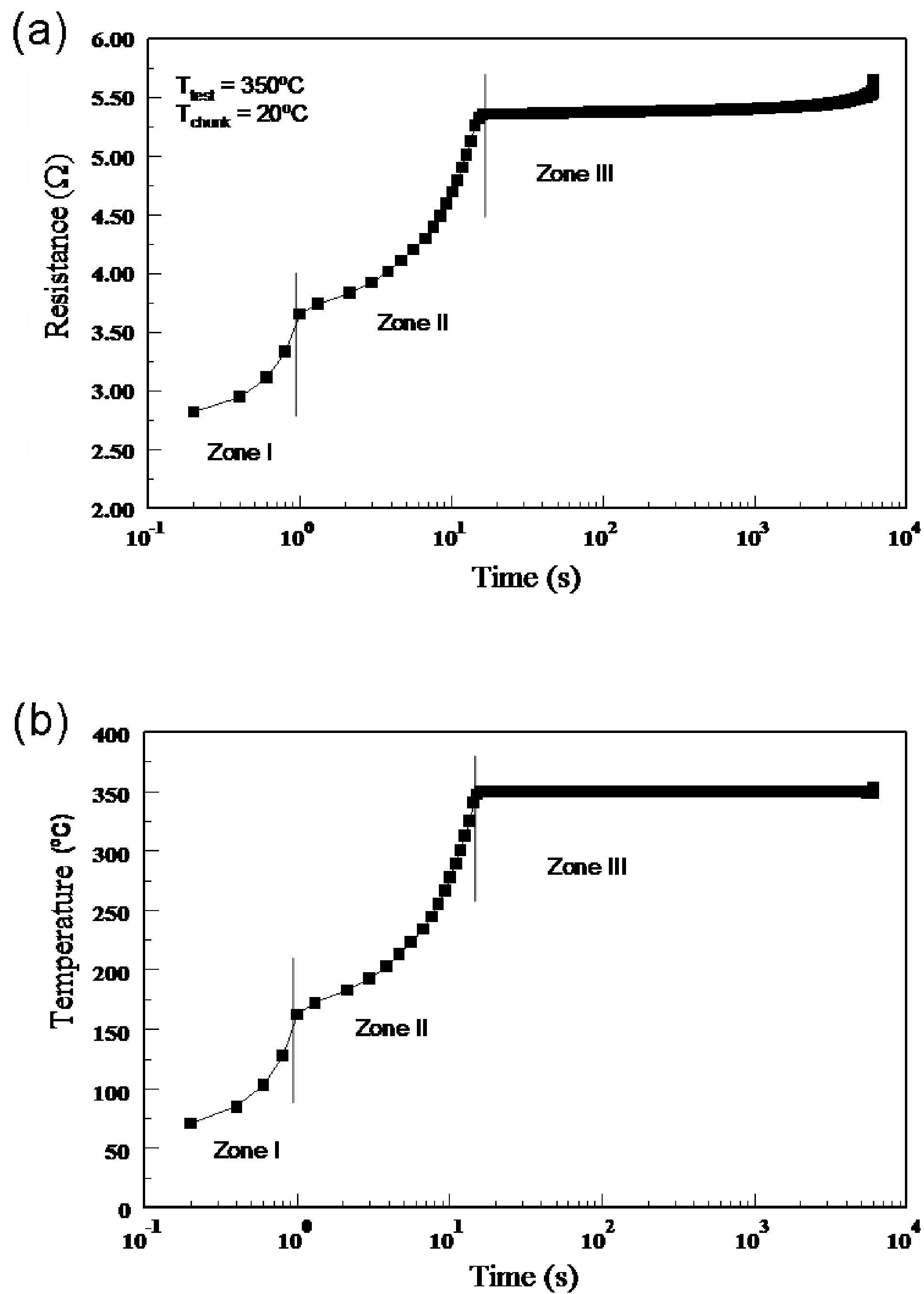

Figure 6.3 Typical (a) resistance and (b) line temperature changes during isothermal EM test.

6.3 Statistical performance of EM

Figure 6.4 shows the initial stress current I_0 vs. the initial resistance R_{chuck} for the EM tests at 320, 350 and 380°C, with the chuck temperature of 20°C. I_0 was the current value when the EM test just turned into the stress phase. The initial stress current is higher for the higher test temperature because more power is required to heat up the test line. For the same test temperature, the initial stress current is higher for the structure with lower resistance. Similar linear fit was reported and was attributed to the derivative of I/R at a narrow range of original resistance.[119] The linear fit suggested that the Cu lines were ready for the EM test, i.e., among those lines, no serious fabrication variation would affect the EM performance.

The activation energy (E_a) and the current density acceleration factor (n) are usually expressed by the Black equation.[52]

$$MTTF = \frac{A}{J^n}\exp(\frac{E_a}{kT}) \qquad (6.7)$$

where MTTF, J, and k are median time to failure, current density and Boltzmann's constant, respectively. A is the normalization time, which depends on the geometry and microstructure of the test line. Equation (6.7) can be transformed to the following.

$$\ln(MTTF) = \ln(A) - n\ln(J) + E_a / kT \qquad (6.8)$$

The value of n can be obtained by the linear regression of ln(MTTF) vs. ln(J) at the same T. The value of E_a can be obtained by the linear regression of [ln(MTTF)+nln(J)] vs. 1/kT once the value of n is known.

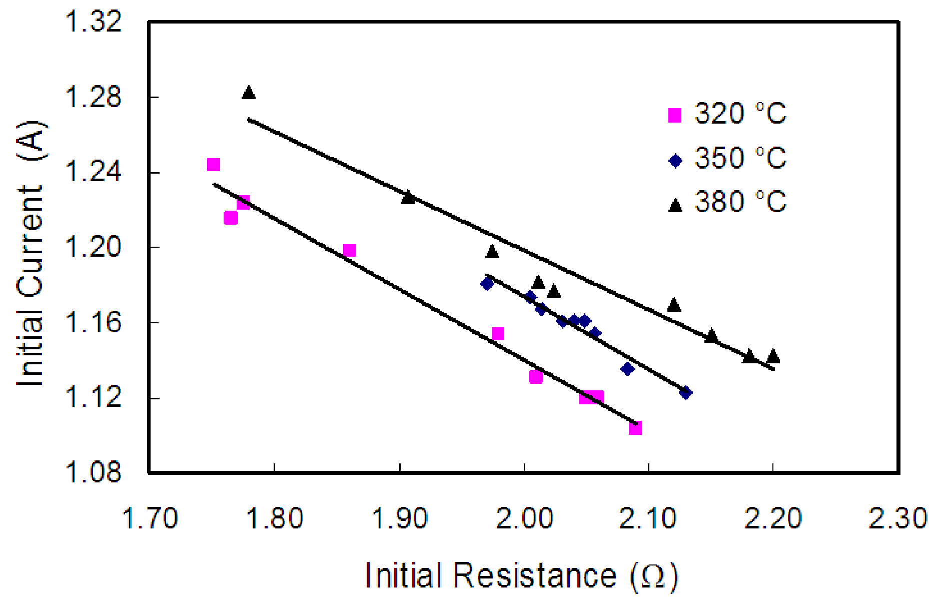

Figure 6.4 Correlation between initial current of stress phase at 320, 350, and 380°C and initial resistance.

Since the temperature and the current density were coupled in the isothermal EM test. In order to decouple T and J, the EM tests were conducted at the same test temperature of 350ºC but different chuck temperatures. In such cases, the current density varied for the same T_{test}. Figure 6.5 shows the cumulative failure distribution of 800 nm thick Cu lines at 350ºC with the chuck temperature of 20ºC, 46ºC, and 74ºC, respectively. The inset shows the linear regression of ln(MTTF) vs. ln(J). The n value of 2.7 was obtained. It is generally considered that the n value should lie between 1 and 2. For void-growth limited failure, the n value was reported to be close to 1 while for nucleation limited failure it should be close to 2.[2] For an n value greater than 2, there may exit a thermal gradient during the EM test. For the Cu lines in this test, the SEM observations showed that the voids were randomly distributed along the length. However, during the void growth, the temperature increases locally in the vicinity of the void. From the Black equation, the underestimated temperature leads to an overestimation of the n value. Similarly, the n value increased with the current density due to the increase of Joule heating in the EM test on the packaged chips.[120] Therefore, the isothermal EM test here resulted in a larger n value than the conventional moderate EM test.[58]

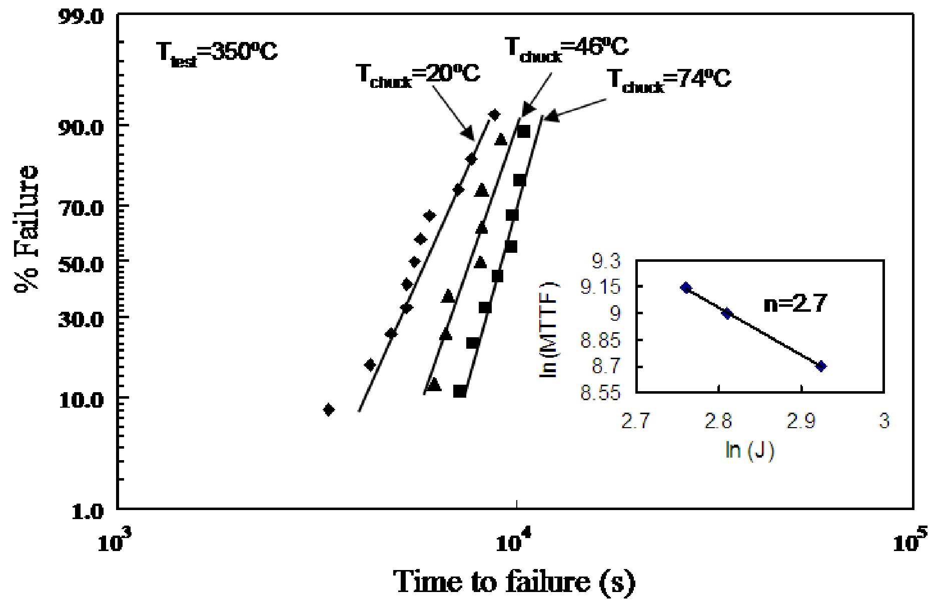

Figure 6.5 Cumulative failure distribution of thick Cu line at 350ºC with different chuck temperatures. The inset is the linear regression of ln (MTTF) vs. ln (J).

Figure 6.6 shows the cumulative failure distribution of the 800 nm thick Cu lines at the test temperatures of 320, 350 and 380°C. The times to failure (TTF) follow a log-normal distribution with the standard deviation σ between 0.19 and 0.30. Although these σ values are larger than those obtained from two-level test structure,[121] they are comparable to the value obtained from the single level damascene test structure.[122] For the two-level structures, failure occurs in or adjacent to the vias because they are the weakest regions. The low value of σ in the two-level interconnects were due to this well defined failure model.[122] For the single level structure, failure is more sensitive to Cu film microstructure and interface.[123] The value of σ became large when more than one failure mechanisms existed in the test structure.[124]

The inset of Fig. 6.6 shows the linear regression of [ln(MTTF) + n ln(J)] vs. 1/kT using $n = 2.7$ obtained from Fig. 6.5. The E_a value of 0.6 eV was obtained. There are four possible diffusion paths in the Cu structure: lattice, grain boundary, Cu/Ta interface, and Cu/SiN_x interface. As discussed in Chapter I, the lattice and the grain boundary diffusion generally show a large E_a value, i.e., larger than 1.2 eV. The Cu-barrier metal interface diffusion shows a larger E_a value than that of the Cu-dielectric interface diffusion because the former has a stronger adhesion force than the latter. The strength of adhesion affects the void nucleation and growth rate induced by EM. The PECVD SiN_x cap layer usually adheres weakly to the Cu layer.[125] In addition, the large difference of the thermal expansion coefficient (CTE) between Cu and the dielectric film weakens the interface in the EM test at high temperature.[126] An E_a value of 0.65 eV was reported for Cu line with PECVD SiN_x cap layer.[125] The E_a value of 0.6 eV in this study

indicates that the Cu-SiN_x cap layer interfacial diffusion may be the primary transport mechanism. Considering the extrapolation to the regular use condition, equation (1.3) is employed. At operation conditions such as the temperature of 105°C and the current density of 3 MA/cm^2, the MTTF at the operation condition will be more than 30 years, which exceeds the requirements for most microelectronic application.

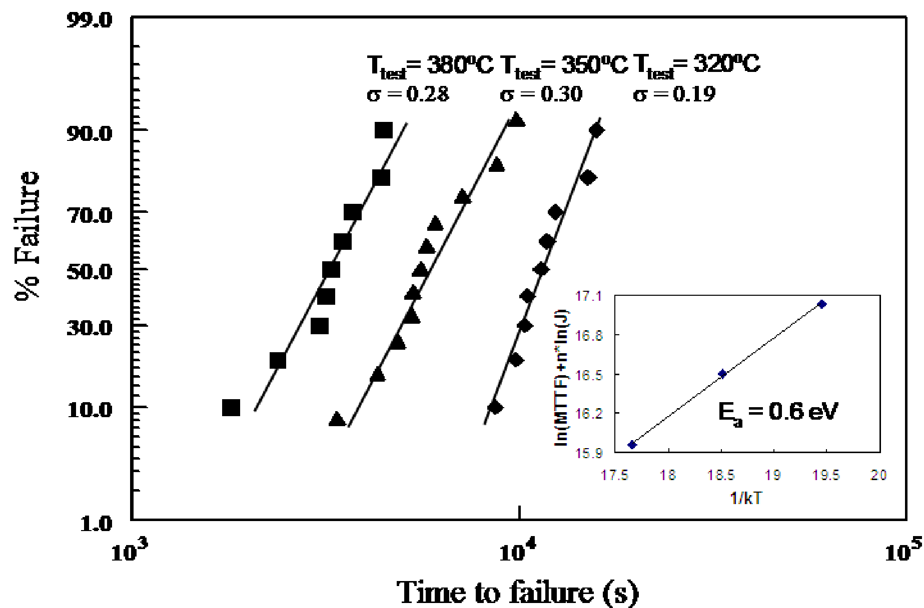

Figure 6.6 Cumulative failure distribution of 800 nm thick Cu lines at various test temperatures. The inset is the linear regression of [ln(MTTF) + n*ln(J)] vs. 1/kT, using n =2.7.

Figure 6.7 shows the cumulative failure distribution of 240nm thick Cu lines at the test temperatures of 150, 175, and 200°C. The E_a value of 0.49 eV was obtained. The thin sputtered Cu film showed a much shorter life time than that of the thick electroplated Cu film. Since the EM failure time is not sensitive to the Cu film microstructure,[127] the difference in the Cu films' microstructure was not the main factor to the lifetime difference. On the other hand, if the interfacial diffusion is the primary mechanism for the EM failure, its effect on EM is more significant for the thinner Cu film than for the thicker Cu film because the interface area fraction of the former is higher than that of the latter. It was reported that the narrow Cu damascene lines showed shorter lifetimes due to the interface diffusion mechanism.[123] Moreover, the thicker film need a longer time to develop the voids that go through the whole layer thickness than the thinner film need, which results in the former's longer lifetime. The diffusion path cannot be solely determined by the value of E_a. If more than one diffusion mechanisms exist in the EM process, the E_a calculated from the lifetime test should be considered as an apparent value that can not be associated exclusively to any single diffusion path.

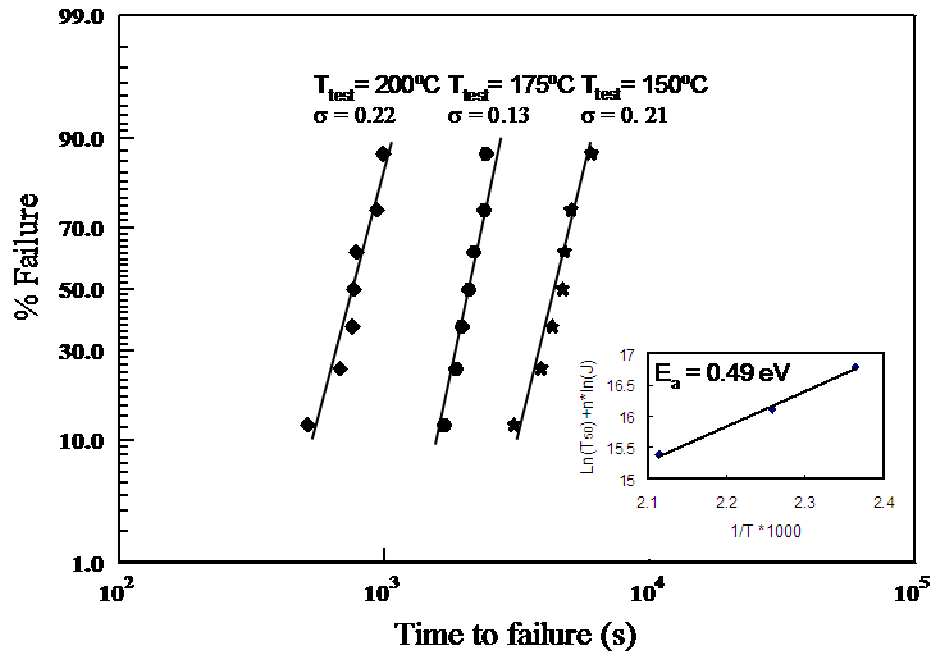

Figure 6.7 Cumulative failure distribution of 240 nm thick Cu lines at various test temperatures. The inset is the linear regression of [ln(MTTF) + n*ln(J)] vs. 1/kT, using n =2.7.

6.4 Failure analysis

It is well established that the basic requirement for EM to occur in an interconnect structure is the existence of flux divergence of metal atoms due to the electronic driving force. The atomic flux Γ related to the total driving force F can be expressed as the following equation.[128]

$$\Gamma = \frac{ND}{kT} F \tag{6.9}$$

where N is the atomic concentration and D is the diffusion coefficient. The atomic flux at the i-th grain boundary can be expressed as follow.

$$\Gamma_i = \frac{N_i D_i}{kT_i} Z^* qE \cos\phi_i \tag{6.10}$$

using $F_i = Z^* qE \cos\phi_i$, where $Z^* q$ is the effective charge of the ions, ϕ_i is the inclination angle of the i-th grain boundary with respect to the electron flow. The flux divergence at a triple junction point is $\sum \Gamma_i$, which is zero only when the relative angle between two adjacent grain boundaries is 120°.[128] However, due to the variation of the grain size, this particular condition is hardly met. A non-zero divergence at the triple junction point leads to an accumulation or void. As illustrated in Figure 6.8(a), if $\Gamma_1 < \Gamma_2 + \Gamma_3$, the void is formed by the divergent flux along the grain boundaries. In this case, the void at the early stage should have a triangle shape. Fig. 6.8(b) and (c) show the typical voids formed on the Cu line after the EM test at 350°C for 150 and 350 seconds and the removal of SiN_x cap layer, respectively. The voids were not due to the removal of the passivation layer, because no similar voids on the adjacent dummy lines were

observed. Although Fig. 6.8(b) and (c) were from different lines, the voids presented at the similar location, i.e., the triple junction point of grain boundaries. Therefore, the void initiated from the grain boundary junction point, grew larger as the EM continued, and grew preferentially along the grain boundaries, as shown as the sharp corners of the void in Fig. 6.8 (c).

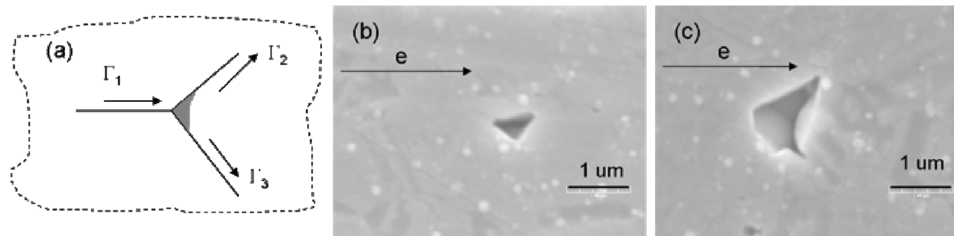

Figure 6.8 Illustration (a) and SEM images of void formation after EM at 350ºC for (b) 150 seconds, (c) 350 seconds.

Mass transport occurs not only along the grain boundary, but also along the interface. Cu atoms that are migrating along the upper Cu surface or Cu/dielectric interface are fed by two mechanisms: the Cu diffusion from inside of the metal line to the top surface along the grain boundaries, and the grain thinning, as illustrated in Figure 6.9(a). When the Cu atoms are depleted from the grain boundary or the inner free surface of the void that intersects the top Cu surface, the void tends to grow in a “v” shape. In this case, the void grows wider and deeper with the increase of time. For grain thinning, the surface atoms on the upstream grain diffuse to the void boundary, and then move up the step to feed the atoms that flow at the Cu/dielectric interface.[49] Therefore, the void leads to the flat upstream surface. Fig. 6.9(b) shows the top view of the Cu line after the EM test at 350°C for 2400 seconds and the removal of the top SiN_x. The recess areas in Fig. 6.9(b) corresponded to the voids at the Cu-SiN_x interface, which were due to the interfacial diffusion. Both grain boundary depletion voids and grain thinning voids are observed. Voids formed from grain thinning should have less impact on the Cu line resistance change than voids from grain boundary depletion because the lower-stream grains are still connected in the former situation. However, since both kinds of voids exist at the same time, it is hard to differentiate them from the resistance-time plot.

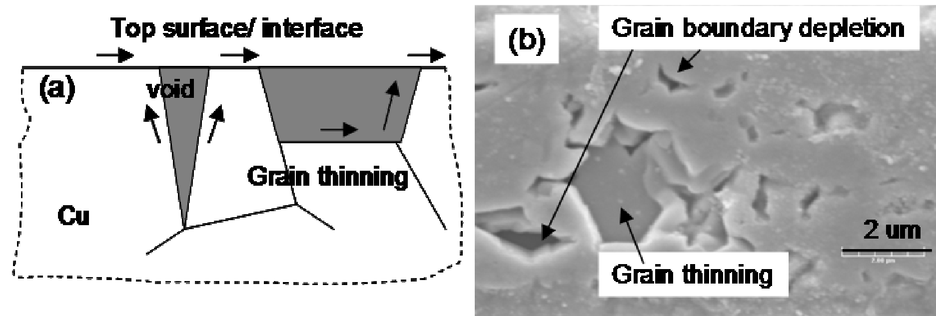

Figure 6.9 Illustration (a) and SEM image (b) of voids by grain thinning and grain boundary depletion after EM at 350ºC.

Figure 6.10 shows the failure site of a 200 nm thick Cu line after the EM test. The slit-like disconnection of the line was usually observed on the Al line with the bamboo structure where the grain boundary diffusion dominates the failure mode.[129] However, this mechanism can not be completely applied to this study because the Cu line width was much larger than the grain size, e.g., 7 um vs. less than 100 nm.[130] There was no bamboo structure in the Cu line used in this study. The EM induced voids started from the grain boundary triple junction point and grew larger by grain boundary depletion and void nucleation. These voids significantly reduced the line width. The increased current density in the remaining cross section area led to more local Joule heating, which in turn accelerated the void growth by increased ion flux or by temperature gradient-induced vacancy accumulation. Therefore, the voids extended into the remaining cross-section area, and resulted in the slit–like broken site.

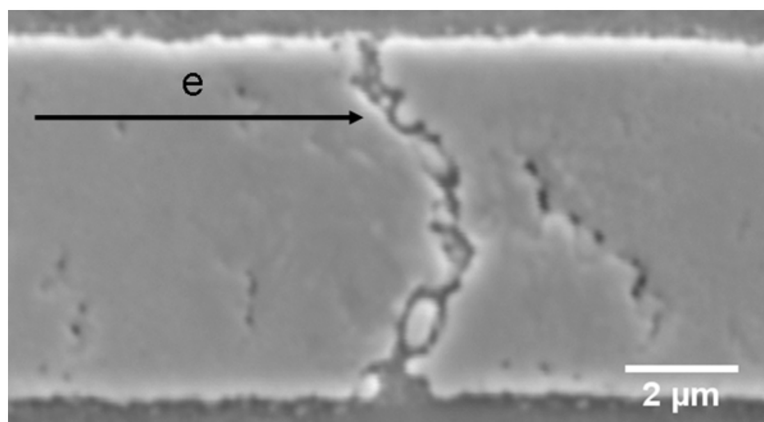

Figure 6.10 Slit-like failure site of thin Cu line after EM at 170ºC.

Figure 6.11(a) shows the top view of the Cu line failure after the 320°C EM test without the removal of the SiN_x cap layer. The cap layer crack is observable. As shown in Fig. 6.11(b), the EDX analysis confirmed that the Cu extruded from the cracked area. The Au and Pt peaks were from the coating layer. The crack was associated to the stress development during the EM test. The stress may come from three origins: intrinsic stress, thermal stress, and EM induced stress. The intrinsic stress caused by the PECVD SiN_x was altered by the N/Si ratio. For the N/Si ratio of 0.85 in this film,[102] there was no apparent compressive or tensile stress.[131] No crack was observed before the EM test, which indicates that the intrinsic stress was not a critical factor. The thermal stress (σ_T) can be calculated by the equation.[132]

$$\sigma_T = (T_0 - T) * \Delta\alpha * E \qquad (6.11)$$

where T_0 is the stress free temperature, T is the EM test temperature, $\Delta\alpha$ is the difference between the CTEs of Cu and SiN_x, E is the Young's modulus of Cu. The CTE values of Cu and SiN_x are $16.5x10^{-6}$ ºC^{-1} and $2.7x10^{-6}$ ºC^{-1}, respectively, and the E value of Cu is 125 GPa,.[133] According to equation (6.11), the thermal stress is less than 40 MPa at 320°C, indicating the thermal stress is unlikely the main contribution to the crack. The EM induced stress can be 100 MPa[2] or even 1 GPa,[134] depending on the test line's structure. The stress distribution along the line is more complex if there is a flux divergence along the length.[135] The cap layer crack occurs when the stress induced by EM exceeds the threshold stress of the cap layer.[136] The crack of the cap layer leads to the loss of the mechanical constrain on the Cu lines which, in turn, leads to the Cu line extrusion and results in an EM failure.

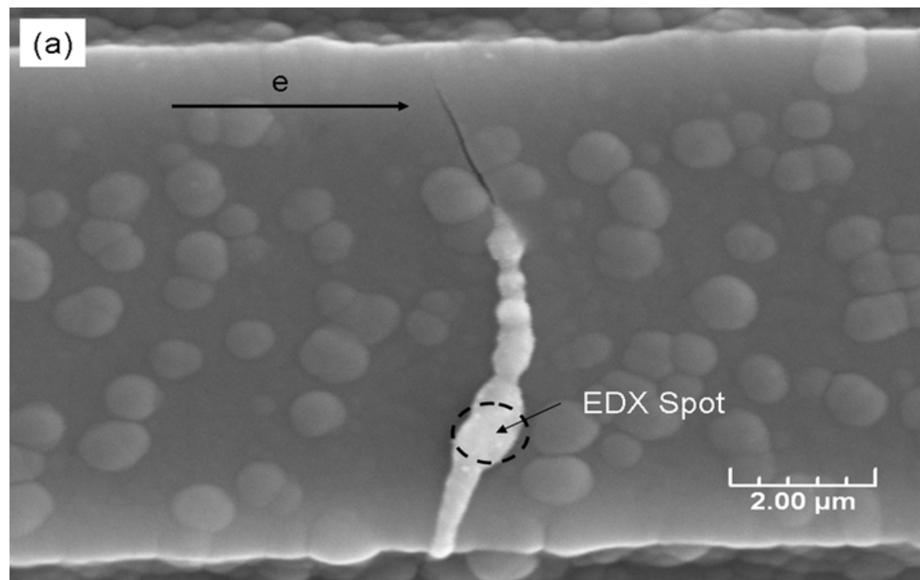

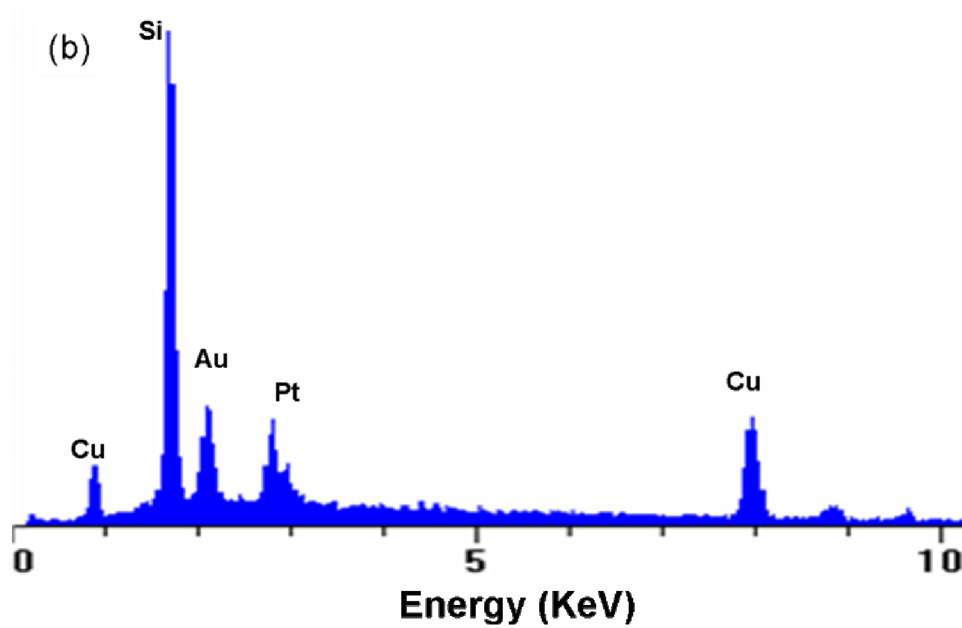

Figure 6.11 (a) Cap layer crack after EM at 320ºC and (b) EDX of the spot at (a).

The EM damage during a lifetime test is a dynamic and complex process, which may include more than one diffusion paths and more than one failure modes. If one diffusion mechanism is responsible for the void formation, other diffusion paths may interfere the damaging process. Again, the E_a value is more likely an apparent value. SEM observations show the interface between the Cu and the cap layer is critical to the EM failure, e.g., by the Cu grain thinning and the Cu extrusion. The grain boundary diffusion also plays an active role in the EM damage, e.g. the void growth at the triple junction point and the Cu depletion from the grain boundary.

6.5 External bending stress effect on Cu EM

To further investigate the mechanical stress effect on EM, EM tests were performed on the mechanically bended 800 nm thick Cu lines. Figure 6.12 shows the cumulative failure distribution of the bended Cu lines at the temperatures of 320°C, 350ºC and 380°C. The MTTFs of the bended lines are shorter than those of the non-bended lines at 320ºC and 350ºC, i.e., 8852s and 4944s vs. 11711s and 6000s, respectively. At 380ºC, these MTTFs of the bended and non-bended lines are comparable, i.e., 3320s vs. 3278s. According to equation (6.11), the thermal stress increases with the EM temperature, therefore the mechanical bending stress effect becomes less significant at 380ºC due to the increased thermal stress. The inserted plot shows the linear fit of [ln(MTTF)+nln(J)] vs. 1/kT using n = 2.7, leading to the E_a value of 0.5 eV, which is smaller than the E_a without bending stress, i.e., 0.6 eV. Similar activation energy shift was reported on the Cu damascene lines with an applied compressive stress.[137] Consideration the life time at

the regular use condition, according to equation (1.3), the MTTF at operation condition such as 105 ºC and 3 MA/cm^2 is only about 8 years, which is much shorter than that of non-bended Cu lines. As previously discussed, the cap layer crack was caused by the EM induced compressive stress. Assuming the threshold stress for the crack to occur is the same, the time to reach this threshold stress would obviously be dependent on the amount of original stress in the line. Therefore, for the Cu lines with an applied bending stress, EM would generate correspondingly less stress to induce the cap layer crack. Once the cap layer cracked, Cu was kept being pumped to the crack, leading to a shorter lifetime.

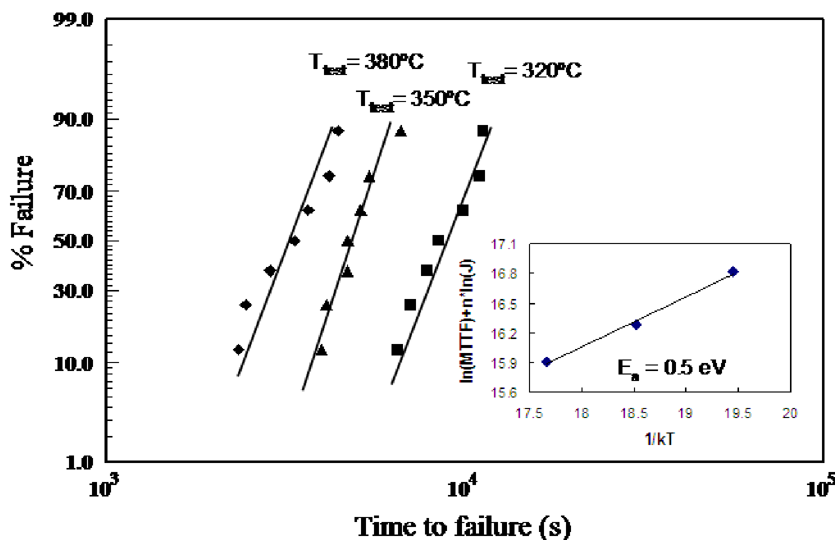

Figure 6.12 Cumulative failure distribution of thick Cu lines at various temperatures with applied bending stress. The inserted is the linear regression of [ln(MTTF) + n*ln(J)] vs. 1/kT, using n = 2.7.

In the EM test, the resistance change is a complex collective behavior of the void nucleation and growth. After EM tests, numerous voids were observed along the length. There was a noticeable difference in the voids distribution between the bended and non-bended lines. For example, in the non-bended line, the consecutive voids tended to line up along the current flow, as shown in Figure 6.13 (a). However, in the bended lines, the consecutive voids tended to line up perpendicular to the current flow, as shown in Fig. 6.13 (b). In a simplified mode, assuming the total volume of the voids are comparable for the bended and non-bended lines, the resistance change in a conductor of overall length L and width W is given by the following equation:

$$\frac{\Delta R}{R_0} = \frac{l(t)}{L} \times \left(\frac{W}{W - w(t)} - 1\right) \quad (6.12)$$

where $l(t)$ and $w(t)$ are equivalent overall void length and width at time t, respectively. From equation (6.12), the voids aligned perpendicular to the current flow play a larger impact on the resistance change than the voids aligned parallel to the current flow do. Therefore, the line with the void distribution in Fig. 6.13(b) would have a short lifetime. Although equation (6.12) was developed based on a simplified model, more detail study and simulation on the void morphology showed the similar result.[138] Therefore, the bending stress affected the void distribution and shortened the EM lifetime. This result is critical to the application of Cu lines in the large area flexible electronics.

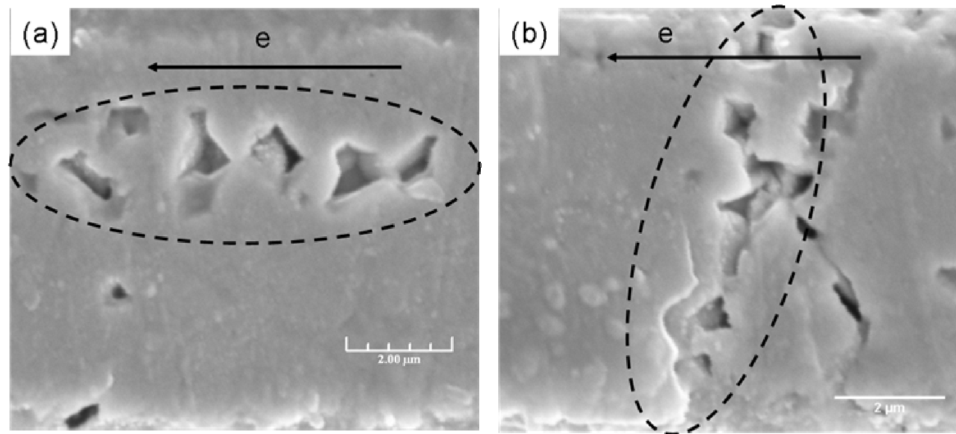

Figure 6.13 Typical void distribution in (a) non-bended line, (b) bended line after EM at 350ºC.

6.6 Summary

The isothermal electromigration tests were performed on the single level Cu interconnect lines prepared from a Cl_2 plasma-based etch process. An activation energy of 0.5~0.6 eV and a current density exponent of 2.7 were obtained. Failure analysis provided by SEM pictures showed that the voids were initiated from the grain boundary junction points and grew preferentially along the grain boundaries. Both the Cu-SiN_x interface and the Cu grain boundary diffusion were critical to the EM failure. The EM induced compressive stress caused the cap layer crack which in turn led to Cu extrusion. The Cu lines with the bended compressive stress showed a shorter lifetime and a lower activation energy than the non-bended lines. The bending stress not only accelerated the cap layer crack, but also affected the void distribution, which shortened the lifetime of the Cu lines. Results in this study will be important to the large area flexible electronics.

CHAPTER VII

SUMMARY AND CONCLUSIONS

Copper films can be patterned with a unique plasma-based etching process. Instead of forming volatile reaction products during the plasma exposure, the Cu film is converted into $CuCl_x$ which is dissolved into a dilute HCl solution. Many factors were proved to have an impact on this plasma-based Cu etching process, such as feed gas, plasma pressure, RF power, and substrate temperature. It was further proved that the microstructure of Cu film also played substantial influence on the Cu etch process. Under the same Cl_2 plasma condition, the Cu conversion rate and the $CuCl_x$ reaction product formation rate increased monotonically with the grain size of the starting Cu film. Cu and Cl diffused through the bulk Cu grain at much slower rates than along the grain boundary. The reaction rate of the former was also much slower than that of the latter. The $CuCl_x$ layer's porosity and Cl content were critical to Cu conversation process because they both influence the Cl supply mechanism. The grain size and boundary effects were further confirmed through examining the surface structure of the chlorinated Cu film. This study delineated critical Cu microstructure effects on the plasma-based Cu etch process, which is potentially important for the fabrication of many microelectronic and optoelectronic products.

It is very important to obtain the notch-free Cu lines with the plasma-based etching process. Several approaches have been applied to reduce the Cu lines sidewall attack of a predefined Cu patten by introducing additive gases into the Cl_2 feed stream. The additive

gas strongly affects the Cu conversion rate and the sidewall roughness in the Cl_2 plasma process. This is because the plasma phase chemistry, ion bombardment energy, and the surface structure all change with the additive gas. The addition of Ar enhanced the Cu conversion rate due to the strong ion bombardment and the increase of the Cl concentration; the latter also increased the sidewall roughness. The addition of N_2 increased the Cu conversion rate due to the increase of ion bombardment energy. However, due to the dilution of the Cl concentration, Cu sidewall did not show "mouse bites". The addition of CF_4 can either increase or decrease the Cl concentration in the plasma phase depending on the CF_4 concentration. The ion bombardment energy increased monotonically with the CF_4 concentration. The Cl_2/CF_4 plasma exposed Cu sidewall was smooth and free of "mouse bites" due to the formation of a protection layer of CF_x, CuF_x, or both. In summary, the vertical direction Cu consumption process is related to the ion bombardment energy and the Cl concentration. The sidewall attack can be reduced or eliminated with the formation of a protective layer by adding N_2 or CF_4 into the Cl_2 plasma.

Cu can easily diffuse into the silicon substrate or dielectric layer, therefore a TiW layer was used as the diffusion barrier layer. Plasma etching process of the TiW film has been investigated using the CF_4/O_2, CF_4/Cl_2, and CF_4/HCl feed gases under various gas compositions, RF powers, and plasma pressures. The etch rate behaviors are different in various plasmas. In the CF_4/O_2 plasmas, the F is the dominant etchant and the etch rate changes consistently with the F concentration. However, in the CF_4/Cl_2 and CF_4/HCl plasmas, the etch rate changes with the sum of Cl and F concentrations. The increase of

RF power increases ion bombardment energy, which enhances the etch rate. The maximum TiW etch rate was achieved with the proper combination of plasma phase chemistry and ion bombardment energy at the medium pressure condition. The CF_4 plasma exposed TiW surface contains two types of F: physically adsorbed F, and chemically bonded F such as tungsten oxyfluoride or titanium fluoride. The Cl_2 plasma exposed TiW surface contains a trace amount of physically adsorbed Cl, however, metal-Cl bonds were not observed due to the instantaneous removal of the chloride during the etching process. The etch selectivity of TiW to SiN_x decreases with the increase of the CF_4 concentration and with the increase of the RF power. A etch ratio of TiW/SiN_x greater than 2 was readily obtained.

Cu/barrier metal stack was successfully patterned with above plasma etching processes. The isothermal electromigration tests were performed on the single level Cu lines that were prepared by the Cl_2 plasma-based etch process. The activation energy of 0.5~0.6 eV and the current density exponent of 2.7 were obtained. Failure analysis provided by SEM pictures showed various diffusion paths including the Cu-SiN_x interface and the Cu grain boundary. The EM induced compressive stress caused the SiN_x cap layer crack which, in turn led to Cu extrusion. The Cu line with the bended compressive stress showed a shorter lifetime and lower activation energy. The bending stress not only accelerated the cap crack, but also affected the void distribution, which shortened the lifetime of the Cu lines.

This dissertation provides profound understandings of the etching processes of Cu and TiW films. The factors affecting the etching process are carefully investigated. The

reliability of the Cu lines patterned by above plasma etching processes was assessed. Those processes can be applied to the fabrication of many advanced microelectronic devices including large area flexible micrielectronics.

REFERENCES

1. J.-Y. Tewg, Y. Kuo and J. Lu, *J. Electrochem. Soc.*, **152**, G643 (2005).

2. C. S. Hau-Riege, *Microelectron. Reliab.*, **44**, 195 (2004).

3. S. P. Murarka and S. W. Hymes, *Crit. Rev. Solid State Mater. Sci.*, **20**, 87 (1995).

4. S.-P. Jeng, R. H. Havermann and M.-C. Chang, *Mater. Res. Soc. Symp. Proc.*, **337**, 25 (1994).

5. S. P. Murarka, *Metallization-Theory and Practice for VLSI and ULSI*, Butterworth-Heinermann, Boston (1993).

6. J. D. McBrayer, R. M. Swanson and T. W. Sigmon, *J. Electrochem. Soc.*, **133**, 1243 (1986).

7. J. D. Plummer, M. D. Deal and P. B. Griffin, *Silicon VLSI Technology: Fundamentals, Practice and Modeling*, Pentice Hall, New Jersey (2000).

8. J. W. Coburn and M. Chen, *J. Appl. Phys.*, **51**, 3134 (1980).

9. S. Kondo, N. Sakuma, Y. Homma, Y. Goto, N. Ohashi, H. Yamaguchi and N. Owada, *J. Electrochem. Soc.*, **147**, 3907 (2000).

10. B. M. Belongia, P. D. Haworth, J. C. Baygents and S. Raghavan, *J. Electrochem. Soc.*, **146**, 4124-4130 (1999).

11. Y. Kuo and S. Lee, *Vacuum*, **74**, 473 (2004).

12. M. S. Kwon, J. Y. Lee, K.-S. Choi and C.-H. Han, *Jpn. J. Appl. Phys. Part 1*, **37**, 4103 (1998).

13. S.-K. Lee, S.-S. Chun, C. Hwang and W.-J. Lee, *Jpn. J. Appl. Phys. Part 1*, **36**, 50 (1997).

14. A. M. Efremov and V. I. Svettsov, *Russ. Microelectron.*, **31**, 179 (2002).

15. K. Ohno and M. Sato, *Pro. Electrochem. Soc.*, **93**, 316 (1993).

16. Y. Kuo and S. Lee, *Appl. Phys. Lett.*, **78**, 1002 (2001).

17. S. Lee and Y. Kuo, *J. Electrochem. Soc.*, **148**, G524 (2001).

18. Y. Kuo, H. Nominanda and G. Liu, *J. Korean Phys. Soc.*, **48**, S92 (2006).

19. S. Lee and Y. Kuo, *Jpn. J. Appl. Phys.*, **41**, 7345 (2002).

20. Y. Kuo, *J. Electrochem. Soc.*, **137**, 1907 (1990).

21. P. M. Schaible, W. C. Metzger and J. P. Anderson, *J. Vac. Sci. Technol.*, **15**, 334 (1978).

22. E. Schonbachler, B. Lecohier and W. Fichtner, *J. Vac. Sci. Technol., B*, **15**, 2011 (1997).

23. W. Sesselmann and T. J. Chuang, *Surf. Sci.*, **176**, 32 (1986).

24. H. F. Winters, *J. Vac. Sci. Technol. A*, **3**, 786 (1985).

25. N. Cabrera, *Rep. Prog. Phys.*, **12**, 163 (1949).

26. Y.-R. Zhang and E. S. Machlin, *Mater. Lett.*, **8**, 182 (1989).

27. C. Y. Nakakura and E. I. Altman, *J. Vac. Sci. Technol. A*, **15**, 2359 (1997).

28. S. Lee and Y. Kuo, *Jpn. J. Appl. Phys.*, **41**, 7345 (2002).

29. S. Tabara, *J. Vac. Sci. Technol. B*, **16**, 553 (1998).

30. M. Markert, A. Bertz, T. Gessner, Y. Ye, A. Zhao and D. Ma, *Microelectron. Eng.*, **50**, 417 (2000).

31. T. Kinoshita, *J. Vac. Sci. Technol. B*, **14**, 560 (1996).

32. J. P. Chang and H. H. Sawin, *J. Vac. Sci. Technol. B*, **19**, 1870 (2001).

33. H. Uetake, T. Matsuura, T. Ohmi, J. Murota, K. Fukuda and N. Mikoshiba, *Appl. Phys. Lett.*, **57**, 596 (1990).

34. E. R. Webber, *Appl. Phys. A: Solids Surf.*, **30**, 1 (1983).

35. S.-Q. Wang, *J. Appl. Phys.*, **73**, 2301 (1993).

36. H.-W. Wang and B.-S. Chiou, *J. Mat. Sci.*, **11**, 17 (2000).

37. I.-S. Jin, H.-H. Park, K.-H. Kwon and C.-I. Kin, *Microelectron. Eng.*, **33**, 223 (1997).

38. R. d'Agostino, F. Fracassi and C. Pacifico, *J. Appl. Phys.*, **72**, 4351 (1992).

39. G. Turban, J. F. Coulon and N. Mutsukura, *Thin Solid Films*, **176**, 289 (1989).

40. M. Milosavljevic and N. Bibic, *Thin Solid Films*, **164**, 493 (1988).

41. O. Krause and H. Ryssel, *J. Appl. Phys.*, **91**, 5645 (2002).

42. A. A. Istratov, C. Flink, H. Hieslmair and E. R. Weber, *Phys. Rev. Lett.*, **81**, 1243 (1998).

43. R. d'Agostino, F. Fracassi, C. Pacifico and P. Capezzuto, *J. Appl. Phys.*, **71**, 462 (1992).

44. D. S. Fischl and D. W. Hess, *J. Electrochem. Soc.*, **134**, 2265 (1987).

45. K. Ninomiya, K. Suzuki, S. Mishimatsu and O. Ukada, *J. Appl. Phys.*, **62**, 1549 (1987).

46. J. H. Thomas-III and L. H. Hammer, *J. Vac. Sci. Technol. B*, **5**, 1617 (1987).

47. P. E. Riley, *IEEE Trans.Semiconductor Manuf.,* **8**, 309 (1995).

48. Y. Kuo, *J. Electrochem. Soc.*, **137**, 1235 (1990).

49. C.-K. Hu, L. Gignac and R. Rosenberg, *Microelectron. Reliab.*, **46**, 213 (2006).

50. R. E. Jones, Jr. and L. D. Smith, *J. Appl. Phys.*, **61**, 4670 (1987).

51. T. Berger, L. Arnaud, R. Gonella, G. Lormand and Y. Morand, *Microelectron. Reliab.*, **40**, 1311 (2000).

52. J. R. Black, *Reliab. Phys. Symp.*, **6**, 148 (1967).

53. J. R. Lloyd and J. J. Clement, *Thin Solid Films*, **262**, 135 (1995).

54. J. R. Lloyd, J. Clemens and R. Snede, *Microelectron. Reliab.*, **39**, 1595 (1999).

55. J. Proost, T. Hirato, T. Furuhara, K. Maex and J. P. Celis, *J. Appl. Phys.*, **87**, 2792 (2000).

56. A. V. Vairagar, S. G. Mhaisalkar and A. Krishnamoorthy, *Microelectron. Reliab.*, **44**, 747 (2004).

57. A. Leong, *IEEE IRW Final Report*, **2001**, 63 (2001).

58. L. Arnaud, T. Berger and G. Reimbold, *J. Appl. Phys.*, **93**, 192 (2003).

59. R. G. Filippi, M. A. Gribelyuk, T. Joseph and etc, *Thin Solid Films*, **388**, 303 (2001).

60. Y. Kuo, *J. Electrochem. Soc.*, **142**, 186 (1995).

61. M. Sugawara, *Plasma Etching-Fundmentals and Applications*, Oxford University Press, Oxford (1998).

62. R. A. Gottscho and V. M. Donnelly, *J. Appl. Phys.*, **56**, 245 (1984).

63. V. M. Donnelly, D. L. Flamm and R. H. Bruce, *J. Appl. Phys.*, **58**, 2135 (1985).

64. O. Auciello and D. L. Flamm, *Plasma Diagnostics*, Academic Press Inc., San Diego CA (1989).

65. V. M. Donnelly, D. L. Flamm, W. C. Dautremont-Smith and D. J. Werder, *J. Appl. Phys.*, **55**, 242 (1984).

66. D. P. Woodruff and T. A. Delchar, *Modern Techniques of Surface Science* Cambridge University Press, Cambridge (1994).

67. C. Hammond, *The Basics of Crystallography and Diffraction*, Oxford University Press, New York (2001).

68. S.-K. Rha, W.-J. Lee, S.-Y. Lee, D.-W. Kim, C.-O. Park and S.-S. Chun, *Jpn. J. Appl. Phys., Part 1*, **35**, 5781 (1996).

69. V. G. Glebovsky, V. Y. Yaschak, V. V. Baranov and E. L. Sackovich, *Thin Solid Films*, **257**, 1 (1995).

70. A. F. Mayadas and M. Shatzkes, *Phys. Rev. B*, **1**, 1382 (1970).

71. J. M. E. Harper and C. Cabral Jr, *J. Appl. Phys.*, **86**, 2516 (1999).

72. S. H. Kang, Y. S. Obeng, M. A. Decker, M. Oh, S. M. Merchant, S. K. Karthikeyan, C. S. Seet and A. S. Oates, *J. Electron. Mater.*, **30**, 1506 (2001).

73. W. W. Mullins, *J. Appl. Phys.*, **28**, 333 (1957).

74. S. Nakahara, S. Ahmed, T. T. Ahmed and D. N. Buckley, *J. Electrochem. Soc.*, **154**, D145 (2007).

75. D. R. Lide, *CRC handbook of Chemistry and Physics*, CRC Press, New York (1999).

76. D. Westphal and A. Goldmann, *Surf. Sci.*, **131**, 92 (1983).

77. G. Liu and Y. Kuo, *J. Electrochem. Soc.*, **155**, H97 (2008).

78. F. Delamare and G. E. Rhead, *Surf. Sci.*, **28**, 267 (1971).

79. W. Sesselmann and T. J. Chuang, *Surf. Sci.*, **176**, 67 (1986).

80. M. K. Balapanov, E. K. Urazaeva, I. B. Zinnurov, R. S. Musalimov and R. A. Yakshibaev, *Ionics*, **12**, 205 (2006).

81. H. Raaf and N. Schwentner, *Appl. Surf. Sci.*, **174**, 13 (2001).

82. H. Aoki, E. Ikawa, T. Kikkawa, Y. Teraoka and I. Nishiyama, *Jpn. J. Appl. Phys.*, **31**, 2041 (1992).

83. J. R. Fuhr and W. L. Wiese, *CRC handbook of Chemistry and Physics*, CRC Press, Boston (1995).

84. K. Kobayashi, Y. Inoue, T. Nishimura, M. Hirayama, Y. Akasaka, T. Kato and S. Ibuki, *J. Electrochem. Soc.*, **137**, 1987 (1990).

85. S. Lee, *A Study of Plasma-Based Copper Etching Reaction Process*, Dissertation, Texas A&M University, College Station (2001).

86. C. B. Zarowin, *J. Electrochem. Soc.*, **130**, 1144 (1983).

87. K.-H. Kwon, C.-I. Kim, S. J. Yun and G.-Y. Yeom, *J. Vac. Sci. Technol. A*, **16**, 2772 (1998).

88. T. Bruckl and H. Zull, *J. Appl. Phys.*, **98**, 023307/023301 (2005).

89. J. K. Sheu, Y. K. Su, G. C. Chi and M. J. Jou, *J. Appl. Phys.*, **85**, 1970 (1999).

90. J. M. Knight, J. L. C. Fonseca, Z. V. Hauptman and J. P. S. Badyal, *Chem. Mater.*, **5**, 1221 (1993).

91. G. Soto, J. A. Diaz and W. d. l. Cruz, *Mater. Lett.*, **57**, 4130 (2003).

92. A. Nilson, O. Bjorneholm, H. Tillborg, B. Hernnas, R. J. Guest, A. Sandell, R. E. Palmer and N. Martensson, *Surf. Sci.*, **287-288**, 758 (1993).

93. Y. Kuo, *Jpn. J. Appl. Phys.*, **29**, 2243 (1990).

94. A. L. Ji, R. Huang, Y. Du, C. R. Li, Y. Q. Wang and Z. X. Cao, *J. Cryst. Growth*, **295**, 79 (2006).

95. J.-K. Jung and W.-J. Lee, *Jpn. J. Appl. Phys. Part 1*, **40**, 1408 (2001).

96. Y. Kuo, *J. Vac. Sci. Technol. A*, **8**, 1702 (1990).

97. A. Mimoto, T. Miyazaki, J. Yamashita, S. Nagamine, M. Inaba and A. Tasaka, *J. Electrochem. Soc.*, **153**, D149 (2006).

98. M. S. Silverstein, L. Sandrin, and E. Sacher, *Polymer*, **42**, 4299 (2001).

99. J.-H. Min, S.-W. Hwang, G.-R. Lee and S. H. Moon, *J. Vac. Sci. Technol. A*, **20**, 1574 (2002).

100. R. P. Vasquez, M. C. Foote and B. D. Hunt, *J. Appl. Phys.*, **66**, 4866 (1989).

101. C. Gabriel and J. Zheng, *J. Vac. Sci. Technol. A*, **15**, 697 (1997).

102. Y. Kuo and H. L. Lee, *Vacuum*, **66**, 299 (2002).

103. Y. Waseda, K. Hirata and M. Ohtani, *High Temp. High Pressures*, **7**, 221 (1975).

104. V. G. Glebovsky, V. Y. Yaschak, V. V. Baranov and E. L. Sackovich, *Thin Solid Films*, **257**, 1 (1994).

105. C. J. Mogab, A. C. Adams and D. L. Flamm, *J. Appl. Phys.*, **49**, 3796 (1978).

106. F. Fracassi and J. W. Coburn, *J. Appl. Phys.*, **63**, 1758 (1988).

107. D. M. Manos and D. L. Flamm, *Plasma Etching: An Introduction*, Academic Press, San Diego (1988).

108. J. W. Coburn, *J. Appl. Phys.*, **50**, 5210 (1979).

109. K. Ikeda and Y. Oshita, *J. Vac. Sci. Technol. B*, **16**, 159 (1998).

110. C. J. Choi, Y. S. Seol and K.-H. Baik, *Jpn. J. Appl. Phys. Part 1*, **37**, 801 (1998).

111. G. S. Oehrlein and J. L. Lindstom, *J. Vac. Sci. Technol., A*, **7**, 1035 (1989).

112. F. Fracassi, R. d'Agostino, R. Lamendola and I. Mangieri, *J. Vac. Sci. Technol. A*, **13**, 335 (1995).

113. A. Bensaoula, E. Grossman and A. Ignatiev, *J. Appl. Phys.*, **62**, 4587 (1987).

114. G. Liu and Y. Kuo, *J. Electrochem. Soc.*, **154**, H653 (2007).

115. L. D. Chen, M. J. Zhang and S. Zhang, *J. Appl. Phys.*, **76**, 1547 (1994).

116. EIA/JESD61, *Isothermal Electromigration Test Procedure* (1997).

117. EIA/JESD33-B, *Standard Method of Measuring and Using the Temperature Coefficient of Resistance to Determine the Themperature of a Metallization Line* (2004).

118. J. V. Hagen and H. A. Schafft, *IEEE IRW Final Report*, 45 (2002).

119. T. Sullivan, T. Lee and D. Tibel, *IEEE IRW Final Report*, 80 (2000).

120. S. Yokogawa, N. Okada, Y. Kakuhara and H. Takizawa, *Microelectron. Reliab.*, **41**, 1409 (2001).

121. C.-K. Hu, *Thin Solid Films*, **260**, 124 (1995).

122. C.-K. Hu and J. M. E. Harper, *Mater. Chem. Phys.*, **52**, 5 (1998).

123. N. L. Michael, C.-U. Kim, P. Gillespie and R. Augur, *J. Electron. Mater.*, **32**, 988 (2003).

124. B. Li, T. D. Sullivan, T. C. Lee and D. Badami, *Microelectron. Reliab.*, **44**, 365 (2004).

125. M. H. Lin, Y. L. Lin, K. P. Chang, K. C. Su and T. Wang, *Microelectron. Reliab.*, **45**, 1061-1078 (2005).

126. T. C. Lee, M. Ruprecht, D. Tibel, T. D. Sullivan and S. Wen, *IEEE Int. Reliab. Phys. Symp.*, **40**, 327 (2002).

127. C. S. Hau-Riege and C. V. Thompson, *Appl. Phy. Lett.*, **78**, 3451 (2001).

128. G. L. Baldini, I. D. Munari, A. Scorzoni and F. Fantini, *Microelectron. Reliab.*, **33**, 1779 (1993).

129. J. E. Sanchez, Jr., L. T. McKnelly and J. W. Morris, Jr., *J. Appl. Phys.*, **72**, 3201 (1992).

130. G. Liu, Y. Kuo, S. Ahmed, D. N. Buckley and T. Tanaka-Ahmed, *J. Electrochem. Soc.*, **155**, H432 (2008).

131. K. Hiranaka, T. Yoshimura and T. Yamaguchi, *J. Appl. Phys.*, **62**, 2129 (1987).

132. Y.-J. Park, K.-D. Lee and W. R. Hunter, *IEEE Int. Reliab. Phys. Symp.*, 18 (2005).

133. T. Kramer and O. Paul, *Sens. Actuators, A*, **92**, 292 (2001).

134. S. Chiras and D. R. Clarke, *J. Appl. Phys.*, **88**, 6302 (2000).

135. C. S. Hau-Riege, S. P. Hau-Riege and A. P. Marathe, *J. Appl. Phys.*, **96**, 5792 (2004).

136. Z. Suo, *Acta. Mater.*, **46**, 3725 (1998).

137. G. Reimbold, O. Sicardy, L. Arnaud, F. Fillot and J. Torres, *IEDM Tech. Digest,* 745 (2002).

138. J. E. Sanchez, Jr., L. T. McKnelly and J. W. Morris, Jr., *J. Electron. Mater.*, **19**, 1213 (1990).

APPENDIX A

RCA WAFER CLEANING

Its name is derived from the original wafer cleaning process developed at RCA Laboratories in 1970. This clean consists of a sequence of cleaning steps using "standard" solutions which has become known as the "RCA clean".

Step #1: Standard Cleaning solution #1 (SC-1) consists of a mixture of ammonium hydroxide (NH_4OH), hydrogen peroxide (H_2O_2), and DI water (H_2O). A typical concentration ratio for the mix is 1:1:5 $NH_4OH:H_2O_2:H_2O$. The solution is to remove particles from the surface of the wafer. The solution is also very effective at removing organic contaminants and some metallic contaminants from the surface of the wafer. It accomplishes this by continually oxidizing and then etching the surface of the wafer, thereby dissolving the contaminants into solution. It is typically operated at the temperature 70 °C.

Step #2: Standard Cleaning solution #2 consists of a mixture of hydrochloric acid (HCl), hydrogen peroxide (H_2O_2), and DI water (H_2O). A typical concentration ratio for the mix is 1:1:5 $HCl:H_2O_2:H_2O$. The solution is to remove metal contaminants from the wafer surface, and it usually follows the SC-1 in the RCA sequence. Like the SC-1, it removes metals by continually oxidizing and then etching the surface of the wafer, thereby dissolving the contaminants into solution. It is typically operated at the temperature 70 °C.

Finally the silicon wafer is dried with N_2 gun.

APPENDIX B

COPYRIGHT PERMISSION

05/16/2008 FRI 13:56 FAX 001/001

Page 1 of 1

Patricia Lorynski

From: Guojun Liu [guojun@tamu.edu]
Sent: Monday, May 12, 2008 11:44 AM
To: Copyright
Subject: Permissions Request

Permissions Request
The Electrochemical Society (ECS)
65 South Main Street
Pennington, NJ 08534, USA

To whom to be concerned,

I am a doctoral candidate at Texas A&M University, and am writing to request permission to include the following informaiton into my dissertation:

1. Guojun Liu,Yue Kuo,Shafaat Ahmed, Denis N. Buckley, and Tanjim Tanaka-Ahmed, "Grain-size effect on a plasma-based copper etch process", *Journal of The Electrochemical Society*, 155(6) H432-H437 (2008).

The dissertation will be made available to the public on the Web through Texas A&M University Libraries. In addition the dissertation will be microfilmed by UMI Dissertation Publishing (ProQuest Information and Learning), and copies of the dissertation will be sold on demand.

Please supply a signed letter granting me permission to use the works.

Thanks for your favorable help.

Sincerely

Guojun

Guojun Liu
Ph.D. Candidate
Department of Chemical Engineering
Texas A&M University
Tel: (979) 862-1179
FAx: (979) 845-6446
Email: guojun@tamu.edu

Permission is granted to include the above-referenced paper in your thesis, provided that you obtain permission of the other individual authors. In the thesis, please acknowledge the authors and the citation given above, and include the words: "Reproduced by permission of ECS — The Electrochemical Society."

May 16, 2008 — Date

Ann F. Goedkoop, Director of Publications

5/12/2008

Patricia Lorynski

From: Guojun Liu [guojun@tamu.edu]
Sent: Friday, March 14, 2008 11:49 AM
To: Copyright
Cc: Guojun Liu
Subject: permission request for JECS paper

Permissions Request
The Electrochemical Society (ECS)
65 South Main Street
Pennington, NJ 08534, USA

To whom to be concerned,

I am a doctoral candidate at Texas A&M University, and am writing to request permission to include the following informaiton into my dissertation:

1. Guojun Liu and Yue Kuo, "Additive Gas Effects on Cl_2 Plasma-based Cu Etching Process and Sidewall Attack", *Journal of The Electrochemical Society*, 155(2) H97-102, (2008).
2. Guojun Liu and Yue Kuo, "Reactive Ion Etching of TiW Films", *Journal of The Electrochemical Society*, 154(7), H653-658, (2007)

The dissertation will be made available to the public on the Web through Texas A&M University Libraries. In addition the dissertation will be microfilmed by UMI Dissertation Publishing (ProQuest Information and Learning), and copies of the dissertation will be sold on demand.

Please supply a signed letter granting me permission to use the works.

Thanks for your favorable help.

Sincerely

Guojun

Permission is granted to include the above-referenced papers in your thesis, provided that you obtain permission of the other individual authors. In the thesis, please acknowledge the authors and the citation given above, and include the words: "Reproduced by permission of ECS — The Electrochemical Society."

March 18, 2008
Date

Ann F. Goedkoop, Director of Publications

VITA

Name: Guojun Liu

Current Address: Department of Chemical Engineering
Texas A&M University
College Station, TX 77843-3122

Email Address: guojun@gmail.com

Education: B.S., Chemical Engineering, Tsinghua University, Beijing, China, 1999.
Ph.D., Chemical Engineering, Texas A&M University, College Station, TX, 2008.

Selected Publications:

1. G. Liu, Y. Kuo, S. Ahmed, D. Buckley, and T. Ahmed, "Grain size effect on plasma-based Copper Etch process", *Journal of The Electrochemical Society*, 155(6) H432-H437 (2008).
2. G. Liu and Y. Kuo, "Additive Gas Effect on Plasma-based Copper Etch Process and Sidewall Attack", *Journal of The Electrochemical Society*, 155 (2), H97-H102, (2008).
3. G. Liu and Y. Kuo, "Reactive Ion Etching of Titanium Tungsten Thin Films", *Journal of The Electrochemical Society*, 154 (7), H653-H658, (2007).

This dissertation was typed by Guojun Liu